

# Optical and structural properties of ultrathin films on noble metals

---

Lončarić, Martin

Doctoral thesis / Disertacija

2011

*Degree Grantor / Ustanova koja je dodijelila akademski / stručni stupanj:* **University of Zagreb, Faculty of Science / Sveučilište u Zagrebu, Prirodoslovno-matematički fakultet**

*Permanent link / Trajna poveznica:* <https://um.nsk.hr/um:nbn:hr:217:268677>

*Rights / Prava:* [In copyright](#)/[Zaštićeno autorskim pravom.](#)

*Download date / Datum preuzimanja:* **2025-04-01**



*Repository / Repozitorij:*

[Repository of the Faculty of Science - University of Zagreb](#)





UNIVERSITY OF ZAGREB  
FACULTY OF SCIENCE  
DEPARTMENT OF PHYSICS

Martin Lončarić

**OPTICAL AND STRUCTURAL  
PROPERTIES OF ULTRATHIN FILMS  
OF NOBLE METALS**

DOCTORAL THESIS

Zagreb, 2011.



SVEUČILIŠTE U ZAGREBU  
PRIRODOSLOVNO MATEMATIČKI FAKULTET  
FIZIČKI ODSJEK

Martin Lončarić

**OPTIČKA I STRUKTURNA SVOJSTVA  
ULTRATANKIH SLOJEVA  
PLEMENITIH METALA**

DOKTORSKI RAD

Zagreb, 2011.



SVEUČILIŠTE U ZAGREBU  
PRIRODOSLOVNO MATEMATIČKI FAKULTET  
FIZIČKI ODSJEK

Martin Lončarić

**OPTIČKA I STRUKTURNA SVOJSTVA  
ULTRATANKIH SLOJEVA  
PLEMENITIH METALA**

DOKTORSKI RAD

Mentor:

Dr. sc. Hrvoje Zorc

Zagreb, 2011.



UNIVERSITY OF ZAGREB  
FACULTY OF SCIENCE  
DEPARTMENT OF PHYSICS

Martin Lončarić

**OPTICAL AND STRUCTURAL  
PROPERTIES OF ULTRATHIN FILMS  
OF NOBLE METALS**

DOCTORAL THESIS

Supervisor:  
Hrvoje Zorc, Ph. D.

Zagreb, 2011.

# Acknowledgements

I would like to express my gratitude to all those who made this thesis possible.

First of all, I would like to thank to my supervisor Dr. Hrvoje Zorc and to my colleagues Dr. Jordi Sancho-Parramon and Dr. Vesna Janicki for the support, guidance, valuable advices and discussions. They gave me decisive support and encouraged me to complete this thesis.

This thesis would not be possible without the collaboration with other research groups and experiments performed in their labs. I want to express my gratitude to Dr. Georg Jakopic and Dr. Anja Haase from Joanneum Research Institute for Surface Technologies and Photonics in Weiz, to Dr. Sigrid Bernstorff from SAXS line at Elettra synchrotron in Trieste and to Dr. Pavo Dubček and Dr. Suzana Šegota from “Ruđer Bošković” Institute. I want to thank Dr. Slobodan Tomaš and Professor Marijan Šunjić for discussing and clarifying theoretical aspects of the thesis with me.

In the name of all the readers of this thesis, I would like to thank Dunja Bebek for the effort she has put in proofreading this text.

Everything is easier when you work in a nice atmosphere among friends and colleagues of my LAIR department. I enjoy the time I spend with all of you. In living memory of our Mladen Pavlović is also always with us.

Finally, I would like to express my deepest appreciation to my Family, thank you for all your support and patience.

# Contents

## Extended abstract in Croatian language

<b>1. Introduction</b>	<b>1</b>
<b>2. Theoretical background</b>	<b>6</b>
<b>2.1. Noble metal nanoparticle growth</b>	<b>6</b>
<b>2.2. Interaction of light with matter</b>	<b>9</b>
2.2.1. Maxwell's equations in matter	9
2.2.2. Optical properties of materials	13
2.2.3. Optical properties of dielectric materials and semiconductors	16
2.2.4. Optical properties of metals	21
<b>2.3. Plasmonics</b>	<b>24</b>
2.3.1. Volume plasmons (bulk plasmons)	24
2.3.2. Surface plasmon polaritons (surface plasmons)	26
2.3.3. Localized surface plasmons (particle plasmons)	27
<b>2.4. Plasmons in noble metal island films</b>	<b>31</b>
2.4.1. Effective medium theories for plasmons in metal island films	32
2.4.2. Oscillator model for plasmons in noble metal island films	36
<b>2.5. Spectroscopic ellipsometry</b>	<b>38</b>
<b>2.6. Grazing-incidence small-angle X-ray scattering</b>	<b>44</b>
2.6.1. Approximate quantitative analysis – Guinier's approximation	47
2.6.2. GISAXS analysis beyond Guinier's approximation	48

<b>3. Experimental</b>	<b>49</b>
<b>3.1. Sample preparation</b>	<b>49</b>
<b>3.2. Materials</b>	<b>50</b>
<b>3.3. Optical characterisation techniques</b>	<b>51</b>
3.3.1. Spectrophotometry	52
3.3.2. Variable angle spectroscopic ellipsometry	53
<b>3.4. Structural characterisation techniques</b>	<b>54</b>
3.4.1. Atomic force microscopy	54
3.4.2. Grazing-incidence small-angle X-ray scattering	55
<b>4. Localized surface plasmons of noble metals</b>	<b>56</b>
<b>5. Silver metal island films on glass substrates</b>	<b>58</b>
<b>5.1. Optical characterisation of silver MIFs</b>	<b>58</b>
5.1.1. Spectrophotometry of silver MIFs	58
5.1.2. Variable angle spectroscopic ellipsometry of silver MIFs	62
<b>5.2. Structural characterisation of silver MIFs</b>	<b>64</b>
5.2.1. Atomic force microscopy of silver MIFs	64
5.2.2. GISAXS of silver MIFs	65
<b>6. Copper metal island films on glass substrates</b>	<b>69</b>
<b>6.1. Structural characterization of copper samples</b>	<b>69</b>
6.1.1. Atomic force microscopy of copper samples	69
6.1.2. GISAXS of copper samples	70
<b>6.2. Optical characterisation of copper samples</b>	<b>71</b>



<b>7. Gold metal island films on glass substrates</b>	<b>74</b>
7.1. Optical characterisation of gold MIFs	74
7.2. Structural characterisation of gold MIFs	80
7.2.1. Atomic force microscopy of gold MIFs	80
7.2.2. GISAXS of gold MIFs	82
<b>8. Gold metal island films in dielectric multilayers</b>	<b>86</b>
8.1. Optical characterization of embedded gold MIFs	86
8.2. Design of multilayer reflectors with gold MIFs	90
<b>9. Conclusions</b>	<b>93</b>
<b>Appendix: Different approaches in GISAXS analysis</b>	<b>95</b>
<b>References</b>	<b>100</b>
<b>List of symbols and abbreviations</b>	<b>111</b>

## Optical and Structural Properties of Ultrathin Films of Noble Metals

Martin Lončarić

“Ruđer Bošković” Institute, Bijenička cesta 54, Zagreb, Croatia

Ultrathin layers of noble metals obtained by deposition to the substrate during evaporation in high vacuum represent nanostructured matter. Nanoparticles showing interesting optical properties due to the localized surface plasmons are formed instead of homogenous layer. Optical properties of noble metal nanoparticles are closely related to their size, shape, distribution and dielectric environment. Localized surface plasmon properties may be tailored by changing deposition parameters (amount of material and substrate temperature) or by changing dielectric environment (dielectric layers below and/or above metal nanoparticles). The goal of research was to correlate optical and structural properties of noble metal island films. Results show that different combinations of ultrathin noble metal layers and dielectric layers have a potential for application in novel optical components.

**Keywords:** silver, copper and gold nanoparticles, localized surface plasmons, optical properties, structural properties, ellipsometry, GISAXS, multilayer reflectors with noble metal island films

**Supervisor:** Ph. D. Hrvoje Zorc

**Reviewers:** Professor Damir Veža, Ph. D. Hrvoje Zorc, Professor Hrvoje Buljan, Professor Joachim Krenn, Professor Marijan Šunjić

Thesis accepted: 10. 05. 2011.

Optička i strukturna svojstva ultratankih slojeva plemenitih metala

Martin Lončarić

Institut „Ruđer Bošković“, Bijenička cesta 54, Zagreb, Hrvatska

Ultratanki slojevi plemenitih metala srebra, bakra i zlata koji nastaju depozicijom na podlogu pri isparavanju u visokom vakuumu predstavljaju nanostrukturiranu tvar. Umjesto homogenog sloja, na podlozi se formiraju nanočestice koje pokazuju zanimljiva optička svojstva zbog pojave lokaliziranih površinskih plazmona. Optičke karakteristike slojeva nanočestica srebra, bakra i zlata u uskoj su vezi s njihovom veličinom, oblikom i raspodjelom te dielektričnom okolinom. Svojstva lokaliziranih površinskih plazmona mogu se kontrolirati na razne načine: npr. odabirom parametara depozicije (količina materijala i temperatura podloge) ili odabirom dielektrične okoline (dielektrični slojevi ispod i/ili iznad sloja nanočestica). Cilj disertacije je istraživanje korelacije optičkih i strukturnih svojstava ultratankih slojeva plemenitih metala. Rezultati ukazuju na zanimljive mogućnosti kombinacija nanočestica zlata u tankom sloju i dielektričnih materijala, od kojih se mogu očekivati inovativne optičke komponente raznih namjena.

Ključne riječi: nanočestice srebra, bakra i zlata, lokalizirani površinski plazmoni,  
optička svojstva, strukturna svojstva, elipsometrija, GISAXS,  
višeslojni reflektori sa slojevima nanočestica plemenitih metala

Mentor: dr. sc. Hrvoje Zorc

Ocjenjivači: prof. dr. sc. Mladen Veža, dr. sc. Hrvoje Zorc, prof. dr. sc. Hrvoje Buljan,  
prof. dr. sc. Joachim Krenn, prof. dr. sc. Marijan Šunjić

Rad prihvaćen: 10. 05. 2011.

# EXTENDED ABSTRACT IN CROATIAN LANGUAGE

## UVOD

Ultratanki slojevi plemenitih metala, srebra, bakra i zlata, na čvrstoj podlozi strukturno predstavljaju dvodimenzionalno raspoređene metalne nanočestice. Mogu se jednostavno proizvesti postupkom depozicije na čvrstu podlogu isparavanjem srebra, bakra ili zlata u visokom vakuumu. Optička svojstva nanočestica plemenitih metala vrlo su zanimljiva i posljedica su pojave lokaliziranih površinskih plazmona – koherentnih oscilacija slobodnih elektrona metalnih nanočestica koje nastaju pri interakciji sa svjetlom. Istraživanje optičkih svojstava metalnih nanočestica, za koja se pokazalo da su u uskoj vezi s njihovim strukturnim i morfološkim osobinama, otvorilo je područje znanosti koje se naziva plazmonika metalnih nanočestica. Razvoj plazmonike metalnih nanočestica potpomognut je pronalaženjem i usavršavanjem eksperimentalnih tehnika za dobivanje plazmoničkih struktura, primjenom naprednih mjernih metoda za njihovu karakterizaciju te pronalaženjem teorijskih modela i simulacijama optičkih svojstava kompleksnih nanostrukture. Ova se disertacija bavi istraživanjem optičkih svojstava te traženjem korelacije između optičkih i strukturnih svojstava ultratankih slojeva plemenitih metala. Optičke karakteristike ultratankih slojeva nanočestica srebra, bakra i zlata u uskoj su vezi s njihovom veličinom, oblikom i raspodjelom te dielektričnom okolinom.

Cilj istraživanja bio je odrediti vezu između optičkih i strukturnih svojstava ultratankih slojeva plemenitih metala srebra, bakra i zlata na podlogama od BK7 optičkog stakla, u kombinaciji s različitim dielektričnim okolinama (staklena podloga, slojevi  $\text{TiO}_2$  i  $\text{SiO}_2$  ispod i/ili iznad sloja metalnih nanočestica) te odrediti fizikalne parametre pripreme uzoraka potrebnih za dobivanje željenih optičkih svojstava.

Hipoteze su da su plazmonska svojstva (položaj apsorpcijske linije plazmona, njezina širina i intenzitet) nanočestica srebra, bakra i zlata u dobro definiranoj korelaciji s njihovim strukturnim parametrima te da se optička svojstva mogu dodatno modelirati odabirom odgovarajuće dielektrične okoline.

# EKSPERIMENT

Kao prvo, odlučeno je koje vrste uzoraka želimo istraživati, a koje možemo sami pripremiti s obzirom na dostupnu instrumentaciju. Uzorke smo proizveli metodom isparavanja srebra, zlata, bakra,  $\text{TiO}_2$  i  $\text{SiO}_2$  depozicijom na podloge od BK7 optičkog stakla u visokom vakuumu. Za pripremu je korišten evaporator s elektronskim topom Varian 3117 u Zavodu za laserska i atomska istraživanja i razvoj Instituta "Ruđer Bošković". Spomenuta oprema omogućuje kontrolu nominalne debljine deponiranog sloja pomoću kvarcne vage, grijanje podloga na različite temperature od sobne temperature do  $220\text{ }^\circ\text{C}$  te kontroliranu brzinu isparavanja upravljanjem strujom elektronskog topa. Nakon pripreme prvih uzoraka izvršena su preliminarna optička mjerenja transmitivnosti i reflektivnosti uzoraka koja su pokazala uz koje parametre su najizraženije fizikalne pojave koje želimo istraživati.

U svrhu optičke i strukturne karakterizacije uzoraka primijenili smo sljedeće tehnike:

a) *za optičku karakterizaciju*

– mjerenje transmitivnosti i reflektivnosti uzoraka radi određivanja koeficijenta ekstincije – spektrofotometrijska mjerenja u području valnih duljina između 200 nm i 1100 nm na instrumentu Perkin Elmer Lambda 25 u našem zavodu te mjerenja u području od 200 nm do 1700 nm na instrumentu Perkin Elmer Lambda 900 na Joanneum institutu u Weizu, Austrija,

– mjerenja spektroskopskom elipsometrijom pod različitim kutovima radi određivanja optičkih parametara – realnog i imaginarnog dijela indeksa loma i dielektrične funkcije te debljina slojeva – na elipsometru Woollam V-VASE na Joanneum institutu u Weizu te u našem zavodu nakon što smo dobili vlastiti elipsometar Woollam V-VASE s proširenim područjem valnih duljina do 2200 nm,

b) *za strukturnu karakterizaciju*

– pretražna mikroskopija atomskih sila (AFM – atomic force microscopy) na uređajima na Joanneum institutu u Weizu te na Institutu "Ruđer Bošković"

– mjerenja raspršenja X-zračenja pri malim upadnim kutovima oko kritičnog kuta na uzorcima (GISAXS – grazing-incidence small-angle X-ray scattering) radi dobivanja horizontalne i vertikalne veličine nanočestica te njihove udaljenosti – na SAXS liniji sinkrotrona Elettra u Trstu

Etape pripreme uzoraka i provođenja mjerenja izmjenjivale su se u iterativnom procesu uz analizu podataka nakon koje bi se pripremali uzorci uz promijenjene fizikalne parametre u procesu pripreme do postizanja odgovarajućih optičkih i strukturnih svojstava.

Rezultati mjerenja metodom GISAXS na sinkrotronu obrađivani su programskim alatima MATLAB (priprema mapa raspršenja X-zračenja za obradu te izračunavanje horizontalnih i vertikalnih veličina nanočestica te njihove međusobne udaljenosti primjenom Guinierove aproksimacije) i IsGISAXS (detaljno modeliranje strukturnih parametara metalnih nanočestica).

Rezultati pretražne mikroskopije atomskih sila obrađivani su programskim alatom Gwyddion, a najvažniji parametar dobiven primjenom te metode bio je međusobna udaljenost između čestica. On je uspoređivan s rezultatima koji su dobiveni nakon GISAXS raspršenja primjenom programa IsGISAXS.

Detaljno istraživanje optičkih parametara uz složeno modeliranje (realni i imaginarni dio indeksa loma odnosno realni i imaginarni dio dielektrične funkcije te ekvivalentne debljine sloja) provedeno je primjenom programskog alata Woollam WVASE32.

## **REZULTATI I DISKUSIJA**

Metode optičke spektroskopije, spektrofotometrija i elipsometrija, pokazale su da optičkim svojstvima ultratankih slojeva srebra, bakra i zlata na BK7 staklu dominira pojava lokaliziranih površinskih plazmona. Rezonancija lokaliziranih površinskih plazmona vidljiva je u spektrima kao izraženi apsorpcijski maksimum. Osim rezonancije lokaliziranih površinskih plazmona, kod uzoraka ultratankih slojeva zlata i bakra uočava se na višim energijama u spektru dodatna apsorpcija koju pripisujemo prijelazima između energijskih vrpci zlata i bakra. Kod uzoraka ultratankih slojeva zlata i bakra pripremljenih na nižim temperaturama i s većom količinom materijala, u infracrvenom dijelu spektra pojavljuje se pobuđenje karakteristično za postojanje slobodnih nosilaca naboja.

Pretražna mikroskopija atomskih sila pokazala je da su ultratanki slojevi srebra, bakra i zlata na BK7 podlogama u strukturnom smislu zapravo slojevi nanočestica na podlozi, a ne homogeni slojevi metala. To je u potpunom slaganju s postojanjem rezonancije lokaliziranih površinskih plazmona uočenom u optičkim svojstvima. Na slikama pretražne mikroskopije atomskih sila uzoraka kod kojih se u infracrvenom dijelu spektra pojavljuje pobuđenje karakteristično za metalnu vodljivost, jasno se uočava pojava perkolacije, odnosno spajanja nanočestica u veće, povezane nakupine koje počinju stvarati mrežu što omogućava električnu vodljivost u ravnini uzorka.

Kod uzoraka ultratankih slojeva srebra, bakra i zlata na BK7 staklu uočeni su sljedeći trendovi strukturno-morfoloških svojstava s promjenama parametara depozicije:

1. Povećanje veličine čestica i njihove udaljenosti s povećanjem nominalne debljine naparenog sloja. Ovaj trend može se objasniti grupiranjem klastera materijala u veće čestice s porastom količine naparenog materijala.
2. Povećanje veličine čestica i njihove udaljenosti s povećanjem temperature podloge pri naparavanju – rezultat je toga što je formiranje većih, više udaljenih čestica povezano s većom energijom dostupnom atomima materijala kada dolaze na jače zagrijanu podlogu.

Trendovi promjene optičkih svojstava s promjenom parametara depozicije uzoraka su:

1. Pomak prema manjim energijama, širenje apsorpcijske linije plazmona i porast njezinog intenziteta s povećanjem debljine naparenog sloja (primjenom Maxwell Garnettovog modela na sloj nanočestica srebra sa zaštitnim tankim slojem  $\text{SiO}_2$ , promatran kao mješavina metalnih nanočestica i dielektrične okoline, dobivaju se optički parametri koji pokazuju porast apsorpcijskog maksimuma uz širenje linije i pomak prema manjim energijama s povećanjem debljine sloja).
2. Pomak prema većim energijama i suženje apsorpcijske linije plazmona s porastom temperature – može se objasniti kao rezultat kombinacije morfoloških trendova s povećanjem temperature (povećanje sferičnosti čestica, njihove veličine i međusobne udaljenosti) što uzrokuje pomak prema većim energijama i širenje plazmonske linije

Za optičku karakterizaciju ultratankih slojeva srebra, bakra i zlata primijenjena je spektroskopska elipsometrija s različitim kutovima upada snopa svjetlosti na uzorak. Napravljena je prilagodba eksperimentalno dobivenih elipsometrijskih kutova  $\Psi$  i  $\Delta$  onima koje daje model, uz modeliranje sloja nanočestica kao homogenog sloja s efektivnim optičkim parametrima ( $\varepsilon_1$ ,  $\varepsilon_2$ ) i debljinom ( $d_{\text{eff}}$ ) uz uporabu oscilatora za opisivanje različitih pobuđenja u spektru (Kramers-Kronig konzistentno).

Pokazalo se da je dovoljan jedan Gaussov oscilator na položaju plazmonske rezonancije te dodatni oscilatori za energijske prijelaze između energijskih vrpca (jedan kod srebra i dva kod zlata) za opis optičkih svojstava uzoraka nastalih pri višim temperaturama podloge uz manju nominalnu debljinu sloja. Kod uzoraka nastalih pri nižim temperaturama uz veću nominalnu debljinu sloja nema lijepo formiranih nanočestica već se vide povezana područja metala. Za modeliranje su potrebni dodatni oscilatori – zbog nehomogenog širenja plazmonske apsorpcije i radi opisivanja ponašanja sličnog makroskopskom metalu pri niskim frekvencijama (električna vodljivost).

## ZAKLJUČCI

Optička svojstva ultratankih slojeva plemenitih metala srebra, bakra i zlata na podlogama od optičkog stakla, kojima dominira pojava lokaliziranih površinskih plazmona, mogu se kontrolirati odabirom uvjeta pri postupku naparavanja (temperatura i količina naparenog materijala/nominalna debljina sloja).

Kombinacija primijenjenih eksperimentalnih tehnika (spektrofotometrija i spektroskopska elipsometrija s različitim upadnim kutovima snopa svjetlosti kao tehnike optičke spektroskopije te pretražna mikroskopija atomskih sila i GISAXS kao tehnike koje daju uvid u strukturalna svojstva uzoraka) omogućuje određivanje veze između strukturalnih i optičkih svojstava istraživanih uzoraka. Spektroskopska elipsometrija pod različitim kutovima uz opisani model (kombinacija oscilatora za opisivanje različitih fizikalnih pobuđenja u sustavu) daje potpunu optičku karakterizaciju uzoraka.

Rezultati optičke karakterizacije poslužili su kao prvi korak u modeliranju višeslojnih sustava – slojeva nanočestica zlata između slojeva dielektrika  $\text{SiO}_2$  i  $\text{TiO}_2$  s ciljem dizajniranja inovativnih optičkih komponenata. Ultratanki slojevi zlata uspješno su upotrijebljeni u dizajnu reflektora visokog sjaja.



# 1. Introduction

Nanoscience and nanotechnology are tremendously increasing fields of research that aim at producing, characterizing and understanding nano-objects and assemblies of nano-objects. Their new physical or chemical properties that arise from confinement effects closely depend on their morphological properties, i.e. their shapes, their sizes and their spatial organization.

Nanomaterials are widely seen as having a huge potential to bring benefits to many areas of research and application. Therefore, they attract fast growing investments. Nanomaterials are defined as having at least one dimension in the nanometre range (1 nm–100 nm). Their properties may significantly differ from those at a larger scale for two main reasons. At first, confinement effects, usually quantum effects, dominate the behaviour of matter at the nanoscale affecting the structural, optical, electrical and magnetic properties of materials. Secondly, nanomaterials have a relatively larger surface area when compared to the same mass of macroscopic material. This can make them more chemically reactive (in some cases materials that are inert in their macroscopic form are reactive when produced in their nanoscale form), and influence their strength or electrical properties.

Nanoscience and nanotechnologies are already present for several decades, but advances in the production and characterization tools have allowed materials to be examined with great precision and enabling the expansion and further developments in this field. The field is today not restricted to physics and chemistry, but it is also involved in life sciences. Recent industrial developments are clearly targeted at introducing nanostructures into everyday life. For instance the ongoing trend of miniaturization in electronics has reached the nanometre scale, where the phenomena such as tunnelling, band structure or photon emission are determined by confinement effects (size, morphology, atomic structure and composition). The past years have thus been marked by the elaboration and study of materials on nanometric scale, such as 2D layers or multilayers, 1D nanowires, 0D nanoparticles, such as quantum dots, or buried aggregates. The properties of interest can be tuned by confining phenomena in objects where at least one dimension is smaller than a typical bulk length scale.

One field with a lot of interest and impact in nanoscience and nanotechnology is plasmonics. The term plasmon refers to collective oscillations of conduction electrons in plasmonic materials, i.e. oscillations of charge density. Plasmonic effects are based on interaction processes between electromagnetic radiation and conduction electrons at metallic interfaces or in small metallic nanostructures, leading to an enhanced optical near field of sub-wavelength dimensions. Thus, it makes plasmonics a major part of the fascinating field of nanophotonics, which explores how electromagnetic fields can be confined within dimensions on the order of or smaller than the wavelength.

The history of plasmonics dates back to Roman times, with application of metallic nanoparticles for the staining of glass [1]. The exquisite Lycurgus cup from the fourth century A. D. represents one of the outstanding achievements of the ancient glass industry [2], owing its unusual optical effects to gold nanoparticles in the glass (in daylight the cup appears a greenish colour, but if illuminated from the inside it glows in ruby). Plasmonics also provides a bridge to the future – optical metamaterials (manmade structures with ‘unnatural’ properties). By combining the modern form of a Roman technology with ideas from ancient Greece, cloaking devices for visible light come a step closer to reality [3]. Cai et al. presented theoretical simulations that show that a modified Roman cup based on modern nanofabrication technology will act as an invisibility device [4].

The clear mathematical foundation of two main concepts of plasmonics, surface plasmon polaritons and localized surface plasmons have been clearly described at the beginning of the 20<sup>th</sup> century [5-7], but the wealth of phenomena and applications of this field together with recent experimental and technological possibilities drive its development further.

There are numerous exciting applications of plasmonics: optical applications – polarisers [8, 9], data storage [10, 11], chemical and biological sensing [12, 13], second harmonic generation [14], surface enhanced spectroscopy [15-18], novel solar cells [19-23], drug delivery and cancer treatment [24-27] etc. Guiding light in integrated optical systems and interfacing with electronic components remain important challenges for research and development in plasmonics today and nanostructured metals are believed to be one of the key ingredients of such future optoelectronic devices [28, 29].

In this thesis, central physical phenomenon is localized surface plasmon (LSP) resonance in nanoparticles of noble metal island films. Metal island films (MIFs) consist of metal clusters deposited on a substrate surface and represent one of the most basic cases of nanostructured matter. They can be obtained by thin film techniques such as evaporation, when the deposited mass thickness is in the range of few nanometres and the film's growth is characterized by the formation of islands, typical for the Volmer-Weber growth mode. MIFs show unique optical properties due to the LSP resonance of the clusters, i.e. resonant charge density oscillations in clusters excited by light. Optical properties of metal nanoparticles are strongly dependent on their size, shape, distribution and dielectric environment [30]. Thus, LSP properties of MIFs may be tailored by changing deposition parameters (amount of material, substrate temperature and deposition rate) [31, 32] or by changing dielectric environment (different dielectric environment around metal nanoparticles) [33, 34]. Also, the LSP properties of MIFs can be tailored by post-deposition treatments (e.g. irradiation with laser light [35] and high-temperature annealing [36]). Further tuning of the LSP resonance over a wide energy range can be obtained using bimetallic nanoparticles (e.g., gold-silver), either as core-shell or as alloyed structure [37-39]. Due to this capacity of tailoring the optical properties, MIFs are interesting for various applications. I would like to mention a surface plasmon related technique investigated by our research group – the electric field assisted dissolution of metal nanoparticles (EFAD) [40]. Owing to its simplicity and inexpensive technical requirements, EFAD represents an attractive possibility for production of low-cost plasmon-based two-dimensional [41] and three-dimensional [42] photonic structures.

In order to tailor the LSP properties of MIFs for applied purposes, it is necessary to understand the link between the deposition conditions and the geometrical structure of the MIF. The influence of two fabrication parameters (substrate temperature and mass thickness of deposited metal) in the MIF optical behaviour was analysed in this thesis. MIFs were characterised with grazing-incidence small-angle X-ray scattering (GISAXS), atomic force microscopy (AFM) and optical spectroscopy in UV-VIS-NIR range. In addition it is required to establish a correlation between the observed structure of the MIF and its optical properties.

Initially, the focus is on the properties of silver, copper and gold MIFs deposited by electron beam evaporation on glass substrates. The structural and optical characterization of the samples evidences that the evolution of LSP characteristics with the fabrication parameters is explained by the differences in the concentration, shape and size of the islands, and their dielectric environment.

We have investigated which model can correctly describe the effective optical constants of MIFs. One way to describe the optical behaviour of MIFs is by modelling the MIF as a homogeneous layer with effective optical constants and thickness [43]. Effective optical constants of MIFs are necessary in designing complex multilayers incorporating metal nanoparticles [44]. Also, they offer insight to different physical phenomena connected to MIFs, such as LSP resonance, size effects in nanostructured matter, percolation etc. Optical constants are usually determined by fitting of experimental data to some parametric dispersion model. Unlike many materials for which standard dispersion model exist, MIFs are usually modelled by effective medium theories (EMTs), which only roughly describe their optical behaviour [45]. Another approach is to use first principles calculations [46, 47] which are too complex to be incorporated in a fitting procedure. Various approaches were tested in this thesis and the conclusion is that the effective optical constants of MIFs were well described using a multiple oscillator approach that can take into account different light-matter interaction phenomena which occur in the investigated spectral range.

Structural properties of MIFs were assessed using AFM and GISAXS as experimental techniques. After investigating different materials, gold was chosen for further use in the analysis of MIFs embedded in dielectric multilayers. For this reason, approach far beyond simple Guinier's approximation was applied to investigate and describe gold MIFs' structure and morphology. The connection between optical properties of gold MIFs elaborated in the preceding part of the study, and MIFs' structure and morphology was established.

Next, the influence of surrounding medium that changes the original behaviour of LSP was of a particular interest. Understanding the influence of surrounding media influence to plasmonic oscillations is of crucial importance for the further multilayer design containing metal island films. We have thoroughly characterized the LSP resonances and optical characteristics of gold island films embedded between SiO<sub>2</sub> and/or TiO<sub>2</sub> dielectric films.

The last part of this thesis makes a bridge between acquired knowledge about optical and structural properties of noble metal island films and a possible field of application of this knowledge. The obtained data was used for the design of optical multilayers containing MIFs. Gold MIFs were used in the design of reflectors with high luminosity.

The present dissertation is structured as follows: After general Introduction, in the Chapter 2 some theoretical aspects of interaction of light with-matter are presented, introduction to the field of plasmonics is given, with the emphasis on the plasmons in noble metal island films, and physical basis of variable angle spectroscopic ellipsometry and grazing-incidence small-angle X-ray scattering are given. In Chapter 3, experimental aspects of the research are presented: sample preparation, optical and structural characterisation techniques used. In Chapter 4, the results of optical measurements using spectrophotometry on silver, copper and gold MIFs are shown with the aim to illustrate the main physical phenomenon – localised surface plasmon resonance common to all samples. Next three chapters are devoted to presentation of results obtained in the MIF analysis using particular noble metal: Chapter 5 to silver, Chapter 6 to copper and Chapter 7 to gold. The final chapter before the Conclusions, Chapter 8, brings the results of using gold MIFs embedded in dielectric multilayers.

## 2. Theoretical background

The main subjects of this thesis are optical and structural properties of ultrathin films of noble metal nanoparticles (silver, copper and gold) on dielectric substrate (BK7 borosilicate glass) and the influence of embedding dielectric environment ( $\text{SiO}_2$  and  $\text{TiO}_2$  layers below/above nanoparticle layer).

The theoretical background is presented to enable a proper interpretation of the diverse phenomena of interest. The first part of this chapter describes physical processes which happen during particle growth. In the second part of this chapter the basic concepts of electrodynamics and solid state theory needed for understanding the optical properties of metal nanostructures are presented.

### 2.1. Noble metal nanoparticle growth

Various experimental techniques are developed for production of thin solid films such as PVD, CVD, sputtering, sol-gel etc. Our samples were prepared with electron beam evaporation. Particles impinging to the substrate have kinetic energy of the order of less than 1 eV. The following atomic processes take place on a substrate: adsorption, diffusion, desorption, nucleation and island growth [48]. They are governed by specific activation energies. The first step is the adsorption of an incoming metal particle on the substrate. The attractive term of the surface potential along its normal is, in this case, governed by van der Waals force. In order to stick, the particle should be thermally accommodated on the substrate. Once adsorbed, the particles diffuse and nucleate on the surface. When the saturation density of nuclei is reached, the growth of formed aggregates takes place.

For thin film growth on a substrate there are three different growth modes, represented schematically in Figure 2.1 [49].

- Volmer-Weber or three-dimensional island growth mode. If the binding energy between adatoms is higher than the binding energy between adatoms and the substrate, the growth process leads to aggregation of atoms and particle growth. This is generally the case with metals grown on oxides [50, 51].

- Frank-van-der-Merwe or layer-by-layer growth mode, displays the opposite behaviour. Because the atoms are more strongly bound to the substrate than to each other, the adatoms condense completing layers on the surface.
- Stranski-Krastanov or layer-plus-island growth mode. It consists of an intermediate case. After the formation of one or a few monolayers, layer growth is not favourable anymore and islands are formed on top of the last monolayer.

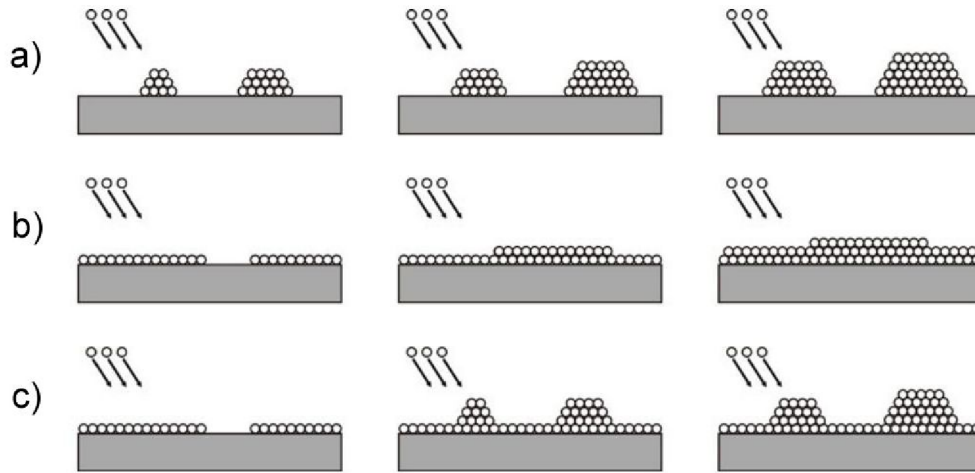


**Figure 2.1** Schematic representation of the three different growth modes: a) Volmer-Weber, b) Frank-van-der-Merwe and c) Stranski-Krastanov.

The nanoparticle growth is a process far from thermodynamic equilibrium. The kinetics of growth, rather than thermodynamics, determines the final film morphology. Nevertheless, thermodynamic considerations can be applied being kinetically rate-limited.

Under conditions of thermodynamic equilibrium, the film growth mode is determined by the help of the surface free energies of the metal ( $\gamma_{\text{met}}$ ), the substrate ( $\gamma_{\text{sub}}$ ) and of the metal-substrate interface ( $\gamma_{\text{int}}$ ).

If the following condition is met,

$$\gamma_{\text{int}} + \gamma_{\text{met}} \leq \gamma_{\text{sub}}, \quad (2.1)$$

the formation of a metal-substrate interface is thermodynamically favourable and the metal wets the surface at equilibrium which corresponds to a layer-by-layer or two-dimensional growth mode. In the opposite case, when the formation of a metal-substrate interface is thermodynamically unfavourable, the metal is expected to form three-dimensional aggregates.

$E_{\text{adh}}$  is the adhesion energy given by:

$$E_{\text{adh}} = \gamma_{\text{met}} + \gamma_{\text{sub}} - \gamma_{\text{int}}. \quad (2.2)$$

The strength of the metal-substrate interaction is given by the relation between the adhesion energy and the surface free energy of the metal,  $E_{\text{adh}}/\gamma_{\text{met}}$ . This ratio is indicated for gold, silver and copper on  $\text{SiO}_2$  and  $\text{TiO}_2$  substrates in Table 2.1.

**Table 2.1** Ratio  $E_{\text{adh}}/\gamma_{\text{met}}$  for the materials used in this research [52].

	$\text{SiO}_2$	$\text{TiO}_2$
<b>Au</b>	0.202 – 0.219	0.455 – 0.485
<b>Ag</b>	0.188 – 0.214	
<b>Cu</b>	0.384	

With the increase of metal-substrate interaction, particles become more flat. However, the final shape is limited by kinetics considerations.

The most important processes during the early stage of growth have been discussed up to this point. Further stage of growth is characterized by a decrease of the density of particles and an increase in their size. This process is referred to as coarsening of aggregates. There are three different mechanisms which lead to particle coarsening:

- 1) Coalescence by growth – when two particles get in contact during their growth, they show a liquid-like behaviour and coalesce to a single one;
- 2) Coalescence by cluster mobility, i.e. cluster migration – surface diffusion of clusters and their collision lead to particle coalescence; and
- 3) Ostwald ripening – the surface free energy of an aggregate is larger if its size is smaller and, as a result, large particles will grow at expense of smaller clusters.

In contrast to the first two cases, contact between the particles in Ostwald ripening is not necessary. When the adhesion of the particles to the substrate surface is low, coalescence due to cluster mobility leads to particle coarsening. In the case of strong adhesion, Ostwald ripening dominates. Reviews of the processes involved in nucleation and growth of thin films are available in [48, 50, 51].



## 2.2. Interaction of light with matter

Any optical phenomenon is connected with the interaction of electromagnetic radiation with matter. This interaction may be theoretically treated at different levels. One may use the purely classical description, where applicable, or resort to quantum mechanical theory. In semi-classical approach, the fields are treated within the framework of Maxwell's theory, while the properties of matter are described in terms of quantum mechanical models. Semi-classical theory is enough to describe the phenomena discussed in this study and there is no need to go to more advanced theory. Maxwell's equations are used in classical approach and in semi-classical approach.

### 2.2.1. Maxwell's equations in matter

Maxwell's equations are fundamental equations governing the evolution of electromagnetic fields in the presence of charges, currents and polarisable media:

$$\nabla \cdot \mathbf{D} = \rho_{\text{ext}}, \quad (2.3)$$

$$\nabla \cdot \mathbf{B} = 0, \quad (2.4)$$

$$\nabla \times \mathbf{E} = -\frac{\partial \mathbf{B}}{\partial t}, \quad (2.5)$$

$$\nabla \times \mathbf{H} = \mathbf{J}_{\text{ext}} + \frac{\partial \mathbf{D}}{\partial t}. \quad (2.6)$$

These equations link the four macroscopic fields  $\mathbf{E}$  (the electric field),  $\mathbf{D}$  (the electric displacement),  $\mathbf{B}$  (the magnetic induction) and  $\mathbf{H}$  (the magnetic field) with the external charge and current densities  $\rho_{\text{ext}}$  and  $\mathbf{J}_{\text{ext}}$ . We distinguish between external ( $\rho_{\text{ext}}$ ,  $\mathbf{J}_{\text{ext}}$ ) and internal ( $\rho$ ,  $\mathbf{J}$ ) charge and current densities. The external set drives the system, while the internal set responds to the external stimuli. In total  $\rho_{\text{tot}} = \rho_{\text{ext}} + \rho$  and  $\mathbf{J}_{\text{tot}} = \mathbf{J}_{\text{ext}} + \mathbf{J}$ .

The advantage of macroscopic Maxwell's equations, i.e. a phenomenological approach, is that details of the fundamental interactions between charged particles inside media and electromagnetic fields need not be taken into account, since rapidly varying microscopic fields are averaged over distances much larger than the underlying microstructure.

If we denote the local electric polarization of matter with  $\mathbf{P}$  and the local magnetization with  $\mathbf{M}$ , the four macroscopic fields are linked as:

$$\mathbf{D} = \varepsilon_0 \mathbf{E} + \mathbf{P}, \quad (2.7)$$

$$\mathbf{H} = \frac{1}{\mu_0} \mathbf{B} - \mathbf{M}, \quad (2.8)$$

where  $\varepsilon_0 = 8.854 \cdot 10^{12} \text{Fm}^{-1}$  is the electric permittivity of vacuum and  $\mu_0 = 4\pi \cdot 10^{-7} \text{NA}^{-2}$  is the magnetic permeability of vacuum. We will consider only nonmagnetic ( $\mathbf{M} = 0$ ) materials.  $\mathbf{P}$  is the electric dipole moment per unit volume inside material and is related to the internal charge density via  $\nabla \cdot \mathbf{P} = -\rho$ . The condition of charge conservation  $\nabla \cdot \mathbf{J} = -\partial\rho/\partial t$  implies the following link between internal charge and current densities:

$$\mathbf{J} = \frac{\partial \mathbf{P}}{\partial t}. \quad (2.9)$$

The equations describing the response of material in case of linear, isotropic and nonmagnetic media, the constitutive relations are:

$$\mathbf{D} = \varepsilon_0 \varepsilon \mathbf{E}, \quad (2.10)$$

$$\mathbf{B} = \mu_0 \mu \mathbf{H}, \quad (2.11)$$

$$\mathbf{J} = \sigma \mathbf{E}. \quad (2.12)$$

The phenomenological coefficients are:  $\varepsilon$  (dielectric constant or relative permittivity),  $\mu = 1$  (the relative permeability of the nonmagnetic medium) and  $\sigma$  (conductivity). The linear relationship between  $\mathbf{D}$  and  $\mathbf{E}$  is also implicitly defined using dielectric susceptibility  $\chi$  which describes linear relationship between  $\mathbf{P}$  and  $\mathbf{E}$

$$\mathbf{P} = \varepsilon_0 \chi \mathbf{E}. \quad (2.13)$$

Using (2.7) and (2.13) we obtain

$$\varepsilon = 1 + \chi. \quad (2.14)$$

Charges are additive, and, as a result, all polarization mechanisms present in real matter will contribute their dipole moments to the final polarization, which is a sum of all dipole moments in the medium. Contributions may come from free electrons, from bound electrons, from positive ion cores and from permanent dipoles if they are present.

The susceptibilities that correspond to different polarization mechanisms (signed by index  $j$ ) add up to the full susceptibility and the dielectric function becomes

$$\varepsilon = 1 + \sum_j \chi_j \quad (2.15)$$

where  $\chi_j$  are the susceptibilities of corresponding groups of dipoles.

In the macroscopic picture, if there is a macroscopic electric field  $\mathbf{E}$  in a material of electric susceptibility  $\chi$  the result is polarization  $\mathbf{P}$ . In the microscopic description, the polarization is the sum of all dipole moments  $\mathbf{p}$  in unit volume, where each dipole moment is induced by the local electric field  $\mathbf{E}_{\text{local}}$  at the dipole site, that is,

$$\mathbf{P} = N\mathbf{p} = N\alpha\mathbf{E}_{\text{local}}, \quad (2.16)$$

where  $\alpha$  represents the local microscopic polarizability and  $N$  is the number of dipoles per unit volume.

The local electric field  $\mathbf{E}_{\text{local}}$  differs from macroscopic electric field  $\mathbf{E}$  and it may be shown that at a site inside a simple cubic crystal the connection between these two fields is [53]:

$$\mathbf{E}_{\text{local}} = \mathbf{E} + \frac{1}{3\varepsilon_0} \mathbf{P}. \quad (2.17)$$

Using equations from (2.13) to (2.17), the following relationship between macroscopic ( $\varepsilon$ ) and microscopic ( $\alpha$ ) material properties of a medium may be derived [53]:

$$\frac{\varepsilon - 1}{\varepsilon - 2} = \frac{1}{3\varepsilon_0} N\alpha, \quad (2.18)$$

which is known as the Clausius-Mossotti relation. It expresses the fact that measurements on macroscopic scale, which yield the optical constants of material, give further access to microscopic parameters such as atomic polarizability.

If we want to properly take into consideration temporal or spatial dispersion, we have to generalize (2.10) and (2.12) (assuming homogeneity of the medium)

$$\mathbf{D}(\mathbf{r}, t) = \varepsilon_0 \int dt' d\mathbf{r}' \varepsilon(\mathbf{r} - \mathbf{r}', t - t') \mathbf{E}(\mathbf{r}', t'), \quad (2.19)$$

$$\mathbf{J}(\mathbf{r}, t) = \int dt' d\mathbf{r}' \sigma(\mathbf{r} - \mathbf{r}', t - t') \mathbf{E}(\mathbf{r}', t'). \quad (2.20)$$

We can decompose the fields into individual plane-wave components of wave vector  $\mathbf{k}$  and angular frequency  $\omega$  according to:

$$\mathbf{D}(\mathbf{r}, t) = \int \mathbf{D}(\mathbf{k}, \omega) e^{i(\mathbf{k}\cdot\mathbf{r} - \omega t)} \mathbf{d}\mathbf{r} d\omega, \quad (2.21)$$

$$\mathbf{E}(\mathbf{r}, t) = \int \mathbf{E}(\mathbf{k}, \omega) e^{i(\mathbf{k}\cdot\mathbf{r} - \omega t)} \mathbf{d}\mathbf{r} d\omega. \quad (2.22)$$

This leads to constitutive relations in the Fourier domain

$$\mathbf{D}(\mathbf{k}, \omega) = \varepsilon_0 \varepsilon(\mathbf{k}, \omega) \mathbf{E}(\mathbf{k}, \omega), \quad (2.23)$$

$$\mathbf{J}(\mathbf{k}, \omega) = \sigma(\mathbf{k}, \omega) \mathbf{E}(\mathbf{k}, \omega). \quad (2.24)$$

Using (2.10), (2.12), (2.23) and (2.24) we can relate dielectric function and the conductivity

$$\varepsilon(\mathbf{k}, \omega) = 1 + \frac{i\sigma(\mathbf{k}, \omega)}{\varepsilon_0 \omega}. \quad (2.25)$$

If the wavelength of electromagnetic field in the material is significantly larger than all characteristic microscopic dimensions,  $\varepsilon(\mathbf{k}, \omega)$  can be approximated by spatially local response  $\varepsilon(\mathbf{k} = 0, \omega) = \varepsilon(\omega)$ . At low frequencies,  $\varepsilon$  is usually used for the description of the response of bound charges to a driving field, resulting in electric polarization, while  $\sigma$  describes the response of free charges, resulting in the current flow. At optical frequencies, however, there is no more clear distinction between bound and free charges.

Maxwell's equations can be used to derive wave equations which have travelling wave solutions. If we combine (2.5) and (2.6) in case that there are no external stimuli, we obtain the following wave equations:

$$\nabla(\nabla \cdot \mathbf{E}) - \nabla^2 \mathbf{E} = -\mu_0 \frac{\partial^2 \mathbf{D}}{\partial t^2} \quad \text{in the time domain,} \quad (2.26)$$

$$\mathbf{K}(\mathbf{K} \cdot \mathbf{E}) - K^2 \mathbf{E} = -\varepsilon(\mathbf{K}, \omega) \frac{\omega^2}{c^2} \mathbf{E} \quad \text{in the Fourier domain.} \quad (2.27)$$

We can distinguish between transverse electromagnetic waves ( $\mathbf{K} \cdot \mathbf{E} = 0$ ), with dispersion relation

$$K^2 = \varepsilon(\mathbf{K}, \omega) \frac{\omega^2}{c^2}, \quad (2.28)$$

and longitudinal electromagnetic waves for which  $\varepsilon(\mathbf{K}, \omega) = 0$ .

The above sets of equations, together with appropriate boundary conditions, are sufficient to solve the time and spatial evolution of electromagnetic fields in the presence of matter.

## 2.2.2. Optical properties of materials

As elaborated in previous section, a dielectric function  $\varepsilon$  or conductivity  $\sigma$  may be used to describe the optical properties which determine how light interacts with a material. They are generally represented as complex numbers:

$$\tilde{\varepsilon}(\omega) = \varepsilon_1(\omega) + i\varepsilon_2(\omega), \quad (2.29)$$

$$\tilde{\sigma}(\omega) = \sigma_1(\omega) + i\sigma_2(\omega). \quad (2.30)$$

Alternatively, the optical properties can be described using complex refractive index  $\tilde{n}$  which consists of the refractive index  $n$  and extinction coefficient  $k$ :

$$\tilde{n}(\omega) = n(\omega) + ik(\omega), \quad (2.31)$$

with the following relation between conventions:

$$\tilde{\varepsilon} = \tilde{n}^2. \quad (2.32)$$

The refractive index  $n$  describes the phase velocity of light  $v$  as it travels in a material compared to the speed of light in vacuum,  $c$ :

$$v = \frac{c}{n}. \quad (2.33)$$

Light slows as it enters a material with higher refractive index. The extinction coefficient  $k$  describes the loss of wave energy by absorption and scattering in the material (optical extinction is a result of both absorption and scattering). It is related to the absorption coefficient  $\alpha_{ext}$ ,<sup>1</sup> as:

$$\alpha_{ext}(\omega) = \frac{2k(\omega)\omega}{c} = \frac{4\pi k(\omega)}{\lambda}. \quad (2.34)$$

The intensity of light decreases in a material by optical extinction according to Beer's Law:

$$I(z) = I(0)e^{-\alpha_{ext}z}, \quad (2.35)$$

where  $z$  is the propagation distance of light in the medium. Thus, the extinction coefficient indicates how the intensity of light decreases through propagation in a material.

---

<sup>1</sup> Absorption coefficient  $\alpha_{ext}$  has to be differentiated from polarizability  $\alpha$ .

The dielectric function represents the degree to which the material may be polarized by an applied electric field. The imaginary part of the dielectric function has the useful property of being directly proportional to the amount of field power absorbed per unit time and unit volume at a point in the material. This is a natural quantity to be calculated from physical absorption models.

The optical constants  $n$  and  $k$  (the real and imaginary parts of the complex refractive index) represent the optical properties of a material in terms of how an electromagnetic wave will propagate in that material. They actually contain the same information as dielectric function. Both types of optical constants are commonly encountered in the literature and the choice of optical constant type is generally determined by the application.

As a result of causality (the requirement that a material cannot respond to an applied electric field before the field is actually applied), the dielectric function and the optical constants depend on light frequency  $\omega$  (dispersion). The dispersions of the real and imaginary parts of the dielectric function are related to each other by integral transformations called the Kramers-Kronig relations:

$$\varepsilon_1(\omega) = 1 + \frac{2}{\pi} P \int_0^{\infty} \frac{\varepsilon_2(\omega') \omega'}{\omega'^2 - \omega^2} d\omega', \quad (2.36)$$

$$\varepsilon_2(\omega) = -\frac{2\omega}{\pi} P \int_0^{\infty} \frac{\varepsilon_1(\omega') - 1}{\omega'^2 - \omega^2} d\omega', \quad (2.37)$$

where  $P$  denotes the principal (Cauchy) value of integral.

It follows from Kramers-Kronig relations that if the imaginary part of the dielectric function is known over the entire spectrum, its real part may be evaluated from (2.36) (and vice versa, if real part is known, imaginary may be evaluated using (2.37)). If we recall the connection between light wave frequency and photon energy  $E = \hbar\omega$ , the denominators of the (2.36) and (2.37) indicate that the integrand does not contribute significantly unless  $E' = \hbar\omega'$  is fairly close to  $E = \hbar\omega$ , so that absorption processes far from the photon energy of interest do not contribute strongly.

The optical properties of all materials are determined completely by the types and strengths of the optical absorption processes that occur in the material. Three primary mechanisms by which energy is absorbed from a light beam by solid state matter are:

### **Interband absorption**

Interband absorption is optical absorption which occurs when an electron in a bound state in the material absorbs a single photon from the light beam and jumps to a higher energy level in the material. This process may occur as stated, with the electron's crystal momentum remaining unchanged, or absorption and/or emission of a phonon may also occur in such way that the crystal momentum of the electron changes as well. Semiconducting and dielectric materials exhibit an energy gap in their band structure, with the Fermi level of the material lying somewhere within the bandgap. Thus, interband absorption will not occur for such materials until the photon energy exceeds the energy difference between the highest occupied electron energy level and the lowest unoccupied electron energy level. If these two levels occur for the same value of the crystal momentum, the onset of absorption occurs with direct transitions, requiring no change in the crystal momentum. This is the case, for example, for GaAs. If the highest occupied and lowest unoccupied levels occur at different crystal momenta, the onset of absorption occurs through indirect transitions, requiring the emission and/or absorption of a phonon for conservation of both crystal momentum and energy. Absorption, due to interband transitions, dominates the optical spectra in the UV-VIS-NIR for nearly all semiconducting and dielectric materials. It may be well described using Lorentz oscillator model (elaborated in further sections). Metals exhibit interband absorption structure in the optical constants as well, but also show strong absorption effects due to the absorption of photons by free carriers – electrons.

### **Intraband absorption**

A second important type of optical absorption is intraband absorption, in which an electron absorbs a photon from the light beam but jumps to a different energy state within the same band. This process requires the emission or absorption of a phonon unless the initial and final electron states occur at identical values of the crystal momentum. A special case of intraband absorption is absorption by free carriers.

## **Free carrier absorption**

Metals and other conducting materials contain a ‘sea’ of conductors which are not bound to any specific atom or location within the material. These free carriers exhibit a distinctive optical absorption, which may be derived by solving for the trajectories of free carriers under the influence of a driving electromagnetic field. The Drude model for metals successfully describes free carrier optical absorption. Drude model will be presented in following sections together with Lorentz oscillator model for dielectrics and semiconductors. The Drude model may be obtained as a special case of a single Lorentz oscillator with the centre energy fixed at zero. This is due to the fact that metals exhibit no band gap, as the Fermi energy for a metal lays within one of the electron energy bands.

### **2.2.3. Optical properties of dielectric materials and semiconductors**

Dielectric materials and semiconductors are equivalent for purposes of discussing their optical properties. The optical constant spectra of a typical semiconductor or dielectric may be divided into two distinct spectral regions. The first region extends from the photon energy where the material begins to absorb to higher energies. The onset of absorption is due to the onset of interband transitions above the band gap energy, and the material will usually be absorbing for all energies higher than the energy at which absorption begins to occur. Near the onset energy, the extinction coefficient (and imaginary part of the dielectric function) tends to increase abruptly with energy, but may show complicated dispersion as the energy increases due to contributions from many different interband transitions. At photon energies less than the band gap energy, the extinction coefficient (and imaginary part of the dielectric function) will be zero, and the refractive index decreases slowly and monotonically with decreasing photon energy. The refractive index cannot show strong dispersion in this region, as previously discussed with respect to the Kramers-Kronig relations.

It should be pointed out that the refractive index (and the real part of the dielectric function) of a material should never increase with decreasing photon energy (or increasing wavelength) if the extinction coefficient (and the imaginary part of the dielectric function) of the material in the spectral range of interest is zero. This is very useful for identifying physically acceptable results in model dependent optical characterisation techniques such as ellipsometry when fitting for the refractive index of transparent films.



A simplified, classical model for the behaviour of electrons in dielectrics will be presented with the aim to deduce the frequency-dependence of the dielectric function. The electrons in a non-conductor are bound to specific sites. The actual binding forces can be quite complicated, but we shall picture each electron as attached to its site by binding force of force constant  $k_{\text{restoring}}$  :

$$F_{\text{binding}} = -k_{\text{restoring}}x = -m\omega_0^2x, \quad (2.38)$$

where  $m$  is electron mass,  $x$  is the displacement and  $\omega_0$  is the natural oscillation frequency.

There will presumably be some damping force on electron:

$$F_{\text{damping}} = -m\gamma\frac{dx}{dt}. \quad (2.39)$$

In the presence of an electromagnetic wave of frequency  $\omega$ , amplitude  $E_0$ , polarized in the  $x$  direction, the electron with charge  $q$  is subject to a driving force

$$F_{\text{driving}} = qE = qE_0\cos(\omega t). \quad (2.40)$$

Newton's second law now gives

$$m\frac{d^2x}{dt^2} = F_{\text{total}} = F_{\text{binding}} + F_{\text{damping}} + F_{\text{driving}} \quad (2.41)$$

or as the real part of complex equation

$$\frac{d^2\tilde{x}}{dt^2} + \gamma\frac{d\tilde{x}}{dt} + \omega_0^2\tilde{x} = \frac{q}{m}E_0e^{-i\omega t}, \quad (2.42)$$

which has a solution

$$\tilde{x}(t) = \frac{q^2/m}{\omega_0^2 - \omega^2 - i\gamma\omega}E_0e^{-i\omega t}. \quad (2.43)$$

The induced dipole moment (due to the electron shift) is the real part of  $\tilde{p}(t) = q\tilde{x}(t)$ . The polarization is given by  $\tilde{\mathbf{P}} = N\tilde{\mathbf{p}}$  for the volume density of electrons  $N$ . Then, from (2.43),  $\tilde{\mathbf{P}} = \varepsilon_0\chi\tilde{\mathbf{E}}$  and  $\varepsilon = 1 + \chi$  it follows that

$$\varepsilon_{\text{Lorentz}}(\omega) = 1 + \frac{\omega_p^2}{\omega_0^2 - \omega^2 - i\gamma\omega}, \quad (2.44)$$

where  $\omega_p = \sqrt{\frac{Ne^2}{m\varepsilon_0}}$  is called the plasma frequency;

with real and imaginary parts

$$\varepsilon_1(\omega) = 1 + \frac{\omega_p^2(\omega_0^2 - \omega^2)}{(\omega_0^2 - \omega^2)^2 + \gamma^2\omega^2}, \quad (2.45)$$

$$\varepsilon_2(\omega) = \frac{\omega_p^2\gamma\omega}{(\omega_0^2 - \omega^2)^2 + \gamma^2\omega^2}. \quad (2.46)$$

The resulting model (2.44) is a classical Lorentz oscillator model of optical properties in which bound electrons of matter are treated as simple harmonic oscillators subjected to the driving force of applied electromagnetic fields.

In general, electrons in different states experience different natural frequencies  $\omega_j$  and damping coefficients  $\gamma_j$  (we assume groups of  $f_j$  electrons) and

$$\tilde{\mathbf{P}} = \frac{Ne^2}{m} \left( \sum_j \frac{f_j}{\omega_j^2 - \omega^2 - i\gamma_j\omega} \right) \tilde{\mathbf{E}}, \quad (2.47)$$

which together with  $\tilde{\mathbf{P}} = \varepsilon_0\chi\tilde{\mathbf{E}}$  and  $\varepsilon = 1 + \chi$  gives

$$\varepsilon(\omega) = 1 + \frac{Ne^2}{m\varepsilon_0} \sum_j \frac{f_j}{\omega_j^2 - \omega^2 - i\gamma_j\omega}. \quad (2.48)$$

Notice that the imaginary term plays important role only when  $\omega$  is very close to one of the resonant frequencies  $\omega_j$ .

The quantum mechanical expression for the dielectric function may be written formally identical to classical expression

$$\varepsilon(\omega) = 1 + \frac{Ne^2}{m\varepsilon_0} \sum_j \frac{f_{ij}}{\omega_{ij}^2 - \omega^2 - i\gamma_j\omega}, \quad (2.49)$$

but interpretations of the terms in the quantum and classical expressions are quite different. Quantum mechanically  $\omega_{ij}$  is the energy difference (divided by  $\hbar$ ) between the initial or ground state  $i$  and excited state  $j$ . The oscillator strengths  $f_{ij}$  represent the probability of an excitation from state  $i$  to state  $j$ ; they are calculated through the matrix elements of the dipole moment operator.  $\gamma_j$  relates to the probabilities of transition to all other quantum states.

BK7 glass substrates were used for all the samples in this research and thin films of SiO<sub>2</sub> and TiO<sub>2</sub> were used in multilayer samples. These materials are transparent to the visible light with absorption edge in the UV. Dispersion relations used for their optical characterization (Cauchy dispersion model in visible and Urbach absorption in higher photon energy region) are discussed in the following paragraphs.

Cauchy equation [54] is an empirical relationship between the refractive index and wavelength of light for a transparent material (extinction coefficient  $k = 0$ )

$$n(\lambda) = A + \frac{B}{\lambda^2} + \frac{C}{\lambda^4} + \dots, \quad k = 0, \quad (2.50)$$

where  $n$  is the refractive index,  $\lambda$  is the wavelength,  $A$ ,  $B$ ,  $C$ , etc., are coefficients that can be determined for a material by fitting the equation to measured refractive indices at known wavelengths. Cauchy equation is actually just a series expansion of a single term of Sellmeier dispersion which, further, is a special case of Lorentz model. Sellmeier dispersion will be presented in next paragraph. The Cauchy equation is only valid for regions of normal dispersion in the visible wavelength region. In the infrared, the equation becomes inaccurate, and it cannot represent regions of anomalous dispersion. Despite this, its mathematical simplicity makes it useful and widely applied for transparent materials.

The Sellmeier's equation [55], which is a later development of Cauchy's work, handles anomalously dispersive regions, and more accurately models material's refractive index across the ultraviolet, visible, and infrared spectrum. In Sellmeier dispersion model of transparent media, the material is treated as a collection of atoms whose negative electron clouds are displaced from the positive nucleus by the oscillating electric fields of the light beam (at IR wavelengths, the atoms themselves are displaced by the electric field). The oscillating dipoles resonate at a specific frequency (energy or wavelength), so the dielectric response is modelled as one or more Lorentz oscillators. Sellmeier model assumes that the atomic dipoles have no absorption, so the broadening of the Lorentz oscillators equals zero.

The resulting equations are usually written as:

$$\varepsilon_1(\lambda) = n^2 = 1 + \sum_{k=1}^m \frac{A_k \lambda^2}{\lambda^2 - \lambda_k^2}, \quad \varepsilon_2 = 0. \quad (2.51)$$

Multiple terms are used for multiple resonances. Because there is no broadening term, the equations are purely real ( $\varepsilon_2 = 0, k = 0$ ), and each term approaches  $+\infty$  or  $-\infty$  as  $\lambda$  approaches  $\lambda_k$  from the long or short wavelength sides. Thus, the Sellmeier dispersion model cannot be valid in spectral ranges close to the resonant frequency.

Absorption spectrum associated with a defect-free semiconductor or dielectric terminates abruptly at the absorption edge. In an amorphous semiconductors and dielectrics an absorption tail extends into the gap region. Urbach's rule states that the optical absorption coefficient near the absorption edge is an exponential function of photon energy. The rule was discovered in 1953 by Franz Urbach's study of the optical absorption of silver halides [56]. In the range of absorption coefficients below  $10^3 \text{ cm}^{-1}$  the photon energy dependence of the optical absorption is exponential over three or more orders of magnitude ("Urbach edge") [57]. The Urbach edge in the optical absorption spectrum arises as a result of optical transitions involving the tail states with their density exponentially decaying into the gap. Urbach also pointed out that the slope of the absorption edge depends on temperature, impurities and structural disorder. Afterwards, many other insulator and amorphous materials, including silica (amorphous  $\text{SiO}_2$ ), were found to obey Urbach's rule. The Urbach equation gives a convenient representation of the extinction coefficient when the material is only slightly absorbing at the UV-end of the spectral range of interest.

The Urbach equation is

$$\alpha(E) = \alpha_0 \exp\left(\frac{E}{E_\mu}\right), \quad (2.52)$$

where  $E_\mu$  is the Urbach energy which is associated to structural and thermal disorder in the material [56].

## 2.2.4. Optical properties of metals

Optical properties of metals are determined by contributions from free electron absorption and from interband absorption. As a result, the dispersion of the optical constants of metals tends to be rather complicated. They don't exhibit vanishing optical absorption anywhere in the UV-VIS-NIR regions of the spectrum.

The Drude model for metals is a classical kinetic model of conductivity (1/resistivity) developed by Drude and Sommerfeld [58, 59]. It describes the interaction of time varying electric fields with charge carriers which move freely in conductive materials. The basic picture of metals in the framework of this theory is gas of free and independent electrons. The electrons move freely between collisions (with lattice ions, other electrons, defects, phonons, etc.), which occur with an average rate of  $\gamma = \tau^{-1}$ , where  $\tau$  is called electron relaxation time. There is a complete loss of directional information after a collision and the result is a random orientation of the electron velocity afterwards. In an external field, the electrons are accelerated between collisions resulting in a drift motion – electric current. The resulting alternating current conductivity  $\sigma(\omega)$  of metals in Drude model is

$$\sigma(\omega) = \frac{\sigma_{static}}{1 - i\omega\tau}, \quad (2.53)$$

where  $\sigma_{static}$  is the static value for the conductivity.

Recalling relation between conductivity and dielectric function (2.25), the Drude dielectric function, is obtained

$$\epsilon_{Drude}(\omega) = 1 - \frac{\omega_p^2}{\omega^2 + i\gamma\omega}, \quad (2.54)$$

with real and imaginary parts

$$\epsilon_1(\omega) = 1 - \frac{\omega_p^2}{\omega^2 + \gamma^2}, \quad (2.55)$$

$$\epsilon_2(\omega) = \frac{\omega_p^2\gamma}{\omega(\omega^2 + \gamma^2)}, \quad (2.56)$$

which may be used to describe the interaction between light and free electrons in metals.

Notice that the Drude dielectric function is represented by a Lorentz oscillator having zero centre energy.  $\omega_p = \sqrt{Ne^2/\epsilon_0 m_e}$  is plasma frequency,  $N$  is volume density of electrons,  $e$  is electron charge,  $m_e$  is electron mass and  $\gamma$  is the electron relaxation rate.

The coupling of free electrons to the ion core can be described by introducing effective electron mass  $m^*$ , which is in general different from the free-electron mass  $m_e$ . It is a simple way to incorporate into model the influence of specific band-structure of metal on the behaviour of conduction electrons.

The contribution of the bound electrons to the polarizability may also be included by replacing number 1 in expression (2.54) with  $\epsilon_\infty$  (which is equal to 1 in the case that just the conduction band electrons contribute to the polarization).

Free-electron types of metals to which Drude model applies well are the alkali metals Li, Na, K and Rb, and multivalent metals such as Mg, Al and Pb. For most metals at room temperature,  $\gamma$  is much less than  $\omega_p$ . Plasma frequencies of metals are in the visible and ultraviolet spectral regions. A good approximation to the real and imaginary parts of Drude dielectric function in these spectral regions is

$$\epsilon_1 \approx 1 - \frac{\omega_p^2}{\omega^2}, \quad \epsilon_2 \approx \frac{\omega_p^2 \gamma}{\omega^3}, \quad (\omega \gg \gamma). \quad (2.57)$$

The high frequency limit of the Lorentz model (2.44) gives the same equations indicating that at sufficiently high frequencies all non-conductors have metal like dispersion. Thus, the Drude free-electron model is not limited to metals.

In this thesis, the focus is on the noble metals. According to the definition of a noble metal in physics, noble metals should have the d-bands of the electronic structure filled and below Fermi level [60, 61]. Copper, silver and gold fulfil this condition. The excitation of bound electrons from filled d-bands that are closely below Fermi energy, into the conduction band (interband excitations) in noble metals presents bound-electrons contribution to the dielectric function:

$$\epsilon(\omega) = 1 - \frac{\omega_{p,free\,el}^2}{\omega^2 + i\gamma_{free\,el}\omega} + \sum_j \frac{\omega_{pj}^2}{\omega_j^2 - \omega^2 - i\gamma_j\omega}. \quad (2.58)$$

The dispersion of the optical constants (real and imaginary parts of the dielectric function) of the bulk noble metals (silver, gold and copper) is represented in Figure 2.2.

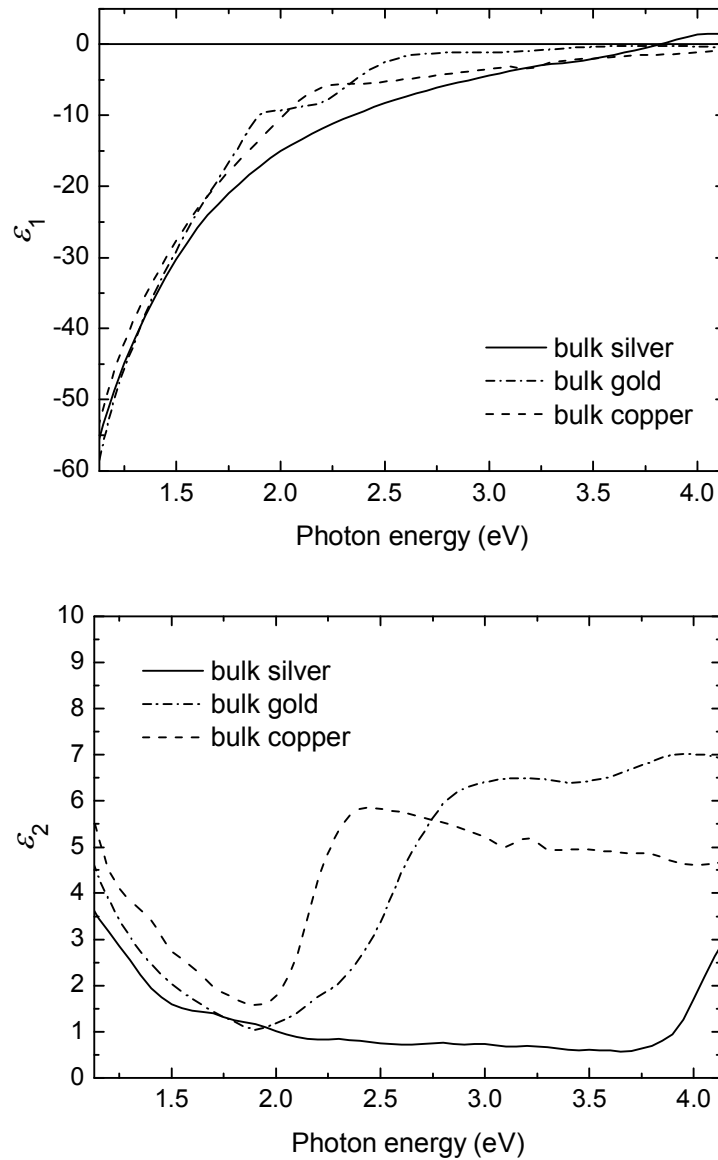


**Figure 2.2** Experimental values of optical constants of the bulk silver, gold and copper taken from [62].

The Drude behaviour of dielectric function may be observed for silver in a broad spectral range. Gold and copper have strong interband absorption in the spectral region above 2.5 eV and 2 eV, respectively, as show in  $\epsilon_2$  part of Figure 2.2.

There are very significant differences between the optical properties of ultrathin layers of noble metals, which are the subject of this thesis, in comparison with optical properties of bulk noble metals (compare Figure 2.2 and Figure 7.3).

## 2.3. Plasmonics

A simple physical model of a metal is free electron gas of density  $N$  immersed in a uniform background of equal and opposite positive charges known as a plasma. Oscillations of a free electron gas (charge density oscillations) are known as plasma oscillations. As in the case of a simple harmonic oscillator, the energy of plasma oscillations can be quantized into units of  $\hbar \omega_p$ . The quantized entities are known as plasmons. As they are charge oscillations and oscillating charges produce electromagnetic fields, plasmons are inherently associated with an electromagnetic field. A theoretical description has to include this interplay of charges and fields. The boundary conditions for electromagnetic fields lead to different conditions for the occurrence of plasmons in the cases of bulk material, planar metal-dielectric interfaces and metal particles. Therefore we distinguish three different kinds of plasmons: volume plasmons (in bulk metal), surface plasmons (at the planar metal-dielectric interface) and particle plasmons (e.g., in metallic nanoparticles). Plasmonics investigates the wealth of phenomena related to plasmons and associated electromagnetic fields. Although particle plasmons play a central role in this thesis, an introduction to all of three fundamental plasmonic excitations is given in the following sections (valuable sources were: [63] for plasmonics in general, [30, 64] for interaction of light with small particles; a systematic rigorous approach to surface states is given in [65]).

### 2.3.1. Volume plasmons (bulk plasmons)

The fundamental excitations of the conduction electron sea in bulk metals are volume plasmons. The long wavelength  $\varepsilon(\omega, K = 0)$  response of free electron gas may be obtained from the Drude dielectric function (2.54) in case of negligible damping  $\gamma$  (the same result can be derived by solving equation of motion of a free electron of mass  $m$  and charge  $e$  in an electric field  $\mathbf{E}$ ). The dielectric function for free electron gas of density  $N$  immersed in a uniform background of positive charges (known as a plasma) is given by

$$\varepsilon(\omega) = 1 - \frac{\omega_p^2}{\omega^2}, \quad (2.59)$$

where the plasma frequency  $\omega_p$  is defined by the relation

$$\omega_p^2 = \frac{Ne^2}{\varepsilon_0 m}. \quad (2.60)$$



When  $\varepsilon(\omega) = 0$  (which is the case if  $\omega = \omega_p$ ), it is not necessary to apply an external field to the free electron gas in order to produce an internal electric field. The electrons can be excited to oscillate at  $\omega_p$  with the Coulomb attraction between the electrons and the positive background providing the restoring forces. Such oscillations of a free electron gas are known as plasma oscillations. The plasma frequency  $\omega_p$  is the natural frequency of plasma oscillations. It is assumed that all electrons move in phase, thus  $\omega_p$  corresponds to the oscillation frequency in the long-wavelength limit (where  $\mathbf{k} = 0$ ). The quanta of these charge oscillations are called plasmons (or volume plasmons, to distinguish them from surface and particle plasmons, which will be discussed further in the text). In general, plasmons cannot be excited in optical absorption since they are longitudinal excitations (i.e., the electrons vibrate along the direction of propagation) while photons are transverse (the electric field is perpendicular to the direction of propagation). Because volume plasmons do not couple to transverse electromagnetic waves, they can only be excited by particle impact.

Experimentally, the plasma frequency of metals is typically determined by electron loss spectroscopy experiments, where electrons are passed through thin metallic foils. For most metals, the plasma frequency is in the ultraviolet regime:  $\omega_p$  is on the order of 5 eV – 15 eV, depending on details of the band structure [53].

Using (2.28), the propagation of transverse electromagnetic waves in electron plasma can be investigated. The dispersion relation for travelling waves is obtained using (2.59) in (2.28):

$$\omega^2 = \omega_p^2 + K^2 c^2. \quad (2.61)$$

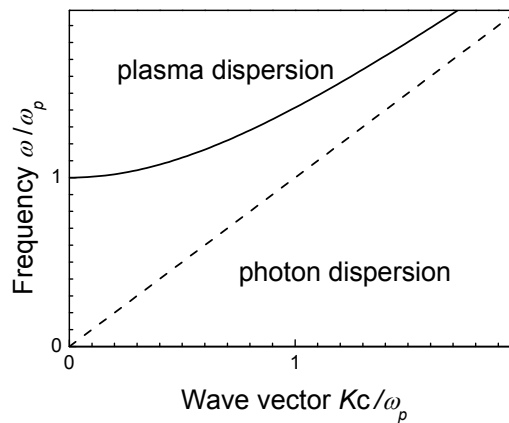


**Figure 2.3** The dispersion relation of the free electron gas.

For  $\omega < \omega_p$  the propagation of transverse electromagnetic field is not possible, but for  $\omega > \omega_p$  the plasma supports propagation of transverse waves and this is known as ultraviolet transparency of metals (as mentioned,  $\omega_p$  of metals is in UV).

### 2.3.2. Surface plasmon polaritons (surface plasmons)

Surface plasmon polaritons (SPP) are essentially two-dimensional electromagnetic waves propagating at the flat interface between a conductor and a dielectric, evanescently confined in the perpendicular direction (i.e., decaying on both sides of the interface). These electromagnetic surface waves arise via the coupling of the electromagnetic fields to oscillations of the conductor's electron plasma (charge density oscillations).

The most simple geometry sustaining SPPs is that of a single, flat interface between a dielectric, non-absorbing half space ( $z > 0$ ) with positive real dielectric constant  $\epsilon_b$ , and an adjacent conducting (metal), half space ( $z < 0$ ) described via a dielectric function  $\epsilon_a(\omega)$  (a metal here implies that  $\text{Re}[\epsilon_a] < 0$ . For metals this condition is fulfilled at frequencies below the bulk plasmon frequency  $\omega_p$ .) Propagating wave solutions confined to the interface, with evanescent decay in the perpendicular direction can be obtained from wave equation and appropriate boundary conditions. Without going into details of derivations, several important physical results will be mentioned. The confinement to the surface demands that  $\text{Re}[\epsilon_a] < 0$  if  $\epsilon_b > 0$ , so the surface waves exist only at interfaces between materials with opposite signs of the real part of their dielectric permittivities, i.e. between a conductor and an insulator. The dispersion relation of SPPs propagating at the interface between the two half spaces is

$$K_x = \frac{\omega}{c} \sqrt{\frac{\epsilon_a \epsilon_b}{\epsilon_a + \epsilon_b}}, \quad (2.62)$$

where  $K_x$  is a wave vector in the plane of propagation. The SPP dispersion curve lies to the right of the light line of the dielectric (given by  $\omega = cK_x / \sqrt{\epsilon_b}$ ), and excitation by light beams is not possible unless special techniques for phase-matching are employed.

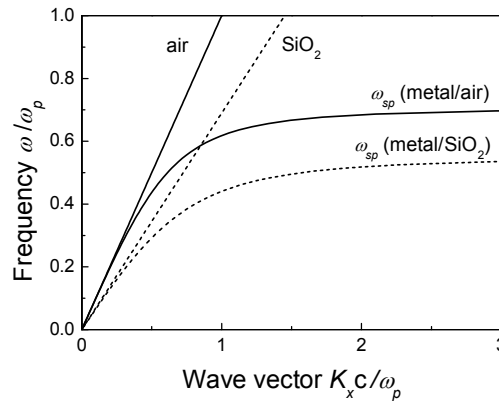


**Figure 2.4** Dispersion relation of SPPs at the interface between a metal with negligible collision frequency and air (solid curves) and silica (dashed curves).

In the range of large wave vectors, the frequency of the SPPs approaches the characteristic surface plasmon frequency

$$\omega_{sp} = \frac{\omega_p}{\sqrt{1 + \epsilon_b}}. \quad (2.63)$$

In the limit of negligible damping of the conduction electron oscillation ( $\text{Im}[\epsilon_a(\omega)] = 0$ ), the wave vector  $K_x$  goes to infinity as the frequency approaches  $\omega_{sp}$ , and the group velocity  $v_g \rightarrow 0$ . The mode thus acquires electrostatic character. The strict definition of the surface plasmon is that it is a large wave vector limit mode of the surface elementary excitations in metals [65].

### 2.3.3. Localized surface plasmons (particle plasmons)

The third fundamental excitation in plasmonics is localized surface plasmon (LSP). As described in previous section, SPPs are propagating, dispersive electromagnetic waves coupled to the electron plasma of a conductor at a dielectric interface. Localized surface plasmons on the other hand are non-propagating excitations of the conduction electrons of metallic nanostructures coupled to the electromagnetic field. These modes arise naturally from the scattering problem of a small, sub-wavelength conductive nanoparticle in an oscillating electromagnetic field. This resonance is called the localized surface plasmon resonance, or shorter, particle plasmon resonance. Important consequence of particle sample geometry is that localized plasmon resonances can be excited by direct light illumination, in contrast to propagating SPPs, where the phase-matching techniques have to be employed.

For silver, gold and copper nanoparticles, the LSP resonance falls into the visible region of the electromagnetic spectrum. A striking consequence of this is that particles produce bright colours of transmitted and reflected light, due to resonantly enhanced absorption and scattering. This effect has found applications for many hundreds of years, for example in the staining of glass for windows or ornamental cups.

The interaction of small metal particles with electromagnetic fields may be well described in a classical framework based on Maxwell's equations. Even metallic nanostructures, down to sizes of a few nanometres, can be described without a need for quantum mechanics (because of high density of free carriers, there is a minute spacing of the electron energy levels compared to thermal excitations of energy  $k_B T$  at room temperature).

In order to understand the diverse optical behaviour of noble metal island films from a qualitative point of view, we shall first consider the localized surface plasmon resonance condition for a single small spherical metal particle with dielectric constant  $\epsilon_m$  embedded in a dielectric host with dielectric constant  $\epsilon_h$ . This condition may be derived using quasi-static approximation which presumes that wavelength of interacting light is much larger than particle size so electric field inside the particle is uniform and induces dipole oscillation.

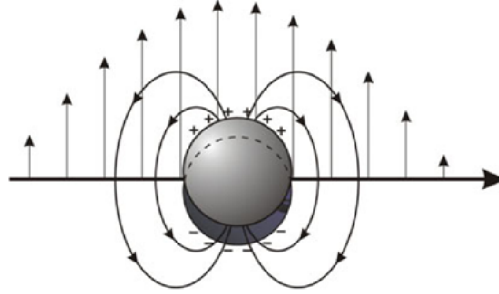


**Figure 2.5** Simplified scheme of the interaction of a small metal particle with light (a particle should be much smaller than the light wavelength).

The static polarizability of the sphere is

$$\alpha = 4\pi r^3 \frac{\epsilon_m - \epsilon_h}{\epsilon_m + 2\epsilon_h}, \quad (2.64)$$

and the polarizabilities of a ellipsoid with semi axes  $a$ ,  $b$  and  $c$ , with corresponding geometrical factors  $L_i$ , for applied fields parallel to corresponding axes  $i$ , are

$$\alpha_i = \frac{4}{3} \pi abc \frac{\epsilon_m - \epsilon_h}{\epsilon_h + L_i(\epsilon_m - \epsilon_h)}. \quad (2.65)$$

If particles are placed in a beam of electromagnetic radiation, the presence of particles results in the extinction of the incident beam. If the surrounding medium in which particles are embedded is non-absorbant, the incident beam is partly absorbed in particles and partly scattered by particles. The extinction cross section  $C_{ext} = C_{abs} + C_{sca}$  is the sum of cross sections for absorption and scattering of light by small particles which are related to particle polarizability as [30]:

$$C_{abs} = \frac{2\pi}{\lambda} \text{Im}[\alpha], \quad (2.66)$$

$$C_{sca} = \frac{1}{6\pi} \left( \frac{2\pi}{\lambda} \right)^4 |\alpha|^2. \quad (2.67)$$

For a metal sphere of volume  $V$  and dielectric function  $\epsilon_m = \epsilon_{1m} + i\epsilon_{2m}$  in the quasi-static limit, the expression for the extinction cross section  $C_{ext} = C_{abs} + C_{sca}$  is

$$C_{ext} \approx 9 \frac{\omega}{c} \epsilon_h^{3/2} V \frac{\epsilon_{2m}}{[\epsilon_{1m} + 2\epsilon_h]^2 + [\epsilon_{2m}]^2}, \quad (2.68)$$

since for small particles of radius  $a$ , much smaller than wavelength of light, the efficiency of absorption, scaling with  $a^3$ , dominates over the scattering efficiency, which scales with  $a^6$  [11]. In practical sense, the scattering may be neglected for particles smaller than 40 nm.

The extinction cross section (2.68) shows a resonant behaviour if the following condition is met:

$$|\epsilon_{1m} + 2\epsilon_h| \rightarrow 0. \quad (2.69)$$

This is the condition of the localized surface plasmon resonance of small metallic particles embedded in a dielectric medium (within quasi-static approximation). The resonance condition (2.69) may be satisfied for metallic particles in dielectric medium because there is a spectral region where the real part of the dielectric function of a metal is negative ( $\epsilon_{1m} < 0$ ) and a dielectric medium has  $\epsilon_h > 0$ . In the special cases of small  $\epsilon_{2m}(\omega)$  ( $\epsilon_{2m} \ll 1$ ), the resonance frequency can be derived from

$$\epsilon_{1m} = -2\epsilon_h. \quad (2.70)$$

Using (2.59) for free electron metals and  $\epsilon_h = 1$ , resonance frequency is obtained:

$$\omega_{LSP} = \frac{\omega_p}{\sqrt{3}}. \quad (2.71)$$

As a result of specific boundary conditions for fields at particle surface, plasma resonance frequency of particle is shape dependent. It may be also seen in the shape dependence of polarizability through depolarization factor  $L$  in (2.65). Hence, more than one resonance may appear for certain particle shapes depending on polarization state of incident light. Plasma resonance positions for various sample geometries in vacuum are listed in Table 2.2 (taken from [30]). Detailed study of curvature dependence of plasmon frequencies is given in [66].

**Table 2.2** Plasma resonance conditions and corresponding resonance frequencies for various sample geometries in vacuum.

Geometry	Resonance condition	Resonance frequency
Bulk metal	$\epsilon_{1m}(\omega) = 0$	$\omega_{res} = \omega_p$
Planar surface	$\epsilon_{1m}(\omega) = -1$	$\omega_{res} = \frac{\omega_p}{\sqrt{2}}$
Thin film	$\frac{\epsilon_{1m}(\omega) + 1}{\epsilon_{1m}(\omega) - 1} = \exp(-K_x d)$	$\omega_{res} = \frac{\omega_p}{\sqrt{2}} \sqrt{1 \pm \exp(-K_x d)}$
Sphere	$\epsilon_{1m}(\omega) = -2$	$\omega_{res} = \frac{\omega_p}{\sqrt{3}}$
Ellipsoid	$\epsilon_{1m}(\omega) = -\frac{1 - L_i}{L_i}$	$\omega_{res,i} = \omega_p L_i$

$L_i$  denote shape dependent depolarization factors,  $d$  is the film thickness and  $x$  gives direction parallel to the film

The quantity  $|\epsilon_{1m} + 2\epsilon_h|$  is presented in Figure 2.6 to illustrate qualitatively the differences observed for the LSP characteristics of noble metal island films, considering  $\text{SiO}_2$  as the dielectric host ( $\epsilon_h = 2.3$ ).

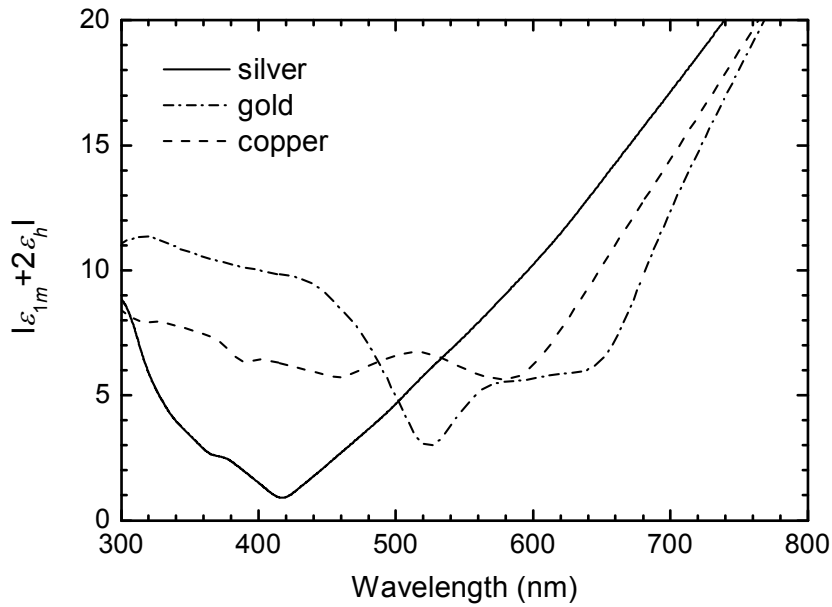


**Figure 2.6** Resonance condition for localized surface plasmon resonance of small, spherical, noble metal particles embedded in a dielectric medium. Bulk metal dielectric functions shown in Figure 2.2 were used for  $\epsilon_m$  and  $\text{SiO}_2$  environment with  $\epsilon_h = 2.3$  was assumed.

First, the wavelength of the minimum of  $|\epsilon_m + 2\epsilon_h|$  is close to the wavelength value where the minimum in transmittance spectra of metal island films occurs (see Figure 4.2 for comparison). For silver, the resonance condition is best accomplished because the imaginary part of the dielectric function of silver is close to zero in the visible part of spectrum. This is not the case for gold and copper, where there is a contribution to the imaginary part of the dielectric function at short wavelengths due to electronic interband transitions. As result, the minimum of  $|\epsilon_{1m} + 2\epsilon_h|$  is broader than in the case of silver and not as deep. Consequently, the LSP resonance is broader and less deep for copper and gold than for silver.

## 2.4. Plasmons in noble metal island films

Real MIFs consist of nanoparticles of different sizes and shapes randomly distributed on the substrate on which they form a kind of thin film. Approach to investigate optical properties of such complex systems from the first principles may show as intractable. Therefore, in order to describe and understand the diverse optical behaviour of noble metal island films, effective medium theories and oscillator models are applied in the analysis. The main assumption that justifies suggested approaches is that the wavelength of light is significantly larger than characteristic dimensions of nanoparticles in MIFs. Then, complex structure of supported nanoparticles which form MIFs may be modelled with a homogeneous layer with effective dielectric function and layer thickness [43].



**Figure 2.7** MIF is modelled with a homogeneous layer with effective dielectric function and layer thickness.

Optical constants are usually determined by fitting of experimental data to some parametric dispersion model. Unlike many materials for which standard dispersion model exist, MIFs are usually modelled by effective medium theories, which only roughly describe their optical behaviour [45].

In this thesis, it is shown that the effective optical constants of MIFs were well described using a multiple oscillator approach that can take into account different light-matter interaction phenomena which occur in the investigated spectral range. Effective optical constants of MIFs offer insight to different physical phenomena connected to MIFs, such as plasmon resonance, size effects in nanostructured matter, percolation etc.

### 2.4.1. Effective medium theories for plasmons in metal island films

In the context of modelling MIF with a homogeneous layer with effective dielectric function, it is tempting to try to describe its optical properties as a mixture of properties of metal nanoparticles and of surrounding media, (either air or embedding dielectric). Therefore, it would be useful to define effective optical constants of the mixture that are related to the optical constants of the composing materials.

When considering material mixtures, it is assumed that the composing materials are in the mixture as phases of microstructure that is big enough to maintain its own dielectric identity, the same as in a layer of a single material, but smaller in comparison to the wavelength of the incident light. In this way the medium is microscopically heterogeneous but macroscopically homogeneous. To satisfy this condition for the visible light and up to mid-infrared radiation, the constituents of the microstructure should have dimensions typically between 3 nm and 30 nm (the shorter the wavelength, the lower the upper limit of the size).

The models developed for description of properties of such effectively homogeneous media are called effective medium theories (EMTs) [67]. They are based on the Clausius-Mossoti equation (2.18) which links relates microscopic and macroscopic material properties and which can be generalised to the case of different phases:

$$\frac{\epsilon_{eff} - \epsilon_h}{\epsilon_{eff} + L\epsilon_h} = \sum_j f_j \frac{\epsilon_j - \epsilon_h}{\epsilon_j + L\epsilon_h}. \quad (2.72)$$

Here  $\epsilon_{eff}$  is complex dielectric function of the effective medium,  $\epsilon_h$  of the host (the matrix of the mixed phases) and  $\epsilon_j$  of the individual phase,  $f_j$  is volume fraction of the individual phase and  $L$  is screening factor that is related to the shape of microstructures that form the mixture. If the microstructure consists of spherical particles  $L = 2$ .



The EMTs that are the most widely used are Lorentz-Lorenz [68, 69] model, Maxwell Garnett model [70] and Bruggeman model [71]. They have the same general form, a special case of (2.72) with two phases ( $a$  and  $b$ ) and  $L = 2$ :

$$\frac{\varepsilon_{eff} - \varepsilon_h}{\varepsilon_{eff} + 2\varepsilon_h} = f_a \frac{\varepsilon_a - \varepsilon_h}{\varepsilon_a + 2\varepsilon_h} + f_b \frac{\varepsilon_b - \varepsilon_h}{\varepsilon_b + 2\varepsilon_h}. \quad (2.73)$$

The particular expressions for calculation of effective optical properties of two materials mixtures using described EMTs, where  $\varepsilon_a$  and  $\varepsilon_b$  are dielectric constants of two components, with  $f_a$  and  $f_b$  being volume fractions of corresponding components, are:

$$\text{Lorentz-Lorenz model} \quad \frac{\varepsilon_{eff} - 1}{\varepsilon_{eff} + 2} = f_a \frac{\varepsilon_a - 1}{\varepsilon_a + 2} + f_b \frac{\varepsilon_b - 1}{\varepsilon_b + 2}, \quad (2.74)$$

$$\text{Maxwell Garnett model} \quad \frac{\varepsilon_{eff} - \varepsilon_a}{\varepsilon_{eff} + 2\varepsilon_a} = (1 - f_a) \frac{\varepsilon_b - \varepsilon_a}{\varepsilon_b + 2\varepsilon_a}, \quad (2.75)$$

$$\text{Bruggeman model} \quad f_a \frac{\varepsilon_a - \varepsilon_{eff}}{\varepsilon_a + 2\varepsilon_{eff}} + f_b \frac{\varepsilon_b - \varepsilon_{eff}}{\varepsilon_b + 2\varepsilon_{eff}} = 0. \quad (2.76)$$

Lorentz-Lorenz model takes an average of molecular polarizability of the components. In this case no phase separation is considered as it is supposed that the mixture is realized at atomic/molecular scale. The host material in (2.73) is vacuum ( $\varepsilon_h = 1$ ) and (2.74) is obtained.

If  $f_a > f_b$ , then the mixing materials may be treated in an unsymmetrical way assuming that the material  $a$  is the host ( $\varepsilon_a = \varepsilon_h$ ) and that the material with dielectric function  $\varepsilon_b$  plays the role of inclusions. In this case expression (2.73) takes the Maxwell Garnett form (2.75).

Bruggeman proposed that neither phase should be given preference, but that the inclusions should be considered as being embedded in the effective medium itself. This is equivalent to choosing  $\varepsilon_h = \varepsilon_{eff}$  in (2.73) and the expression (2.76) is obtained.

The Maxwell Garnett model and Bruggeman model assume that the mixing materials are in separated phases. Maxwell Garnett model considers the mixture that has two (or more) separated grain structures where particles of the first material are dispersed in the continuous host of the second material. Thus, Maxwell Garnett model presents a natural choice to describe embedded nanoparticles.

On the other hand, Bruggeman model assumes aggregate structure having a random space filling mixture of two (or more) material phases. Thus, Bruggeman model can describe percolation. In the limit of small volume fractions  $f$ , the predictions of the two theories approach each other. It is shown that in the case of higher filling factors, i.e. when volume fraction of one material is comparable to the volume fraction of another, the Bruggeman model is valid up to the smaller particle radius than Maxwell Garnett model.

Evolution of optical properties of MIFs may be understood on basis of Maxwell Garnett model [72] with the effective dielectric constant of a composite material: the dielectric host of dielectric function  $\epsilon_h$  with spherical metal inclusions of dielectric function  $\epsilon_m$ , having a fill factor  $f$ . The phenomena of LSP resonance naturally arises in this model, which can be seen in Figure 2.8 and Figure 2.9.

In order to take into account the influence of particle size on the LSP resonance broadening, the most common approach is to consider that confinement effect appear as a result of the reduction of the mean free path of electrons, leading to an increase of the damping constant in the Drude model and, thus, of the LSP resonance width:

$$\Gamma_{FWHM}(R) = \gamma(R) = \gamma_{bulk} + A \frac{v_F}{R}, \quad (2.77)$$

where  $\gamma_{bulk}$  is the damping term for the bulk metal,  $R$  is the radius of metal inclusions,  $v_F$  is Fermi velocity for the metal and  $A$  is a constant related to the electron scattering process, typically  $A = 1$  is used in literature [73].

The results of a simulation for the case of silver nanoparticles embedded in the SiO<sub>2</sub> dielectric medium within just described model are shown in Figure 2.8 and in Figure 2.9. In Figure 2.8, an evolution of absorption coefficient  $\alpha_{ext}$  with increase of fill factor  $f$  is given. The value of the damping constant in the Drude expression for the dielectric constant of silver was fixed to the damping constant of bulk silver  $\gamma(R) = \gamma_{bulk\ silver}$ . Figure 2.9 shows evolution of  $\alpha_{ext}$  with change of radius  $R$  of spherical silver inclusions, with fill factor value fixed to  $f = 0.05$ .

The main results of the simulation using Maxwell Garnett model with MIF-SiO<sub>2</sub> layer as a composite film are red shift, broadening and intensity increase of LSP resonance with deposited mass thickness.

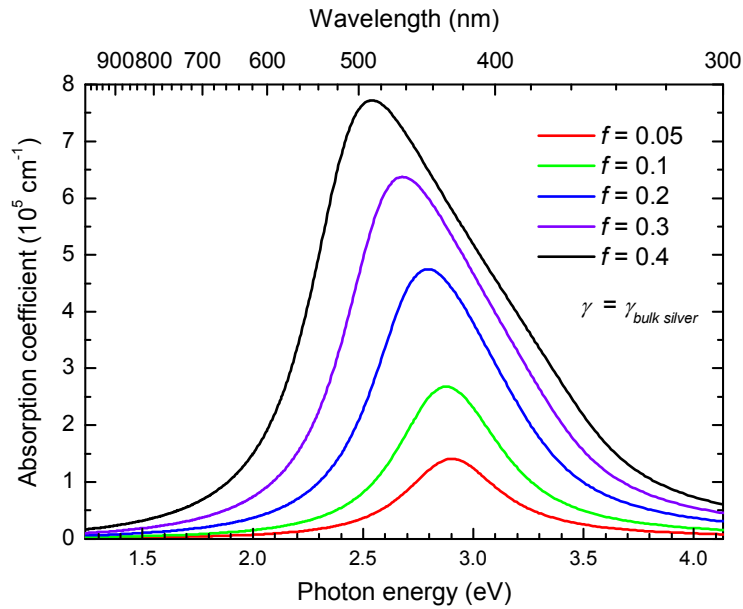


**Figure 2.8** Evolution of absorption coefficient  $\alpha_{ext}$  with increase of fill factor  $f$  is given for MIF-SiO<sub>2</sub> layer as a composite film with optical constants from Maxwell Garnett model (with  $\gamma(R) = \gamma_{bulk\ silver}$ ).

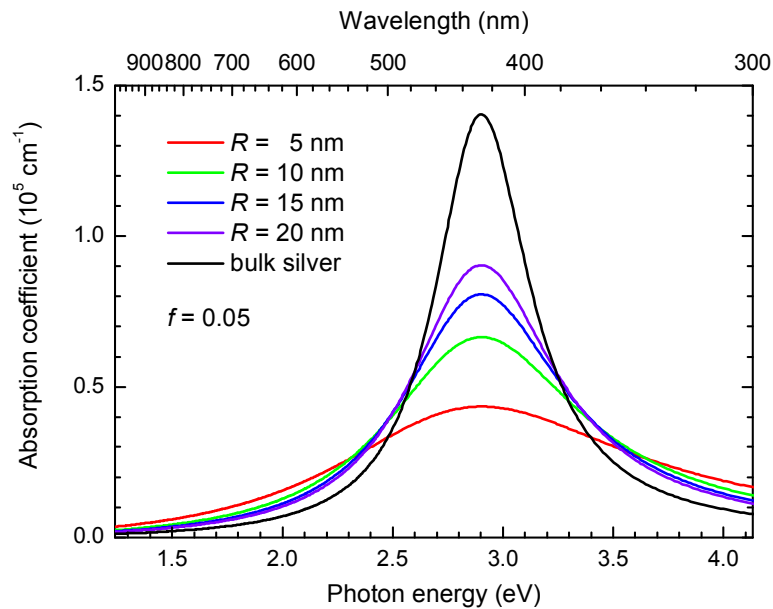


**Figure 2.9** Evolution of absorption coefficient  $\alpha_{ext}$  with change of radius of silver inclusions  $R$  is shown for MIF-SiO<sub>2</sub> layer as a composite film with optical constants from Maxwell Garnett model (the value of fill factor was fixed to  $f = 0.05$ ).

## 2.4.2. Oscillator model for plasmons in noble metal island films

To build a physical dispersion model for the effective optical constants of MIFs, analysis is needed of different phenomena which determine optical properties of MIFs. The main phenomenon is the LSP resonance. Resonant behaviour of physical systems is naturally described by an oscillator model. Absorption due to interband transitions (in visible for gold and copper, and in UV for silver) may also be modelled with oscillators (see sections 2.2.3 and 2.2.4). Behaviour of bulk metals in near infrared is well described with Drude oscillator model and it may be expected to appropriately describe behaviour of MIFs in case of percolation of islands [74]. As a result of the discussion above, the proposed form of complex effective dielectric function  $\varepsilon_{eff}$  as a function of photon energy  $E$  (where  $E = \hbar\omega$ ) may be:

$$\varepsilon_{eff}(E) = \sum_{n=1}^{N_{osc}} \varepsilon_n(E) + \varepsilon_{\infty}, \quad (2.78)$$

where  $\sum_{n=1}^{N_{osc}} \varepsilon_n(E)$  represents the sum of  $N_{osc}$  oscillators  $\varepsilon_n(E)$ , and  $\varepsilon_{\infty}$  is a contribution to the dielectric function from resonances at higher frequencies which are not accessible to our measurements.

According to their physical origin, multiple oscillator contributions to the  $\varepsilon_{eff}(E)$  can be expressed as:

$$\varepsilon_{eff}(E) = \varepsilon_{LSPR}(E) + \varepsilon_{interband}(E) + \varepsilon_{Drude}(E) + \varepsilon_{\infty} \quad (2.79)$$

In the analysis of optical properties of the samples in this research, three different kinds of oscillators  $\varepsilon_n(E)$  were used in various combinations in  $\sum_{n=1}^{N_{osc}} \varepsilon_n(E)$  term of (2.78):

1) *Lorentz oscillator*

$$\varepsilon_{n \text{ Lorentz}}(E) = \frac{A_n B_n E_n}{E_n^2 - E^2 - i B_n E}, \quad (2.80)$$

2) *Gaussian oscillator*

$$\varepsilon_{n \text{ Gaussian}}(E) = \varepsilon_{n1}(E) + i \varepsilon_{n2}(E), \quad (2.81)$$

$$\varepsilon_{n2}(E) = A_n e^{-\left(\frac{2\sqrt{\ln 2}(E-E_n)}{B_n}\right)^2} - A_n e^{-\left(\frac{2\sqrt{\ln 2}(E+E_n)}{B_n}\right)^2}, \quad \varepsilon_{n1}(E) = \frac{2}{\pi} P \int_0^{\infty} \frac{\xi \varepsilon_{n2}(\xi)}{\xi^2 - E^2} d\xi,$$

### 3) Drude oscillator

$$\varepsilon_{nDrude} = -\frac{A_n B_n}{E^2 + iB_n E}. \quad (2.82)$$

Oscillator parameter  $E_n$  is  $n^{\text{th}}$  oscillator centre energy,  $A_n$  is oscillator amplitude and  $B_n$  is a broadening parameter.

The LSP resonance contribution  $\varepsilon_{LSPR}(E)$  was modelled with one or two Lorentz oscillators  $\varepsilon_{nLorentz}(E)$  or Gaussian oscillators  $\varepsilon_{nGaussian}(E)$ . Contribution from interband transitions  $\varepsilon_{interband}(E)$  was modelled using two oscillators for gold or one for silver [75], either  $\varepsilon_{nLorentz}(E)$  or  $\varepsilon_{nGaussian}(E)$ . Contribution  $\varepsilon_{Drude}$  attributed to possible percolation effect, present only for samples with infrared absorption shoulder, was modelled either with  $\varepsilon_{nDrude}(E)$  or with  $\varepsilon_{nGaussian}(E)$ .

Although Lorentz oscillators arising from theoretical considerations elaborated in the sections above are most commonly used in the analysis of MIFs (e.g. [74, 76]), it is shown in this research that Gaussian oscillators are a better choice (detailed analysis is presented in section 7.1). While Lorentz oscillators may be appropriate in describing optical response of the collections of particles of the same size, Gaussian oscillator is more successfully applied when there is a distribution of particle sizes and shapes. This is actually the case with noble metal island films. One Gaussian replaces many Lorentz oscillators belonging to different particles in an ensemble [77].

The oscillator model for optical properties of noble metal island films was used for analysis of the optical properties of the samples investigated by variable angle spectroscopic ellipsometry measurements in this research.

## 2.5. Spectroscopic ellipsometry

Ellipsometry is a very sensitive measurement technique that uses polarized light to characterize thin films, surfaces, and material microstructure. Further elaboration of ellipsometry relies on several valuable sources which are excellent handbooks of ellipsometry [78-82].

Ellipsometry measures the change in polarization state of light reflected from (or transmitted through) the surface of a sample. Fundamentally, ellipsometry refers only to the measurement of the polarization state of a light. However, ellipsometric measurements are usually performed in order to describe an “optical system” that modifies the polarization state of a beam of light. For thin film sample analysis, the “optical system” is, simply, the sample.

When plane electromagnetic wave incidences to a structure composed of one or several thin layers of different media on a substrate, then transmission, reflection, refraction and absorption phenomena take place. In general, the fields  $\mathbf{E}$ ,  $\mathbf{B}$ ,  $\mathbf{D}$ , and  $\mathbf{H}$  will be discontinuous at a boundary between two different media. In the case of linear media, if there is no free charge or free current at the interface, the boundary conditions can be derived from Maxwell’s equations (2.3)-(2.6):

$$\begin{aligned}
 \text{(i)} \quad \varepsilon_{(1)} E_1^\perp - \varepsilon_{(2)} E_2^\perp &= 0 & \text{(iii)} \quad \mathbf{E}_1^\parallel - \mathbf{E}_2^\parallel &= 0 \\
 \text{(ii)} \quad B_1^\perp - B_2^\perp &= 0 & \text{(iv)} \quad \frac{1}{\mu_1} \mathbf{B}_1^\parallel - \frac{1}{\mu_2} \mathbf{B}_2^\parallel &= 0,
 \end{aligned} \tag{2.83}$$

where indexes 1 and 2 sign the fields just to the left and just to the right of the interface between two media ( $\perp$  and  $\parallel$  sign field components perpendicular and parallel to the interface, respectively),  $\hat{\mathbf{n}}$  is the unit vector normal to the interface. These equations are the basis for the theory of reflection and refraction of light.

The first important relation that can be derived from (2.83) is the Snell’s law

$$\tilde{n}_1 \sin \theta_1 = \tilde{n}_2 \sin \tilde{\theta}_2. \tag{2.84}$$

If the Fresnel coefficients for reflection and transmission are defined as the ratio of reflected to incident and transmitted to incident electric field components:

$$\tilde{r} = \frac{\tilde{E}^{reflected}}{\tilde{E}^{incident}} \quad \text{and} \quad \tilde{t} = \frac{\tilde{E}^{transmitted}}{\tilde{E}^{incident}} \quad (2.85)$$

Fresnel equations can be derived from (2.83)

$$\tilde{r}_p = \frac{\tilde{n}_2 \cos \theta_1 - \tilde{n}_1 \cos \tilde{\theta}_2}{\tilde{n}_2 \cos \theta_1 + \tilde{n}_1 \cos \tilde{\theta}_2}, \quad (2.86)$$

$$\tilde{r}_s = \frac{\tilde{n}_1 \cos \theta_1 - \tilde{n}_2 \cos \tilde{\theta}_2}{\tilde{n}_1 \cos \theta_1 + \tilde{n}_2 \cos \tilde{\theta}_2}. \quad (2.87)$$

The measured values in ellipsometry are psi ( $\Psi$ ) and delta ( $\Delta$ ), values related to the ratio of Fresnel reflection coefficients  $\tilde{r}_p$  and  $\tilde{r}_s$ , for  $p$  and  $s$  polarized light (field components parallel and perpendicular to the plane of incidence, respectively) (Figure 2.10):

$$\rho = \frac{\tilde{r}_p}{\tilde{r}_s} = \tan(\Psi) e^{i\Delta}. \quad (2.88)$$

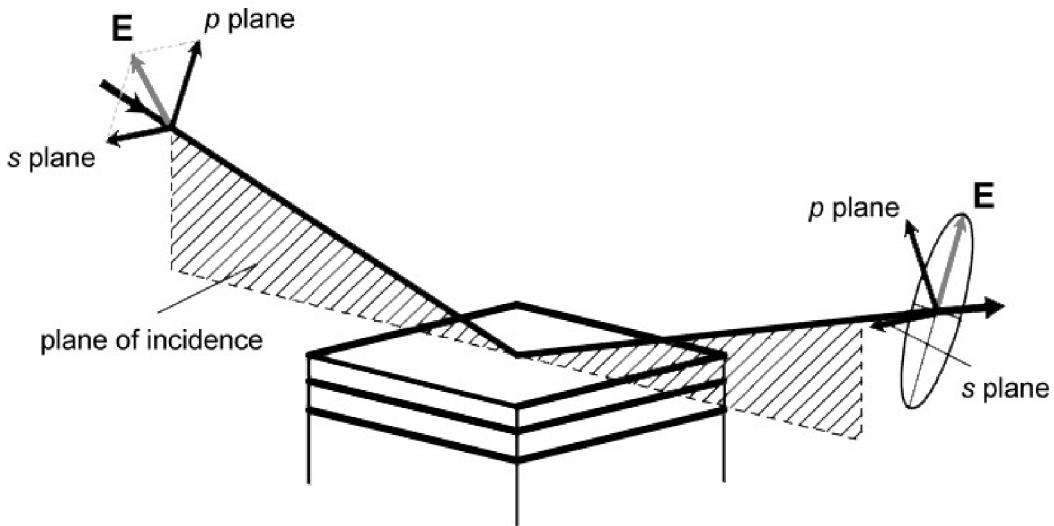


**Figure 2.10** Geometry of an ellipsometric experiment, showing  $p$  and  $s$  directions [83].

$\Psi$  and  $\Delta$  are called ellipsometric angles. They determine the differential changes in amplitude ( $\Psi$ ) and phase ( $\Delta$ ) experienced upon reflection by the component of the electric vector parallel and perpendicular to the plane of incidence.

Ellipsometry measures the ratio of two complex values. Because the ratio is a complex number, it also contains “phase” information ( $\Delta$ ), which makes the measurement very sensitive.

The ellipsometric  $\Psi$  and  $\Delta$  data measured on a bulk sample can be directly inverted into the ‘pseudo-optical’ constants of the material, assuming that surface oxide and/or roughness effects are negligible (this transform is given by (2.89), in which  $\theta$  is the angle of incidence, and  $\rho$  is the complex ellipsometric ratio defined in (2.88)):

$$\langle \tilde{\epsilon} \rangle = \langle \epsilon_1 \rangle + i \langle \epsilon_2 \rangle = \langle \tilde{n} \rangle^2 = (\langle n \rangle + i \langle k \rangle)^2 = \sin^2 \theta \cdot \left[ 1 + \tan^2 \theta \cdot \left( \frac{1 - \rho}{1 + \rho} \right)^2 \right]. \quad (2.89)$$

This approach may be applied for optical characterization of bare substrates in the case where backside reflections are suppressed.

Most of the measurements in this research are done on three layer systems where: medium 1 is ambient (air) – medium 2 is thin film (MIF) with thickness  $d$  – medium 3 is substrate (BK7 glass). Basically, reflection ellipsometry of a three layer system measures the function

$$\rho = \tan \Psi e^{i\Delta} = \frac{r_{12p} + r_{23p} e^{-i2\beta}}{1 + r_{12p} r_{23p} e^{-i2\beta}} \frac{1 + r_{12s} r_{23s} e^{-i2\beta}}{r_{12s} + r_{23s} e^{-i2\beta}}, \quad (2.90)$$

where  $\beta = 2\pi \frac{d}{\lambda} (n_2 \cos \theta_2)$  is the phase thickness of thin film,  $\lambda$  is the wavelength of incident light in medium 1,  $r_{ij}$  is the Fresnel reflection coefficient for the interface between  $i$ -th and  $j$ -th medium and  $\theta_j$  is the angle between the light beam in the  $j$ -th medium and the normal to the interface between media. The final functional form of  $\rho$  is

$$\tan \Psi e^{i\Delta} = \rho (n_1, n_2, n_3, d, \theta_1, \lambda). \quad (2.91)$$

There is only one propagating angle ( $\theta_1$ ) variable dependence of  $\rho$  because  $\theta_1$ ,  $\theta_2$  and  $\theta_3$  are related through the Snell law. In general case,  $\rho$  explicitly depends on nine real variables, the refractive index and extinction coefficient of ambient ( $n_1$ ,  $k_1$ ), film ( $n_2$ ,  $k_2$ ) and substrate ( $n_3$ ,  $k_3$ ), film thickness ( $d$ ), angle of incidence ( $\theta_1$ ), and the wavelength ( $\lambda$ ). By knowing  $n_1$ ,  $n_2$ ,  $n_3$ ,  $d$ ,  $\theta_1$ , the ellipsometric angles can be calculated at any wavelength. In ellipsometry  $\Psi$  and  $\Delta$  can be measured at a given  $\theta_1$  and  $\lambda$ . The ambient optical constants are usually taken to be  $n_1 = 1$  and  $k_1 = 0$ , and the substrate optical constants may be measured independently. The only unknowns left in (2.91) are the complex refractive index of the film and its thickness.



Although the function  $\rho$  may appear from (2.91) to be deceptively simple, it is a non linear equation which has multiple solutions and there is no general unique inversion to obtain  $n_2$  and  $d$ . The usual procedure in ellipsometry to solve the inverse problem is explained in section 3.3 and illustrated in Figure 3.1.

Ellipsometry derives its sensitivity from the determination of the relative phase change in a reflected polarized light beam, exceeding the sensitivity of an intensity reflectance measurement. Also, ellipsometry is more accurate than intensity reflectance because the absolute intensity of the reflected light does not have to be measured, thus no special reference samples need to be maintained.

The combination of variable angle of incidence and spectroscopic measurements allows large amounts of data from a given sample to be acquired. More importantly, the spectral acquisition range and angles of incidence may be optimized for the determination of certain sample parameters such as layer thickness or the optical constants of one of the films. In many cases the dispersion (variation with wavelength) of the optical constants of a given material is known, or the optical constants may be parameterized in such a way as to enforce some type of dispersion on the optical constants (e.g. Cauchy, Lorentz, multiple oscillator model applied for noble MIFs in this thesis, parametric semiconductor models etc.). It is possible to acquire data in spectral regions where the measured data are most sensitive to the model parameters which are to be determined. As a result the variable angle of incidence spectroscopic ellipsometer has possibility to characterize many complex structures, which a single angle and/or a single wavelength ellipsometers cannot.

Ellipsometry is commonly used to characterize both thin films and bulk materials. For many samples, ellipsometry is sensitive to film thickness on a sub-monolayer level. It has also proven to be the primary technique for determining optical constants in the UV, visible, and IR wavelength ranges. Ellipsometry is very flexible and is sensitive to many microstructural material properties. Using modelling that connects microstructure with optical constants, ellipsometry is used to obtain information about:

- Doping concentration
- Surface and interfacial roughness
- Alloy ratio
- Crystallinity
- Optical anisotropy
- Depth profile of material properties, etc.

Ellipsometers consist of the light source, optical system for preparation of light beam and a system for detection of light (Figure 2.11). Polarizers are especially important in the optical systems. They provide control over the state of polarisation of the beams and they are critical for determination of ellipsometric angles. They can be positioned in the beam path before or after the sample. In the later case they are called analysers. Compensators are used for introduction of phase shift between  $s$  and  $p$  beam components.

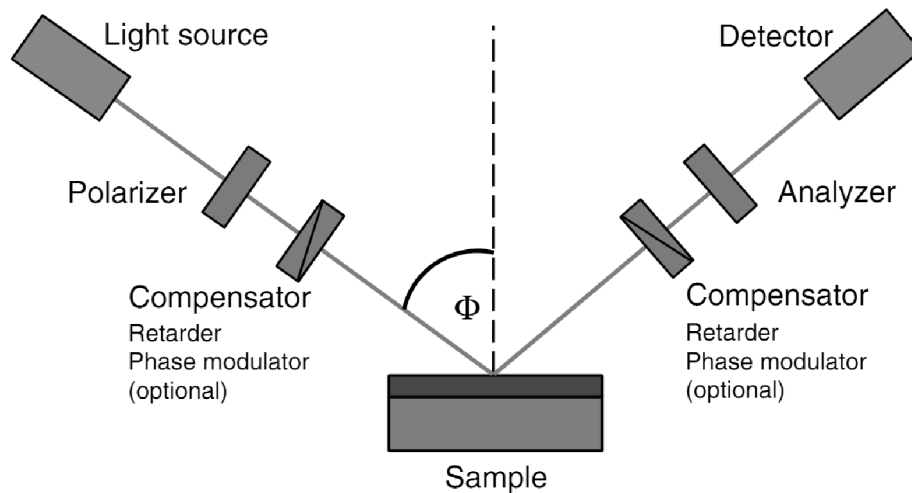


**Figure 2.11** Basic scheme of an ellipsometer components: a white light source used for illuminating the sample (wavelength selection may be done either using monochromator after the light source or using spectrally selective detectors like diode arrays or CCD), a polarizer, a compensator (retarder, photoelastic modulator) which can be placed in the path of the incident or reflected light beam, a second polarizer called analyzer, and the detector. [43].

The most commonly used types of ellipsometers are the following:

a) Null ellipsometer – angles are determined from measured minima of intensity. Before reaching the sample, the beam passes through linear polarizer and compensator and upon reflection at the surface of the sample through analyser. The angles are determined from angular positions of polarizer and analyser at the moment when minimum of intensity is detected. This setup enables very precise measurements and good control over systematic errors. However, since the measurements are very slow, this type of ellipsometer is not often commercially used, especially for spectral measurements.

b) Ellipsometers with rotating elements are based on periodical modulation of polarisation states of beam incident or reflected at the sample by mechanical rotation of some of the optical elements. Ellipsometers with rotating analyser or rotating polarizer can be distinguished. The detected signal intensity is time dependent and upon Fourier analysis it is possible to determine ellipsometric angles. This type of ellipsometer performs measurements much faster compared with null ellipsometers. This setup is very stable and the measurements are very precise. The drawback of this setup is a necessity for a very accurate calibration to avoid systematic errors. The ellipsometer used in this research was rotating analyser ellipsometer with autoretarder (patented compensator).

c) Phase modulation ellipsometers don't need rotating elements. Before reaching the sample, the beam passes photoelastic modulator that vibrates with a defined frequency and introduces phase shift between components of electric field. The detected signal varies periodically and can be decomposed into the continuous signal, the signal that vibrates with frequency of modulator and the one that varies with double frequency of the modulator. Angles are determined from analysis of these signals. Constructing and calibrating an ellipsometer of this type is difficult because polarization modulators tend to exhibit strong sensitivity to ambient temperature. The advantage is that they don't have mobile parts.

One of the main concerns of ellipsometry is systematic errors. The required optics is pretty complex and it is necessary to make very precise calibration of the device to avoid errors in alignment of different optical elements.

Ellipsometric measurements are always done at large angles of incidence and therefore it is difficult to estimate the contribution from multiple reflections from the back side of the substrate. There are several solutions to eliminate contribution from back side reflections: using substrates with sanded back side, using thick substrates ( $\sim 3$  mm or more), substrates with non-parallel surfaces, absorbing substrates or using incidence beam of micrometer diameter (microspot). In these cases, it is possible to treat the sample as being deposited onto semi-infinite substrate. Also, the influence of back-side can be included in the modelling.

## 2.6. Grazing-incidence small-angle X-ray scattering

A detailed morphological characterisation of deposited layers, multilayers and nanostructures like quantum dots or supported islands may be obtained with analysis of grazing-incidence small-angle X-ray scattering (GISAXS) which is based on the phenomenon of total *internal* reflection of X-rays from surfaces in the grazing-incidence range.

In GISAXS experiment a monochromatic beam of X-rays is brought to a sample surface from which X-rays elastically scatter under condition of total *internal* reflection. The optical properties of materials in the photon range above 30 eV can be described by the refractive index that is smaller than 1, compared with vacuum value of 1:

$$n = 1 - \delta + i\beta \quad (\delta, \beta \ll 1), \quad (2.92)$$

where parameters  $\delta$  and  $\beta$  are called the refractive index decrement and the absorption index<sup>2</sup>. For silver  $\delta = 2.94 \times 10^{-5}$ ,  $\beta = 2.66 \times 10^{-6}$ ; for gold  $\delta = 4.71 \times 10^{-5}$ ,  $\beta = 4.85 \times 10^{-6}$  when X-rays wavelength is  $\lambda = 0.154$  nm. Refractive index of materials for X-rays is less than 1 because the driving field frequency is higher than any resonance present in a material (see Figure 2.12).

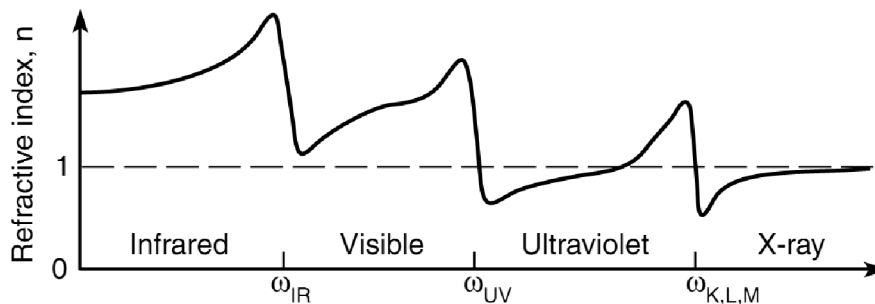


**Figure 2.12** Simplified picture of frequency dependence of refractive index  $n(\omega)$  for materials with typical resonances.

Until the use of high brilliance synchrotron radiation and grazing incidence geometry became possible, the small interaction of hard X-rays with matter prevented its straightforward use for surface or interface studies. Nowadays, surface sensitivity with a reasonable signal to noise ratio is available in synchrotron facilities.

<sup>2</sup> Notice that the absorption index  $\beta$  in X-ray terminology corresponds to extinction coefficient  $k$  in optics.

Typical grazing-incidence experiment geometry is shown in Figure 2.13. A monochromatic beam of X-rays of wave vector  $\mathbf{k}_i$  (wavelength  $\lambda$  between 0.5 Å and 2 Å and corresponding wave number  $K_i = 2\pi/\lambda$ ) incidences on a surface with an incident angle  $\alpha_i$  of a few tenths of a degree with respect to the surface. The light is scattered in the direction  $(2\theta_f, \alpha_f)$  along  $\mathbf{k}_f$  by any type of roughness on the surface.

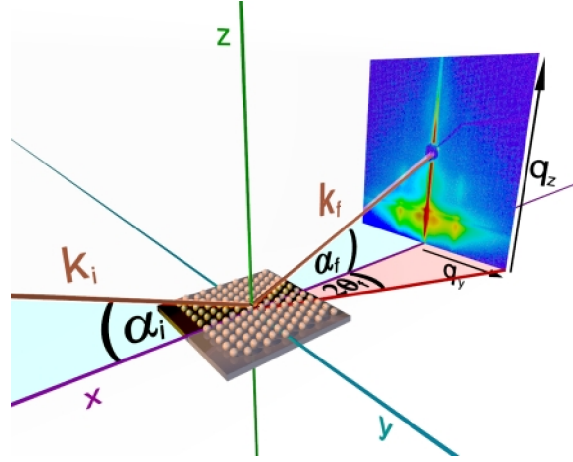


**Figure 2.13** The GISAXS geometry. An incident wave of wave vector  $\mathbf{k}_i$  is scattered in the direction  $\mathbf{k}_f$ .

The scattered X-rays form a scattering pattern which is then detected by a detector which is typically a 2-dimensional flat X-ray detector situated behind the sample, perpendicular to the direction of the primary beam that initially hits the sample. The scattering pattern contains information about the structure of the sample. GISAXS patterns are typically represented as scattered intensity  $I(q)$  as a function of the magnitude of the scattering vector  $\mathbf{q}$ ,  $q = 4\pi \sin(\theta) / \lambda$ . Here  $2\theta$  is the angle between the incident X-ray beam with wave vector  $\mathbf{k}_i$  and the scattered X-ray beam with wave vector  $\mathbf{k}_f$ . The scattering vector or wave vector transfer equals  $\mathbf{q} = \mathbf{k}_f - \mathbf{k}_i$ . Energy conservation holds and the scattering wave vector  $\mathbf{q}$  is given by:

$$\mathbf{q} = \begin{bmatrix} \cos(\alpha_f) \cos(2\theta_f) - \cos(\alpha_i) \cos(2\theta_i) \\ \cos(\alpha_f) \sin(2\theta_f) - \cos(\alpha_i) \sin(2\theta_i) \\ \sin(\alpha_f) + \sin(\alpha_i) \end{bmatrix} \quad (2.93)$$

It is difficult to characterize a single nano-object because of the beam size, divergence, and limitations of X-ray optics (although this field, called coherent X-ray diffraction, is going to develop). The statistical average over the sample can be seen as an advantage since the beam probes a macroscopically large area of the sample and gives information about morphology of a “mean island”.

Compared to microscopy, Grazing Incidence X-Ray Scattering or Diffraction (GIXS or GIXD) and its small angle subset, Grazing Incidence Small-Angle X-Ray Scattering (GISAXS) have several advantages:

1. The technique is fully non-destructive provided that the sample bears hard X-ray exposure;
2. The measurement is averaged over the sample surface, giving statistical information over several square millimetres (while microscopy gives local information about very small sample spot);
3. By varying the probed depth changing the incident angle, X-rays offer the ability to probe from surface to buried interfaces as well as the bulk of the sample;
4. The measurements usually don't require any special sample environment or preparation – the technique can be applied in various types of environment, from ultra-high vacuum to gas atmospheres, even during chemical reactions, in situ and in quasi real-time when kinetic phenomena are involved, like during growth or a catalytic reaction;
5. The Grazing Incidence Small Angle Scattering (GISAXS) technique, which provides morphological information from the nanometer to micrometer length scales, can be combined, for the same samples, with the grazing incidence wide angle X-ray scattering (WAXS) or diffraction (GIXD) techniques which are sensitive to the atomic arrangement and strain state.

The drawbacks of GISAXS are:

1. The use of synchrotron radiation is mandatory because the collected signal scales with the amount of material, which can be rather small (of the order of the monolayer);
2. The interesting information, e.g., the morphology is obtained in reciprocal space, and thus has to be translated in the real space. As only scattered intensities can be measured, the phase information is lost, which means that some model assumptions are most often mandatory to fit the data. This problem can be overcome if the coherence of the synchrotron radiation is employed.

### 2.6.1. Approximate quantitative analysis – Guinier’s approximation

In the analysis of experimental result of GISAXS measurements of metal island films in this research, Guinier’s approach was applied to get a first approximation of horizontal and vertical sizes of nanoparticles. Thus obtained values were used as input parameters to start further, elaborate analysis in the case of gold MIFs samples.

The Guinier’s approximation [84] is a linearization of the small angle scattering data in the region close to the zero scattering angle. Low particle concentration (no interaction) is assumed. The starting point is the classical expression for scattering intensity  $I(q)$  as a function of the magnitude of the scattering vector ( $q$ ):

$$I(q) = 4\pi \int_0^{\infty} P(r) \cdot \frac{\sin(q \cdot r)}{q \cdot r} dr, \quad (2.94)$$

where  $P(r)$  is a probability of finding a vector of length  $r$  between scattering centres within the scattering particle (it can be seen as an inverse Fourier transform of scattering intensity  $I(q)$ ). The derivation of the Guinier’s approximation is presented in the following paragraphs.

The sine function in the expression (2.94) can be approximated by a Taylor series expansion. If the first two terms in the expansion are considered to be significant and if higher order terms ( $q^4, q^6, q^8, \dots$ ) are ignored, the following expression is obtained

$$I(q) \approx 4\pi \int_0^{\infty} P(r) dr \left( 1 - \left( \frac{q^2}{3!} \right) \cdot \frac{\int_0^{\infty} r^2 P(r) dr}{\int_0^{\infty} P(r) dr} \right). \quad (2.95)$$

Now, we can define  $I_0$  and  $R_g$  as follows

$$I_0 = \int_0^{\infty} P(r) dr, \quad R_g^2 = \frac{1}{2} \frac{\int_0^{\infty} r^2 P(r) dr}{\int_0^{\infty} P(r) dr}, \quad (2.96)$$

where  $R_g$  represents Guinier radius or radius of gyration (RMS value of scattering density), and after substitution to (2.95), the result is

$$I(q) \approx I(0) \cdot \left( 1 - \frac{q^2 \cdot R_g^2}{3} \right). \quad (2.97)$$

The equation (2.97) is not a linear equation, but the second factor can be recognized as a part of Taylor series expansion of  $\exp\left[-q^2 R_g^2/3\right]$  and in the approximation of small  $q$  we obtain

$$I(q) = I(0) \cdot e^{-\frac{q^2 \cdot R_g^2}{3}}. \quad (2.98)$$

Finally, we can linearize the equation (2.98) by taking the natural logarithm of both sides thereby producing the recognizable linear form ( $y = a x + b$ )

$$\ln I(q) = \ln I(0) - \frac{R_g^2}{3} \cdot q^2. \quad (2.99)$$

If the shape of the particles is known, their sizes can be determined from the radius of gyration. As an example, for a sphere of radius  $R$  [85]:

$$R_g^2 = \frac{3}{5} R^2. \quad (2.100)$$

## 2.6.2. GISAXS analysis beyond Guinier's approximation

Obtaining more information from GISAXS data requires numerical simulations (also approximate) of scattering. The details of various approximate approaches to the GISAXS analysis beyond Guinier's approximation are described in the Appendix. In the analysis of the samples in this research, several approaches were tried. Successful one was using the scattering calculations in Distorted Wave Born Approximation (DWBA) on gradient layer because it was an appropriate way to treat dense particle systems supported on the substrate [86]. Calculation of the particle-particle correlations was in the framework of Local Monodisperse Approximation (LMA) [86]. As a natural choice for MIFs and suggested by results of AFM and Guinier's approximation, truncated spherical and truncated spheroid particles were chosen as the model particle shapes, with uncoupled size distributions parallel and perpendicular to the surface. The described model gives good results in the analysis of the gold MIFs samples which is presented in section 7.2.2.



## 3. Experimental

### 3.1. Sample preparation

MIFs were prepared by the electron-beam evaporation on 1 mm thick BK7 glass substrates. Prior to deposition, substrates were cleaned with the Balzers substrate cleaning liquid nr. 2, wiped with a cotton cloth and puffed with air. The depositions were done in a modified Varian 3117 evaporator with base pressure of  $5 \times 10^{-6}$  torr. The source materials deposited by evaporation were 99.99 % pure silver, gold and copper. The materials were evaporated from a conical crucible.

The film thickness was controlled by quartz crystal (Sloan Digital DTM). The oscillation frequency of quartz crystal changes as a function of the mass of deposited material. The frequency change is proportional to the deposited mass per unit area. The ratio between deposited mass per unit area and density of deposited material represents “mass thickness” of the deposited layer. Mass thickness of a layer is equal to its real thickness if a material is deposited as homogeneous layer. Silver, gold and copper were deposited in three different mass thicknesses each (3 nm, 7 nm and 12 nm). Deposition rates determined from mass thickness increment with time were  $\sim 0.5$  nm/s for silver and  $\sim 0.1$  nm/s for gold and copper.

The substrates were heated using quartz heaters positioned in the chamber. The depositions were done at different substrate temperatures: 25 °C, 75 °C, 120 °C, 175 °C and 215 °C. In some experiments, a protective capping layer of 10 nm SiO<sub>2</sub> was deposited over MIF in the same deposition run. The role of protective capping layer was to prevent oxidization of silver and copper in air. Sets of samples were prepared without capping layers as well.

The samples with gold MIFs in a sandwich between dielectric layers were also produced by e-beam evaporation; BK7/SiO<sub>2</sub>/Au/TiO<sub>2</sub>, BK7/TiO<sub>2</sub>/Au/TiO<sub>2</sub> and BK7/SiO<sub>2</sub>/Au/SiO<sub>2</sub>. Silicon dioxide (SiO<sub>2</sub>) and titanium dioxide (TiO<sub>2</sub>) films were prepared by reactive e-beam evaporation of silicon dioxide and titanium(III) oxide (Ti<sub>2</sub>O<sub>3</sub>). During the deposition, partial pressure of oxygen was at  $9 \times 10^{-5}$  torr for TiO<sub>2</sub> and  $5 \times 10^{-5}$  torr for SiO<sub>2</sub>. The deposition rates of SiO<sub>2</sub> and TiO<sub>2</sub> films were 1 nm/s. The substrate temperature during deposition was 215 °C. Thicknesses of dielectric layers were 100 nm and mass thickness of gold films was 7 nm.

## 3.2. Materials

Silver, gold and copper, which are noble metals, were the main materials studied in this thesis because of their plasmonic properties.

BK7 glass is a widely used borosilicate glass of optical quality. Borosilicate glass is a type of glass with the main glass-forming constituents: silica (silicon dioxide) and boron oxide. Softening point of BK7 glass is at 550 °C. It is chemically resistant.

Optically, borosilicate glasses have low dispersion and relatively low refractive indices (1.51 – 1.54 across the visible range). Their optical properties are homogeneous through the substrate. BK7 glass has significant absorption at wavelengths below 380 nm.

SiO<sub>2</sub> is a favourable low refractive index material with refractive index of 1.45 – 1.50 at 500 nm. It can be deposited with good adhesion to dielectric substrate and it has a good mechanical durability. It is appropriate for applications in UV and visible range, i.e. for range between 250 nm and 1100 nm. Films are amorphous and they have compressive stress. Crystallisation occurs upon thermal treatment at temperatures above 1100 °C. When evaporated with electron beam gun, the amount of material deposited on a monitor chip or quartz crystal does not have the expected reproducible ratio to that received at other positions in the chamber. This is explained by erratic melting/sublimation of SiO<sub>2</sub> in both, granular and solid disc forms.

TiO<sub>2</sub> is the most widely used material in optical coatings for the visible range due to its high refractive index of 1.9 – 2.6 at 500 nm and good mechanical properties. Sub-oxide free films start to absorb below 400 nm and therefore the material is not appropriate for UV coatings. The TiO<sub>2</sub> films are crystalline with rutile or anatase phases or their mixtures. Refractive index varies a lot depending on deposition technique and conditions, especially on pressure and rate of deposition [87].

Using TiO<sub>2</sub> in combination with SiO<sub>2</sub>, it is possible to obtain multilayer of high number of layers having excellent durability and stability due to mutual compensation of stress.

### 3.3. Optical characterisation techniques

Spectrophotometry and spectroscopic ellipsometry are very well established and widely used experimental techniques for characterisation of optical properties of materials. Both techniques were used in optical characterisation of samples in this research and their description is given in the following subsections.

For extracting relevant information from optical experiments the same general procedure is usually applied [83]. They never directly measure the sample parameters of interest (optical constants, thicknesses, etc.); rather they measure some quantity that is a function of the parameters of interest. It is then necessary to solve the inverse problem of modelling the measured data to estimate the values of the sample parameters that yield data predicted from the model which best match the measured data. This procedure may be divided into the following four steps, as illustrated in Figure 3.1.

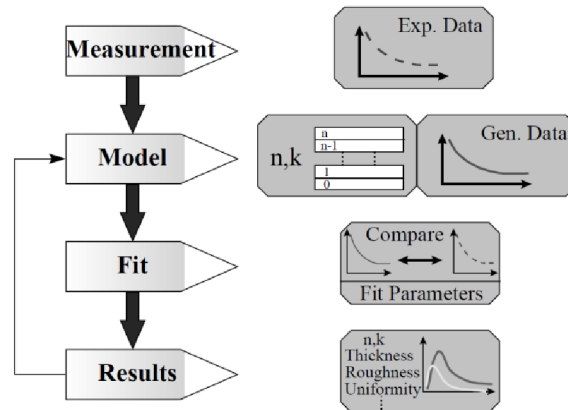


**Figure 3.1** Procedure to determine material properties from experimental data.

First, optical measurements are performed and experimental data are obtained. Then we must construct a model which can accurately describe our sample. The model contains some known parameters, such as the wavelength of the incident light, the incident beam polarization state and the angle of incidence, and some unknown physical parameters such as layer thicknesses and optical constants.

Next we optimize the model parameters to fit the measured data, i.e. vary the unknown physical parameters and generate data until we find a set of optimal parameters that yield calculated data that closely match measured optical data. When a set of physical parameters yielding calculated data which closely match the experimental optical data is found, we must establish that the best-fit set of parameters is unique, physically reasonable, and not strongly correlated. If these criteria are met, we can conclude that the best-fit model probably represents the physical reality of the sample.

### 3.3.1. Spectrophotometry

Spectrophotometry measures reflectance and/or transmittance of a sample over a defined spectral range. The light beam from a source is transmitted through a sample or reflected from a sample and the ratio between the transmitted/reflected and incident intensities is determined. If a spectrophotometer is equipped with integrating sphere, scattering measurements are also possible.

According to wavelength region accessible to measurement and experimental method implemented, spectrophotometers may be divided to dispersive spectrophotometers and Fourier Transform Infrared (FTIR) spectrophotometers. Dispersive spectrophotometers measure usually in the wavelength region from 200 nm to 3000 nm (which spans ultraviolet, visible and near infrared; UV-VIS-NIR). FTIR spectroscopy measures in the range from 2  $\mu\text{m}$  to 100  $\mu\text{m}$ . The main components of dispersive spectrophotometer are: light source, monochromator, optical system for light beam guidance and a detector.

Spectrophotometric measurements may be applied in determining of refractive index and thickness of the layers. But in this research, for the purpose of obtaining optical constant and layer thickness, spectroscopic ellipsometry is used because of higher sensitivity. Spectrophotometry is used to acquire transmittance and reflectance measurements, from which optical loss is calculated. Clear identification of LSP resonance in optical spectrum is thus possible by spectrophotometry and, accordingly, tracking LSP behaviour with changes in sample preparation parameters.

The LSP resonance properties of the samples were studied by analysis of optical loss using optical spectroscopy in the 300 nm – 1100 nm spectral range. In order to do this, transmittance ( $T$ ) and reflectance ( $R$ ) measurements were performed using a Perkin-Elmer spectrometer Lambda 25. Optical loss  $L$  was then calculated according to the formula:  $L = I - T - R$  (where  $L \equiv S + A$  is the sum of scatter  $S$  and absorptance  $A$ ) [88]. Typical value of experimental error, without systematic errors, is 0.15% for transmittance and 0.3% for reflectance at normal incidence (it is not possible to perform actual reflectance measurements at completely normal incidence, so special attachments are used and reflectance measurements are usually done at 6° angle of incidence and this is taken as normal incidence).

### 3.3.2. Variable angle spectroscopic ellipsometry

Optical constants of the bare BK7 substrates, silver, copper and gold MIFs samples were determined using spectroscopic ellipsometry under different angles of incidence (50° and 60° for BK7 substrates; 65° and 75° for silver and copper MIFs; 35°, 45°, 55°, 65° and 75° for gold MIFs) and transmittance measurements at normal incidence in 300 nm – 1650 nm spectral range (corresponding to 0.75 eV – 4.1 eV). J.A. Woollam Co. V-VASE variable angle spectroscopic ellipsometer was used. Fitting of experimental data was done using WVASE32 software (J.A. Woollam Co.). The optical model for MIFs was implemented in the WVASE32 software using “GenOsc” function [83].

The problem of incoherent backside reflections for silver and copper MIFs samples was solved by roughening back side of BK7 substrates using mechanical grinder. In the analysis of gold MIFs, incoherent backside reflections of the samples were accounted for in WVASE32 by including the number of backside reflections parameter in the optimization process [83].

For evaluation of fit quality the mean squared error (*MSE* in (3.1)) was used which quantifies the difference between model and experiment for all regressed quantities. The random measurement error for each data point was incorporated via the following *MSE* equation:

$$MSE^2 = \frac{1}{(2N_\lambda N_\alpha + N_\lambda) - M} \sum_{i=1}^{N_\lambda} \left\{ \sum_{\alpha=1}^{N_\alpha} \left[ \left( \frac{\Psi_{i,\alpha}^{Mod} - \Psi_{i,\alpha}^{Exp}}{\sigma_{\Psi_{i,\alpha}}^{Exp}} \right)^2 + \left( \frac{\Delta_{i,\alpha}^{Mod} - \Delta_{i,\alpha}^{Exp}}{\sigma_{\Delta_{i,\alpha}}^{Exp}} \right)^2 \right] + \left( \frac{T_i^{Mod} - T_i^{Exp}}{\sigma_{T_i}^{Exp}} \right)^2 \right\} \quad (3.1)$$

$$= \frac{1}{N - M} \chi^2,$$

where  $\Psi_{i,\alpha}^{Exp}$ ,  $\Delta_{i,\alpha}^{Exp}$  and  $T_i^{Exp}$  are experimental ellipsometric angles and transmittance data.  $\Psi_{i,\alpha}^{Mod}$ ,  $\Delta_{i,\alpha}^{Mod}$  and  $T_i^{Mod}$  are corresponding model quantities.  $\sigma_{\Psi_{i,\alpha}}^{Exp}$ ,  $\sigma_{\Delta_{i,\alpha}}^{Exp}$  and  $\sigma_{T_i}^{Exp}$  are the standard deviations of the experimental data points  $\Psi_{i,\alpha}^{Exp}$ ,  $\Delta_{i,\alpha}^{Exp}$  and  $T_i^{Exp}$ .  $N_\lambda$  is the number of photon energies in each spectrum,  $N_\alpha$  number of angles of incidence in ellipsometric measurements, and  $N$  is the total number of data points. Compared with well known likelihood estimator, the chi-square ( $\chi^2$ ), the *MSE* expression is normalized by the pre-factor so it is not directly affected by the change in the number of data points  $N$  or number of free fit parameters  $M$ .

## 3.4. Structural characterisation techniques

The morphological and structural properties of nanomaterials are usually addressed by a wealth of techniques such as Transmission Electron Microscopy (TEM), High resolution Scanning Electron Microscopy (SEM), Scanning Tunnelling Microscopy (STM) or Atomic Force Microscopy (AFM), laboratory X-ray diffraction (XRD), and synchrotron radiation based X-ray techniques.

### 3.4.1. Atomic force microscopy

The AFM provides the morphological information for particles on top of a surface. It also has some limitations, such as limited statistics, the problem of convolution with the tip shape, problems with in situ measurement during growth because of shadowing effects and temperature drift. Therefore long acquisition times and interruption of the growth process are needed. The AFM cannot be used for particles embedded in matrix, below the surface and most other techniques are destructive. Complementary information can be obtained in reciprocal space using X-ray scattering.

The AFM of silver and copper MIFs were performed with a Dimension 3100 (Digital Instruments) instrument in the tapping mode. The radius of the tip was  $\leq 10$  nm. Lateral accuracy was typically within 1 %. AFM was used for the island morphology characterisation as a complementary method to GISAXS. These measurements were performed in Joanneum Research, Institute of Nanostructured Materials and Photonics in Weiz, Austria.

The other AFM measurements was performed at “Ruđer Bošković” Institute in Zagreb where the surface topography of gold MIFs was determined using a MultiMode Probe Microscope with the Nanoscope IIIa controller (Veeco Instruments Inc.) and a ”J” scanner with a vertical engagement (JV) 125  $\mu\text{m}$  (AS-130V scanner, Veeco Instruments, Santa Barbara, CA). Imaging was operated in the ”tapping mode” using silicon tip (TESP, Veeco, nominal frequency 320 kHz, nominal spring constant of 42 N/m) under ambient conditions in the air. The linear scanning rate was optimized between 1.0 Hz and 2.0 Hz at a scan angle of  $0^\circ$ . Data were collected with  $(512 \times 512)$  pixel number. The radius of the tip was  $\leq 10$  nm.

### 3.4.2. Grazing-incidence small-angle X-ray scattering

GISAXS measurements were performed at the Austrian SAXS beam line [89, 90] at the Synchrotron ELETTRA, Trieste, Italy. GISAXS setup data were: X-ray photon energy was 8 keV (i.e. wavelength  $\lambda = 0.154$  nm); energy resolution ( $\Delta E/E$ ) was  $\leq 2.5 \times 10^{-3}$  and focal spot size FWHM was  $(4 \times 0.15)$  mm<sup>2</sup>.

The GISAXS intensity curves are obtained from the scattering pattern recorded by a two-dimensional charge-coupled device (CCD) detector with image sizes of  $1024 \times 1024$  pixels. The distance between the sample and detector was  $L = 1.5$  m. A motorized Al beam absorber was positioned perpendicular to the sample surface to reduce the transmitted and specularly reflected beams. The samples were mounted on a stepper-motor-controlled tilting stage with a step resolution of  $0.001^\circ$  and measured at the chosen grazing angles. GISAXS for each sample was measured at critical angle and also at one slightly larger angle.

Analysis of GISAXS intensity patterns was done using Guinier approximation. For gold MIFs samples, IsGISAXS program was used for simulation and fitting of experimental data of islands on a substrate [91]. IsGISAXS program provides a wide variety of calculation frameworks: different scattering formalism, different form factor calculation formalisms, various particle shapes and size distributions; interference functions: lattice (perfect or with defects), random distributions, para-crystal model. Further details are given in the Appendix.

## 4. Localized surface plasmons of noble metals

As an introduction to a series of experimental results that will be presented and discussed in the following chapters, optical transmittance spectra of silver, gold and copper island films will be shown which were prepared under different deposition conditions and with different dielectric environment. Optical properties of these samples illustrate important phenomena which are the subjects of this thesis.

Optical transmittance spectra of samples with silver, gold and copper metal island films, all with mass thickness of 7 nm, deposited at hot substrates (220°C) and coated with a 10 nm SiO<sub>2</sub> protective dielectric layer are shown in Figure 4.1.

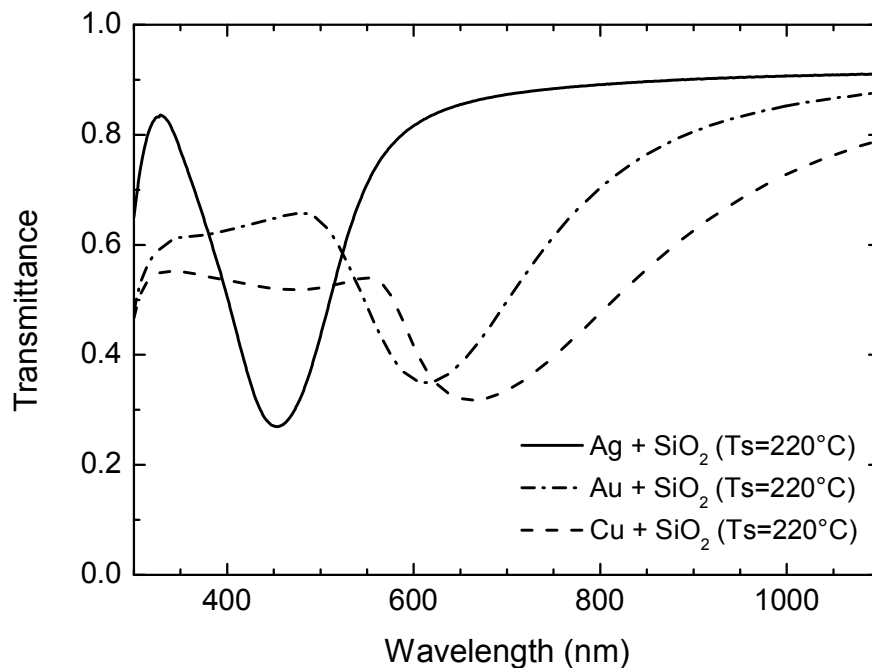


**Figure 4.1** Transmittance spectra of samples with silver, gold and copper metal island films obtained at hot substrates (220 °C) and coated with 10 nm SiO<sub>2</sub> protective layer.

The optical properties in the spectral range of interest are dominated for all the samples by the LSP resonance of free electrons in clusters. The LSP resonance is shown by a minimum in transmission spectra which is positioned in the blue part of the spectrum for silver and in the red part for gold and copper. Beside red shift of the resonance, going from silver to copper, a broadening of the resonance is observed. Transmittance is additionally lowered in the blue part of the spectrum for gold and copper because of interband transitions of these metals. Strong interband absorption very close to the LSP resonance characterizes copper.



Optical transmittance spectra of samples with silver metal island films obtained under different conditions: at hot substrate (220 °C) and coated with SiO<sub>2</sub> or TiO<sub>2</sub>, and at cold substrate and coated with SiO<sub>2</sub> or TiO<sub>2</sub> are shown in Figure 4.2.

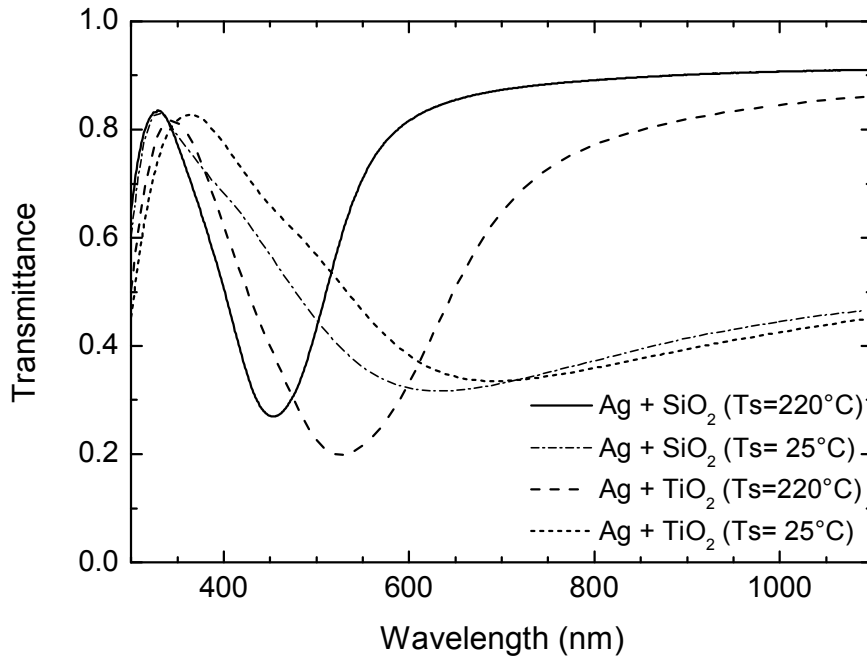


**Figure 4.2** Transmittance spectra of samples with silver metal island films obtained under different conditions: at hot substrate (220 °C) and coated with SiO<sub>2</sub> or TiO<sub>2</sub>, and at room temperature substrate and coated with SiO<sub>2</sub> or TiO<sub>2</sub>.

The blue shift of LSP resonance for silver metal islands coated by SiO<sub>2</sub>, compared with those coated by TiO<sub>2</sub>, can be understood from the dielectric function of silver (see Figure 2.2). As TiO<sub>2</sub> has a higher dielectric constant than SiO<sub>2</sub>, the resonance condition will occur for more negative values of the real part of the dielectric constant of silver, i.e., at longer wavelengths. The analysis of the resonance condition for single small spherical particles, however, cannot explain the changes on the SP characteristics depending on the substrate temperature. These changes must be attributed to the modification of the geometrical arrangement of the metal clusters depending on the substrate temperature. Indeed, clusters grown at cold substrates typically present a wider size and shape distribution and higher percolation degree [92], resulting in an increase of the cluster-cluster interaction and leading to a broader LSP resonance [73].

## 5. Silver metal island films on glass substrates

### 5.1. Optical characterisation of silver MIFs

#### 5.1.1. Spectrophotometry of silver MIFs

It is quite rewarding to have qualitative information about optical behaviour of samples immediately after finishing the deposition procedure. Differences on LSP resonance position in the visible spectrum for the samples may be easily detected by an eye. The trends of colour change (of light reflected from the sample surface) both with increase of substrate temperature and with deposited mass thickness increase, are easily seen in Figure 5.1.

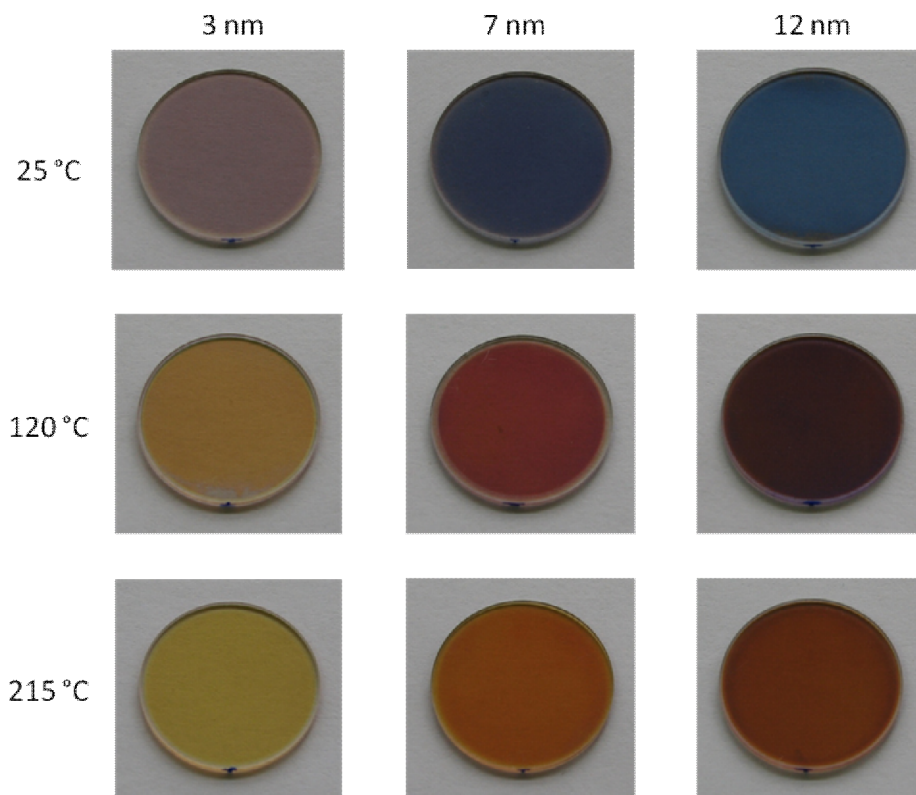


**Figure 5.1** Photographs of silver MIFs samples in case of three deposition temperatures; 25 °C, 120 °C and 215 °C (presented in rows from top to the bottom) and for deposition thicknesses of 3 nm, 7 nm and 12 nm (presented in columns from left to right).

A quantitative assessment of the optical properties of silver MIFs was done by transmittance and reflectance measurements of the samples. The optical loss was then calculated as  $100\% - T - R$  and used for tracking LSP resonance of samples. The LSP resonance trend with the increase of the substrate temperature during deposition is displayed in the Figure 5.2.

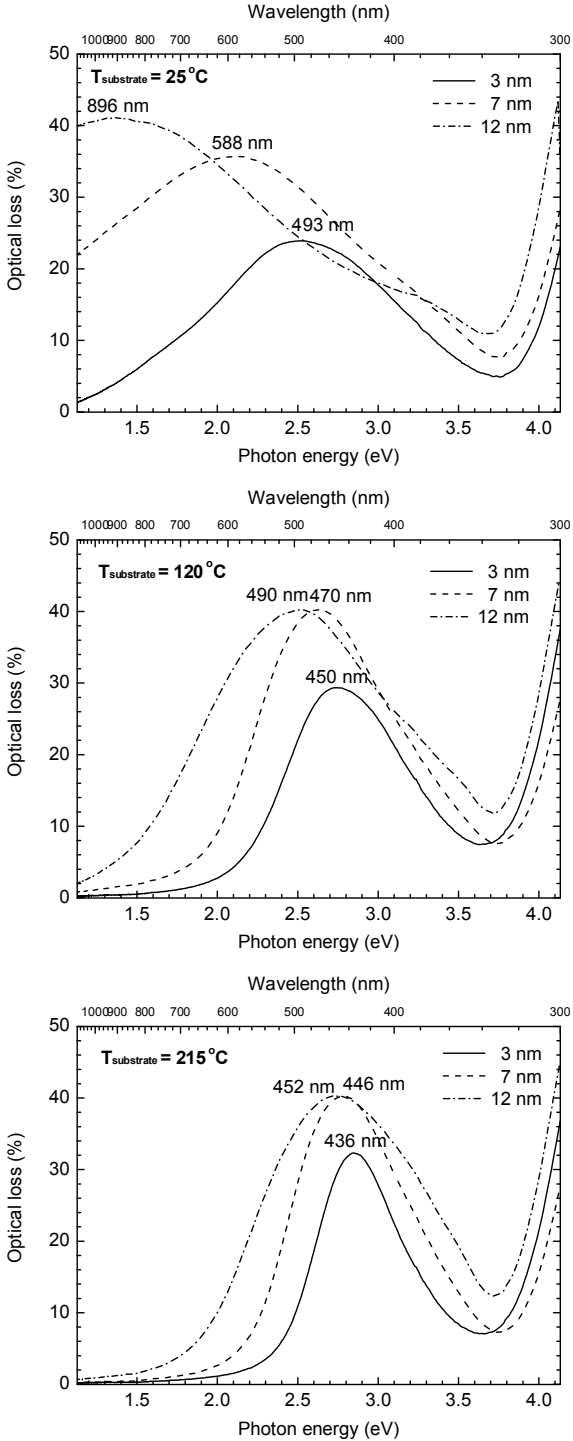


**Figure 5.2** The evolution of LSP resonance with substrate temperature increase (increasing temperature from the top to the bottom of the figure) for the samples with 3 nm, 7 nm and 12 nm mass thickness of deposited Ag.

The Figure 5.3 displays the change of LSP resonance with the increase of the deposited mass thickness of silver.

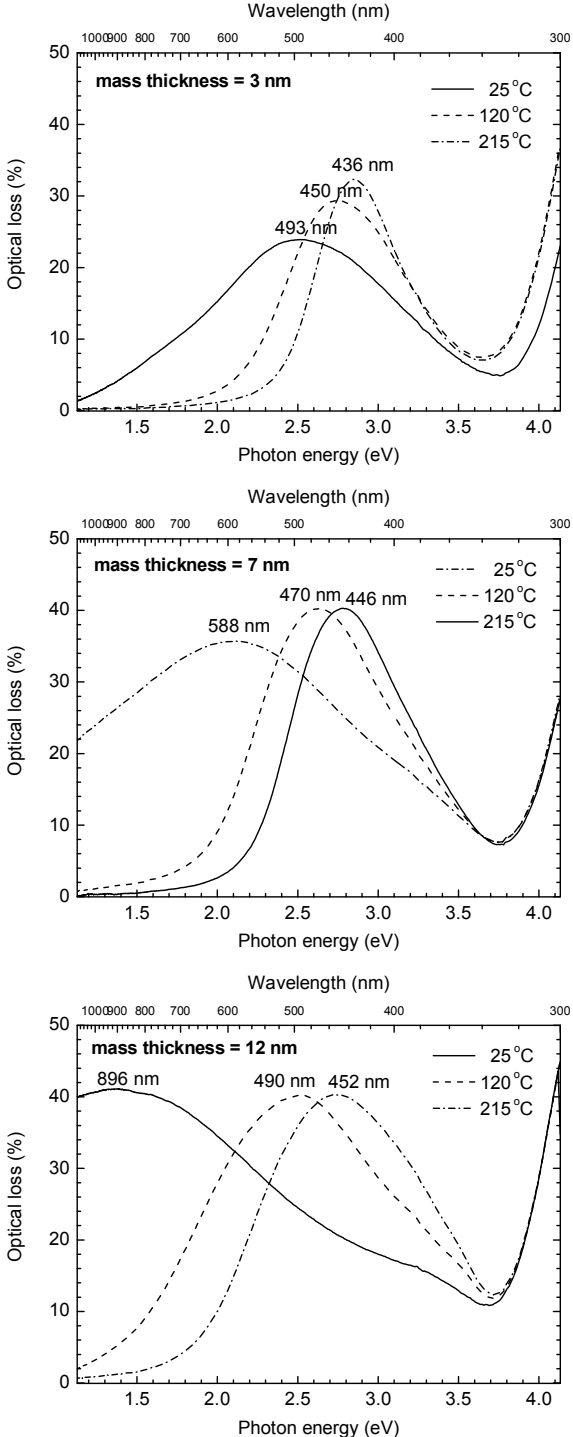


**Figure 5.3** The evolution of LSP resonance with increase of mass thickness of deposited Ag (increasing mass thickness from the top to the bottom of the figure) for the samples with 25 °C, 120 °C and 215 °C substrate temperatures during deposition.

All the spectra are characterized by a peak related to the LSP resonance. Two main effects are observed: i) red shift and widening of the LSP resonance with the increase of deposition thickness and ii) blue shift and narrowing of LSP resonance with the increase of deposition temperature.

Red shift, broadening and intensity increase of LSP resonance with deposited mass thickness may be explained by modelling MIF-SiO<sub>2</sub> layer as a composite film with optical constants that can be calculated using Maxwell Garnett model. The results of Maxwell Garnett simulation are presented in section 2.4.1 using the Drude model for the dielectric function of silver and with the confinement effect incorporated through the increase of damping constant (see equation (2.77)). It was thus possible to show that the LSP resonance becomes more intense, broader and red shifted when the concentration of silver increases. Blue shift and narrowing of LSP resonance with temperature are effects that could be attributed to the combination of morphological trends with temperature (increase of particle sphericity, interparticle distance and particle size). This topic is further studied in the section 5.2 where structural properties of silver MIFs are investigated.

### 5.1.2. Variable angle spectroscopic ellipsometry of silver MIFs

The series of five silver MIF samples with the mass thickness of 7 nm and substrate temperatures of 25 °C, 75 °C, 125 °C, 175 °C and 215 °C were prepared without SiO<sub>2</sub> capping layer.

Optical properties of bare BK7 glass substrates were measured prior to deposition of MIFs. BK7 glass is transparent for the visible light with absorption edge in the UV, so Cauchy dispersion model and Urbach absorption in high energy region were used in optical characterization. The complex dielectric function obtained for BK7 glass substrates was fixed in the further modelling of the silver MIFs.

Silver MIFs were modelled as a homogeneous layer with effective dielectric function and layer thickness (see section 2.4). The analysis started with a point by point fit, keeping effective layer thickness value  $d_{eff}$  equal to the mass thickness. In the point by point fit, the effective optical constants are determined for each photon energy by inversion from  $\Psi$  and  $\Delta$ . It yielded acceptable agreement to measured data. Although point by point fit does not guarantee Kramers-Kronig consistency, it gives some valuable physical information about the dispersion of optical constants due to the different light-matter interaction phenomena which occur in the investigated spectral range. Based on the results of point by point fit, it was possible to identify different phenomena which determine optical properties of silver MIFs: i) a strong absorption between 1.8 eV and 2.9 eV attributed to LSP resonance, ii) a tail of interband transition absorption of silver in UV and iii) a Drude-like infrared absorption shoulder (only for the sample with of 25 °C substrate temperature) which indicates metallic behaviour and suggests a possible percolation of islands.

Finally, multiple oscillator model described in the section 2.4.2 was used (2.79), with Gaussian oscillators modelling LSP resonance and interband transitions, and Drude oscillator in the low photon energy part of spectrum for the sample with 25 °C substrate temperature. The choice of Gaussian oscillators instead of Lorentz oscillators was based on the results of more detailed analysis applied for gold samples which will be presented in section 7.1. *MSE* values obtained were between 1.6 and 3.9.

The effective dielectric functions of the silver MIF samples are presented in Figure 5.4.

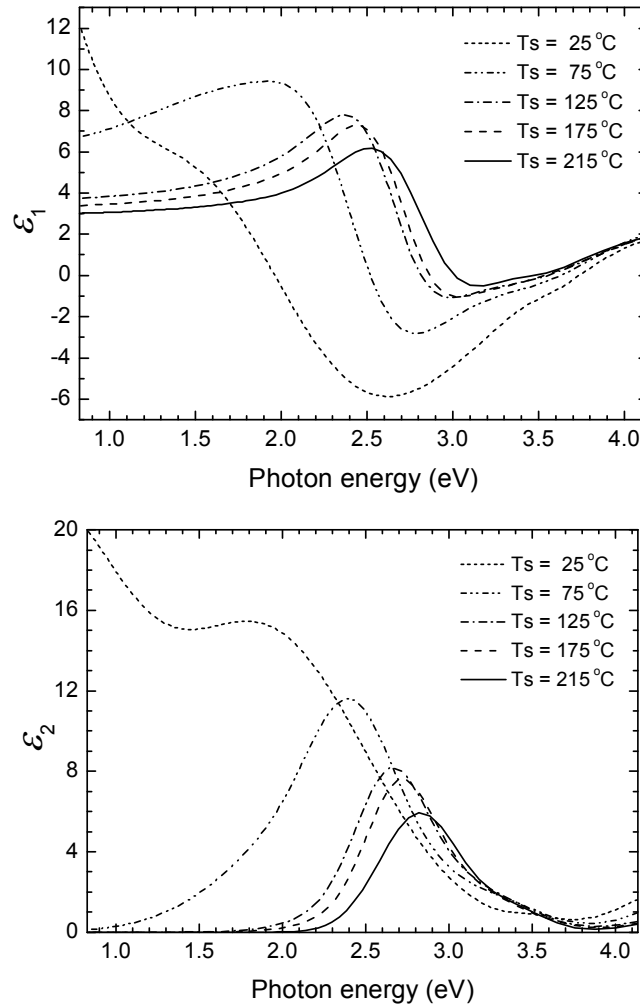


**Figure 5.4** The real and imaginary part of the effective dielectric function of silver MIF samples with mass thickness 7 nm in case of five substrate temperatures during the deposition: 25 °C, 75 °C, 125 °C, 175 °C and 215 °C.

The effective layer thicknesses of the silver MIF samples are presented in Table 5.1.

**Table 5.1** The effective layer thicknesses of the samples

$T_s$ (°C)	25 °C	75 °C	125 °C	175 °C	215 °C
$d_{eff}$ (nm)	$8.0 \pm 0.2$	$14.0 \pm 0.9$	$18.9 \pm 0.2$	$20.9 \pm 0.3$	$26.5 \pm 0.3$

The main results of the ellipsometry study of silver MIFs are: i) there is blue shift, narrowing and intensity decrease of LSP resonance with temperature and ii) effective layer thickness increases with temperature indicating the formation of larger particles. For the sample with 25 °C substrate temperature, indication of percolation of islands is present.

## 5.2. Structural characterisation of silver MIFs

Structural characterization of silver MIFs was done using AFM and GISAXS with the aim to explore the relation between optical and structural properties.

### 5.2.1. Atomic force microscopy of silver MIFs

Figure 5.5 presents AFM micrographs of silver MIFs samples. It was observed that the lateral size of the islands shows an increase with the increase of deposition thickness as well as with the substrate temperature. Quantitative analysis is in Table 5.2.

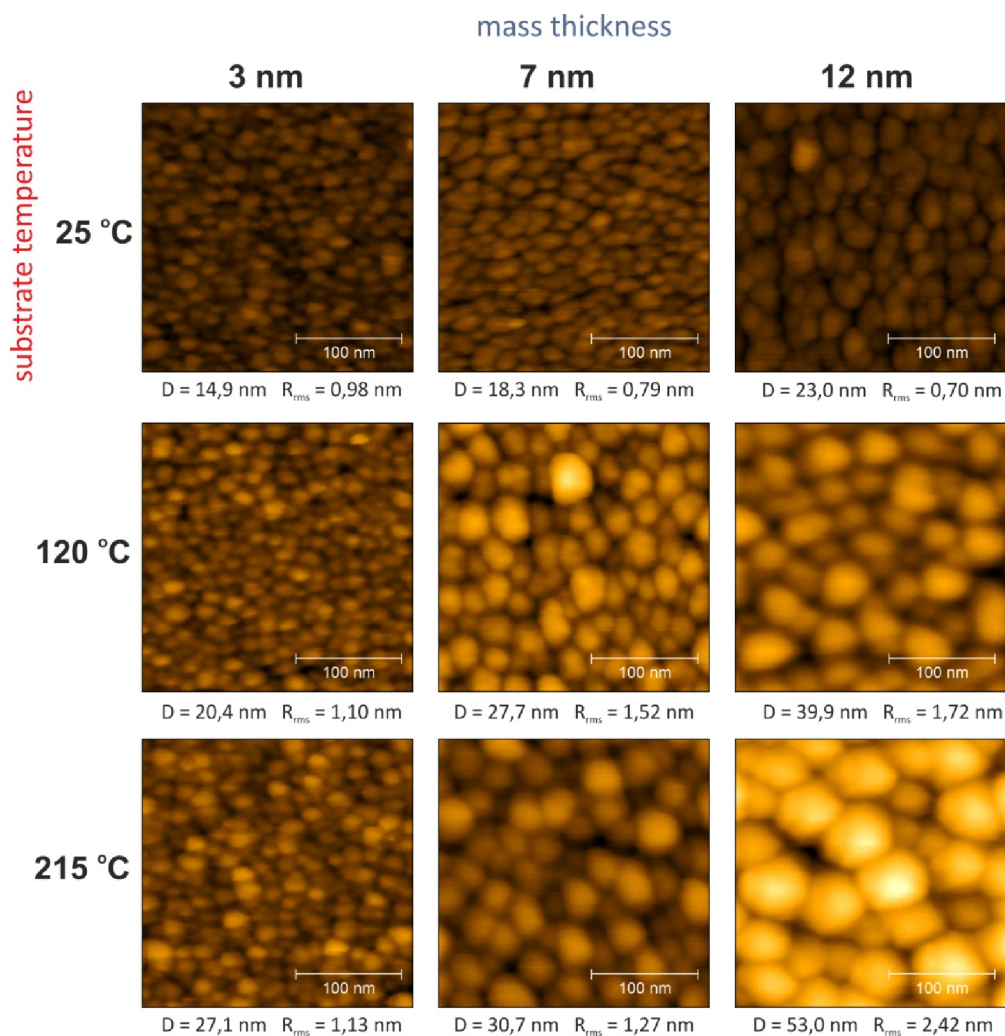


**Figure 5.5** AFM micrographs of silver MIFs samples for three deposition temperatures; 25 °C, 120 °C and 215 °C (presented in rows from top to the bottom) and for deposition thicknesses of 3 nm, 7 nm and 12 nm (presented in columns from left to right).



### 5.2.2. GISAXS of silver MIFs

To obtain quantitative structural information about silver MIFs, GISAXS measurements were done. Figure 5.6 depicts 2D GISAXS scattering patterns of the silver MIFs samples.

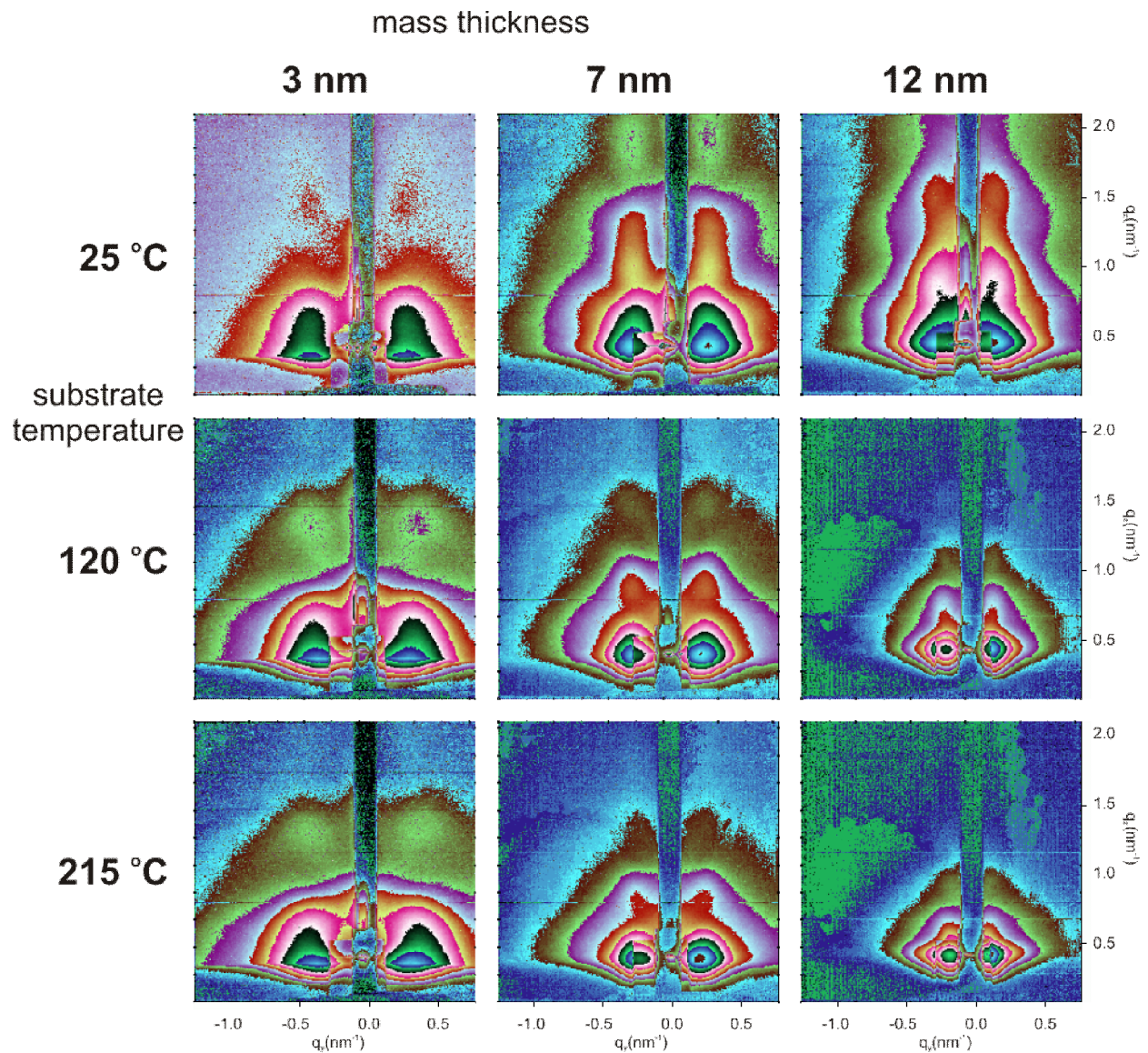


**Figure 5.6** 2D GISAXS scattering patterns for measured silver MIFs samples. The first column presents samples with 3 nm deposited mass thickness, the second with 7 nm and the third with 12 nm. The first row presents samples deposited at 25 °C, the second at 120 °C and the third at 215 °C.

In all cases well-defined areas of maximal intensities at both sides of the beam stop can be observed. The scattered intensity concentrates more and more towards the origin of the reciprocal space as the deposited Ag thickness increases (see Figure 5.6 from left to the right) as well as the deposition temperature increases (see Figure 5.6 from top to the bottom). This reveals the growth of island sizes in all real-space directions as expected [93] and this assumption will be proved later in this section.

In each pattern in Figure 5.6 two maxima situated parallel to the  $q_y$  axis are separated by the partly seen (partly screened by the beam stop) specular rod at  $q_y = 0 \text{ nm}^{-1}$ . This interference effect arises because there is a preferential closest neighbour centre-to-centre distance ( $D$ ) between the islands [93]. This intensity is oscillating in  $z$  direction due to interference effects in the  $\text{SiO}_2$  capping layer.

The island size analysis was performed using a simplified approach.  $D$  was determined by direct extraction from the position of the intensity maximum  $q_m$  using the “Bragg” law ( $D = 2\pi/q_m$ ). In order to determine the average vertical and lateral size of the silver islands, 1D vertical (i.e. perpendicular to the sample surface at  $q_m$ ) and horizontal cuts (i.e. parallel to the sample surface at  $q_m$ ) of a 2D GISAXS patterns were done, respectively. When the Guinier’s approximation (explained in Section 2.6.1) [84, 94] is applied to the vertical and horizontal cut data the respective island sizes are estimated. The obtained vertical and horizontal island’s average sizes clearly show the trend of growing with both the deposition thickness and deposition temperature. The GISAXS characterisation results are presented in Table 5.2.

**Table 5.2** Characterization results obtained by three methods (spectroscopy, GISAXS and AFM) for all measured silver MIFs samples.  $\lambda_{\text{peak}}$  is the position of the LSP resonance peak maximum,  $\Delta\lambda_{\text{FWHM}}$  is the respective peak width (full width at half maximum).  $D$  represents average interparticle centre-to-centre distance,  $R_{\text{rms}}$  is the film surface roughness,  $H$  is the islands' average vertical size (height) and  $d$  is their average horizontal (lateral) size, all in nanometres (nm).

Ag samples		Methods						
		Spectroscopy		AFM			GISAXS	
		$\lambda_{\text{peak}} / \text{nm}$	$\Delta\lambda_{\text{FWHM}} / \text{nm}$	$D / \text{nm}$	$R_{\text{rms}} / \text{nm}$	$H / \text{nm}$	$d / \text{nm}$	$D / \text{nm}$
3 nm	25 °C	497	297	15,7	0,98	5,6	8,2	17
3 nm	120 °C	464	170	22,1	1,10	7,4	9,4	17
3 nm	215 °C	455	126	20,8	1,13	7,8	9,2	17
7 nm	25 °C	591	–	17,7	0,79	14,0	11,2	24
7 nm	120 °C	490	212	27,1	1,52	13,0	14,0	30
7 nm	215 °C	461	171	32,0	1,27	14,8	14,8	30
12 nm	25 °C	940	–	24,3	0,70	10,0	13,4	39
12 nm	120 °C	547	398	40,7	1,72	14,2	21,0	41
12 nm	215 °C	476	248	51,9	2,42	18,6	23,0	47

For a more precise determination of the island sizes and interparticle distances, only the direct modelling of the data is adequate. It should include reflection-refraction effects, the coupling between interference function and the island's form factor which greatly increases the complexity of the analysis [91, 93, 95].

The most evident trends of the geometrical properties of the clusters with the deposition parameters are the increase of the interparticle distance and sizes in all directions with the deposited mass thickness. Such trends are explained by the typical growth mechanism of metal films [49] that starts with a nucleation process that gives place to small clusters and as the amount of deposited metal increases, the clusters start to coalesce and form bigger islands. A secondary trend observable from the structural characterization is an increase of the particle size, together with an increase of the interparticle distance, as the deposition temperature increases. The formation of larger, more spherical and more separated islands, also reported in [96], is connected to the higher energy available to silver atoms arriving to a hotter substrate.

The discrepancy between the interparticle distances extracted from GISAXS and AFM is up to 25 % (except for films of 7 nm and 12 nm thickness deposited at 25 °C). It must be noticed that GISAXS technique provides a more complete description of the clusters geometry. Due to the presence of the protective SiO<sub>2</sub> layer, no information on the vertical and horizontal dimensions of the islands is available from AFM since the bottom of the islands is not reachable by an AFM tip, and only the centre-to-centre distance can be estimated. Even without the presence of a SiO<sub>2</sub> layer, the determination of islands' dimensions might be limited by the convolution of islands' shape with the tip shape. Nevertheless, AFM can provide some qualitative information on the vertical dimensions of the islands, since it is possible to observe an increase of the surface roughness with temperature and deposited mass thickness. Such increase of roughness can be explained by the formation of a less smooth SiO<sub>2</sub> surface due to an increase of the islands' vertical dimension, as confirmed by GISAXS.

A broadening and red shift of the LSP peak characterize the evolution of the optical properties of MIFs with the amount of deposited Ag. Such behaviour can be qualitatively explained by modelling the MIF-SiO<sub>2</sub> layer as a composite film with optical constants that can be calculated using effective medium theories [97]. Using the Maxwell Garnett model [70], it is possible to show that when the concentration of silver increases in the composite film, the LSP resonance peak becomes broader and red shifted [98].

Regarding the evolution of LSP with temperature, blue shift and narrowing of the LSP resonance is observed. Such behaviour can be attributed to changes in: i) particle shape – LSP of spherical particles is blue shifted and narrower compared to that of elliptical particles [99]; ii) interparticle distance – interaction between particles is decreased when particles are more separated, leading to a broadening and blue shift of LSP [96]; iii) particle size – optical constants of small Ag particles are different from that of the bulk Ag due to the shorter mean free path of electrons. The change in optical properties depending on Ag cluster size leads to a broadening of the LSP peak for smaller particles [99]. Combination of these geometrical trends can be identified from the structural characterization of the islands. In order to precisely analyse the contribution of these three effects – shape and size of islands and interparticle distance – in the observed optical properties, modelling of the collective optical response of islands [46] is required. However, for such purpose a more precise knowledge of the size and shape distribution of islands is necessary. This information could be extracted by more complex analysis of GISAXS data [91, 93, 95] beyond the Guinier's approximation. Such approach was applied in the analysis of the gold MIFs.

## 6. Copper metal island films on glass substrates

The series of five copper MIFs samples were prepared, with the mass thickness of 7 nm and 25 °C, 75 °C, 125 °C, 175 °C and 215 °C substrate temperatures during the depositions, without SiO<sub>2</sub> protective layer. This was for the purpose of obtaining the information about the change of structural and optical properties of copper MIFs with respect to different substrate temperatures during the depositions.

### 6.1. Structural characterization of copper samples

#### 6.1.1. Atomic force microscopy of copper samples

The results of AFM of bare BK7 substrate and copper samples with 7 nm mass thickness of copper deposited at 25 °C and 215 °C substrate temperature are shown in the Figure 6.1.

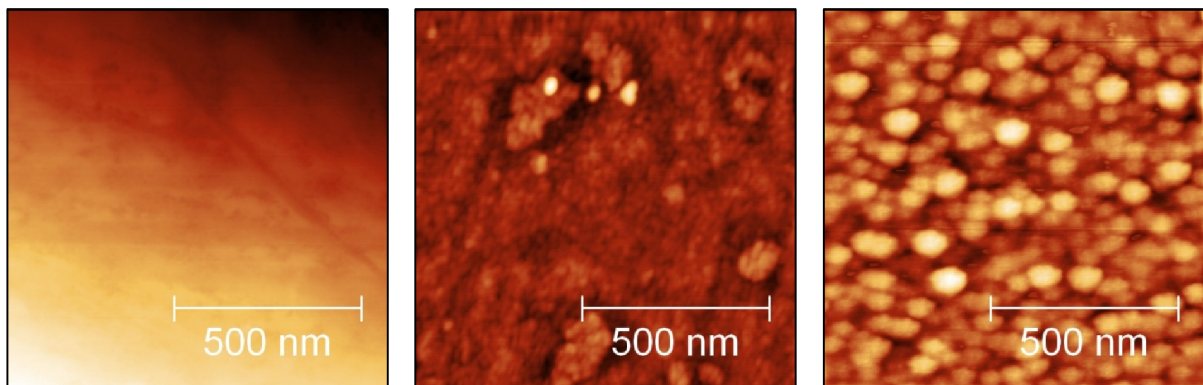


**Figure 6.1** The AFM of a) bare BK7 substrate, b) copper sample with 7 nm mass thickness deposited at 25 °C and c) copper sample with 7 nm mass thickness deposited at 215 °C.

The AFM micrographs of the copper MIFs confirm the formation of copper nanoparticles in the case of high substrate temperature (215 °C) when enough energy is available for atoms coming to the substrate surface to follow Vollmer-Weber growth mode. For sample deposited at 25 °C, the film of percolated small clusters is formed with some large clusters of percolated copper also present on the film. Compared with silver samples deposited at 25 °C, for the corresponding copper sample it seems that growth of nanoparticles is less favourable for copper. This behaviour is further investigated with GISAXS in the following section.

### 6.1.2. GISAXS of copper samples

The GISAXS measurements of 7 nm mass thickness copper samples were done to obtain information about the change of structural properties with substrate temperature during the deposition. The results are shown in the Figure 6.2.

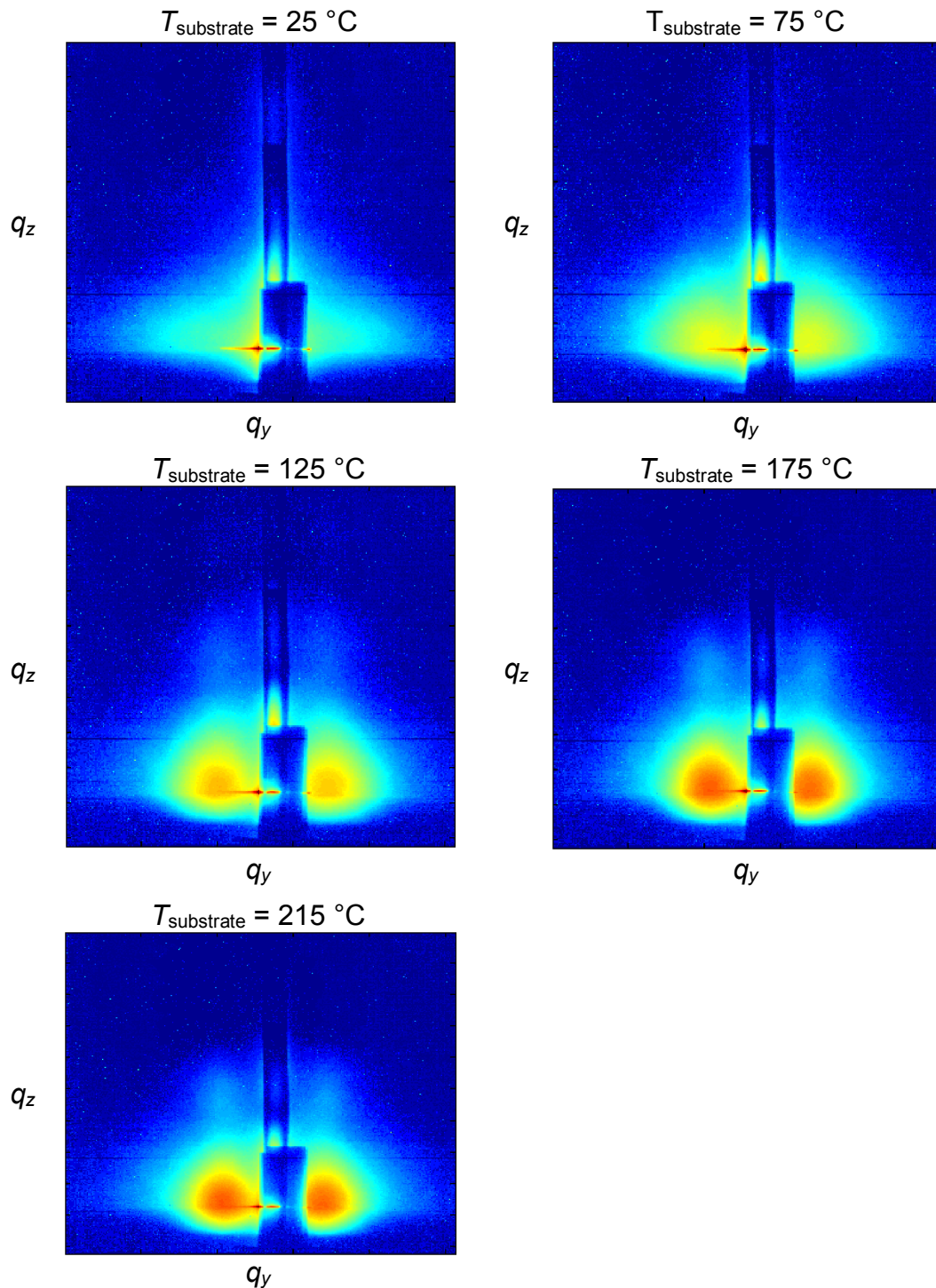


**Figure 6.2** 2D GISAXS scattering patterns of copper samples with 7 nm mass thickness deposited with substrate temperatures: 25 °C, 75 °C, 125 °C, 175 °C and 215 °C.

The GISAXS scattering patterns reveal that the copper MIFs are composed of nanometric clusters distributed at the sample surface in the case of 125 °C, 175 °C and 215 °C substrate temperatures, as evidenced by the presence of two lobes of scattered light symmetric with respect to the incidence angle. For higher substrate temperatures the intensity of the scattered light is more concentrated at smaller angles, suggesting that the particle size increases with substrate temperature. Well defined areas of maximal intensities at both sides of the beam stop cannot be observed in samples with 25 °C and 75 °C indicating formation of compact films with much smaller surface roughness than in MIFs.

The strength of the metal-substrate interaction (see Table 2.1) for copper on SiO<sub>2</sub> (0.384) is larger than for silver on SiO<sub>2</sub> (0.188 – 0.214) thus indicating that higher substrate temperatures are needed for formation of copper nanoparticles [52]. The comparison of the results obtained using AFM and GISAXS of silver and copper samples clearly confirms this.

## 6.2. Optical characterisation of copper samples

Optical transmittance spectra measurements of copper MIFs samples gave the results in accordance with assumptions based on the results of GISAXS. The dip in the transmittance spectrum between 1.5 eV and 1.6 eV is clearly present for samples deposited at 125 °C, 175 °C and 215 °C (pronounced for samples deposited at 175 °C and 215 °C) which may be attributed to LSP resonance of copper nanoparticles (Figure 6.3).

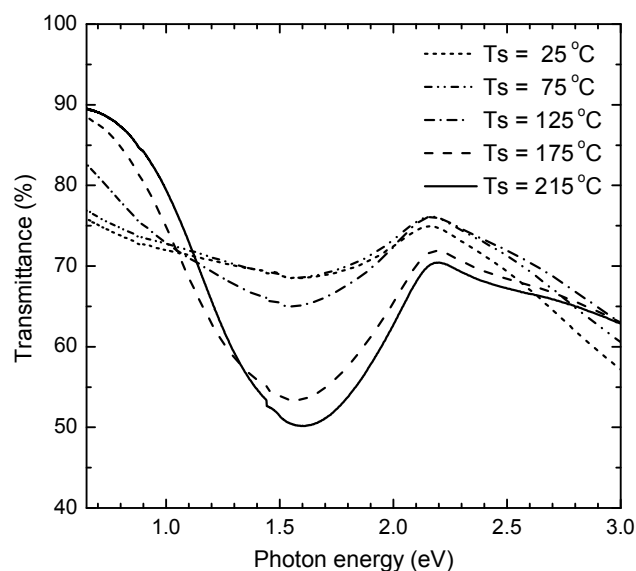


**Figure 6.3** Optical transmittance spectra of copper samples with 7 nm mass thickness deposited with substrate temperatures: 25 °C, 75 °C, 125 °C, 175 °C and 215 °C

The detailed optical characterization of copper samples was performed by variable angle spectroscopic ellipsometry using the same model and the same procedure as for silver (see Section 5.1.2). The strong absorption between 1.5 eV and 1.6 eV was attributed to LSP resonance. There was further absorption above approximately 2.2 eV due to interband transitions of copper. Drude-like absorption shoulder in NIR (which is pronounced for the samples with 25 °C and 75 °C substrate temperatures, and just emerging for the sample with 125 °C substrate temperature) indicated metallic behaviour and the percolation of islands. *MSE* values obtained were between 1.4 and 2.5

The results of the VASE analysis, real and imaginary parts of the effective dielectric function, are presented in Figure 6.4 and Figure 6.5.

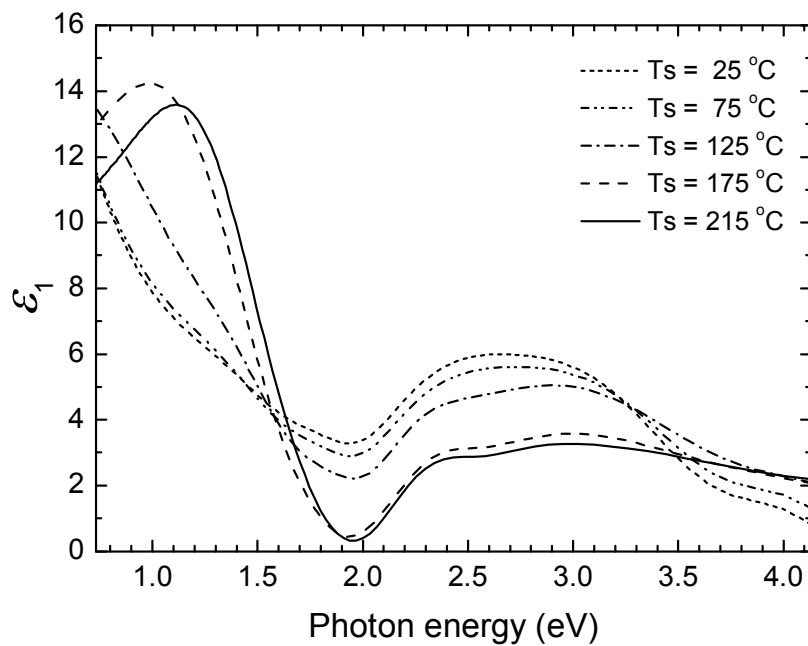


**Figure 6.4** The real part of the effective dielectric function of copper MIFs samples with mass thickness of 7 nm, for five different substrate temperatures during the depositions: 25 °C, 75 °C, 125 °C, 175 °C and 215 °C.



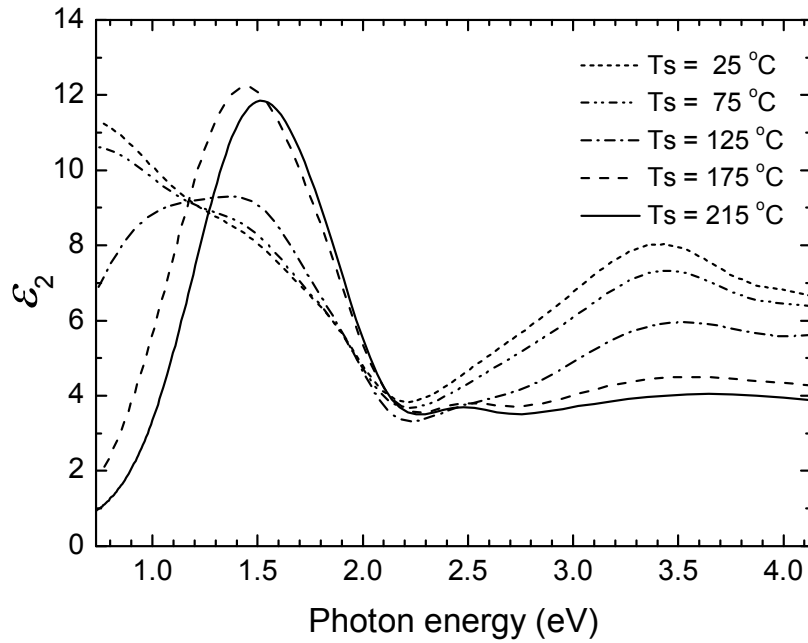


**Figure 6.5** The imaginary part of the effective dielectric function of copper MIFs samples with mass thickness of 7 nm, for five different substrate temperatures during the depositions: 25 °C, 75 °C, 125 °C, 175 °C and 215 °C.

The results of the structural characterization obtained by GISAXS show that the copper nanoparticles are formed at 125 °C, 175 °C and 215 °C and the optical characterization by the VASE show the presence of LSP resonance in these cases (Figure 6.5), with additional result showing that the percolation of clusters is present at 125 °C confirmed by emerging Drude tail in NIR.

Notice that the LSP resonance is positioned in the NIR and that the shift of resonance due to the change of substrate temperature is quite small compared to the one in the case of silver MIFs. Thus, the possibilities of tailoring optical properties of copper MIFs in visible spectrum with our experimental capabilities were quite limited. This, together with the existence of strong interband absorption of copper in visible spectrum, was the reason not to use copper in further investigation of MIFs embedded in multilayer structures.

## 7. Gold metal island films on glass substrates

Optical and structural properties of gold MIFs were investigated in more detail than those of silver and copper MIFs, as a prerequisite for later analysis of MIFs in multilayer structures. The main reason for this was the stability of gold MIFs during deposition of TiO<sub>2</sub> layer above MIF in elevated oxygen pressure environment. Oxidation of silver MIFs in the same conditions prevented the use of silver in the production of multilayer structures where MIFs are embedded between TiO<sub>2</sub> layers. The copper was not used in multilayers because of copper interband transitions present immediately after 2 eV and low LSP resonance tailoring potential with our experimental capabilities.

### 7.1. Optical characterisation of gold MIFs

Different approaches were tried to model the measured ellipsometric data for gold MIFs. At first, EMTs (Maxwell Garnett and Bruggeman) were tried. Here, the gold MIFs have been modelled as a mixture of gold and SiO<sub>2</sub>/air, with corresponding materials' optical constants taken from [100] and with volume fraction of components as optimization parameters. This approach was without success, with  $MSE > 20$  in all the samples.

The second approach starts with a point by point fit in which the effective optical constants are determined for each photon energy by inversion from  $\Psi$  and  $\Delta$ . It yielded acceptable agreement to measured data, but without guarantee for Kramers-Kronig consistency. Nevertheless, it gives valuable information about the dispersion of optical constants due to the different physical phenomena which occur in the investigated spectral range. Therefore, the point by point fit is the first step in a progress to build a physical dispersion model for the effective optical constants of gold MIFs.

Based on the results of point by point fit, it appeared that three different phenomena determine optical properties of gold MIFs: i) a strong absorption between 1.3 eV and 2.1 eV attributed to LSP resonance, ii) two weaker absorption peaks in UV connected to interband transitions of gold and iii) a Drude-like infrared absorption shoulder (only for certain samples) which indicates metallic behaviour and suggests a possible islands percolation [74].

After point by point fit, multiple oscillator approach was used. The total number of parameters optimized for each sample is obtained as a sum of three parameters for each Gaussian and Lorentz oscillator, two parameters for Drude oscillator (if it was used), one for effective layer thickness  $d_{eff}$ , one for  $\epsilon_{\infty}$  and one for number of backside reflections parameter. The number of parameters used in the analysis of our samples varied between 12 and 20 per sample.

As a result of simultaneous analysis of spectroscopic ellipsometry and transmittance measurements in the same point of the sample, the uniqueness of fit with respect to the effective layer thickness  $d_{eff}$  was achieved. If transmittance measurements were not included in fitting, the statistical uncertainty of the  $d_{eff}$  was significantly higher.

Experimental and model values of ellipsometric  $\Psi$  and  $\Delta$  together with measured normal incidence transmittance  $T$  in the same point of the sample are shown in Figure 7.1 for 7 nm mass thickness sample deposited at 120 °C.

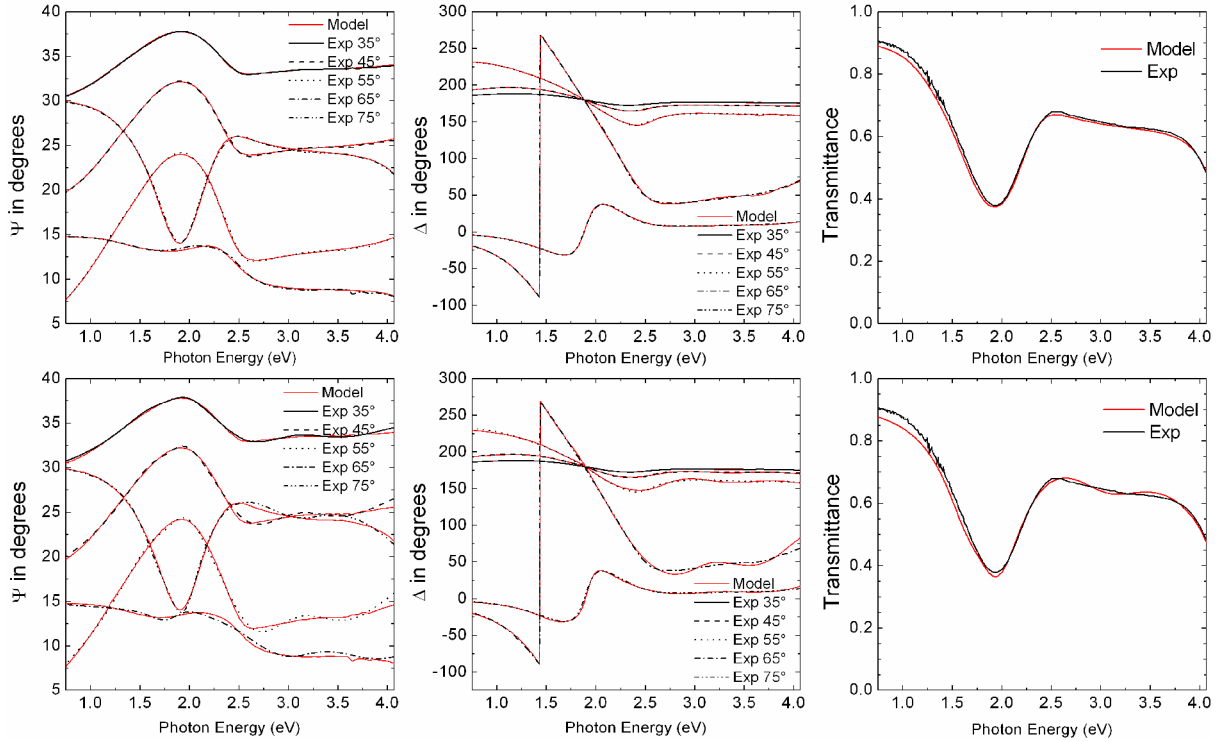


**Figure 7.1.** Experimental and model values of ellipsometric  $\Psi$ , ellipsometric  $\Delta$  and normal incidence transmittance  $T$  in the same point of the sample deposited at 120 °C with 7 nm mass thickness. Upper row corresponds to the model using Gaussian oscillators and lower row corresponds to the model using Lorentz oscillators.

In the first row the results of modelling with four Gaussian oscillators are shown, and in the second row there are modelling results with four Lorentz oscillators. Fitting with Gaussian oscillators gives better result ( $MSE_{\text{Gaussian}} = 2.3$ ;  $MSE_{\text{Lorentz}} = 5.6$ ).

The imaginary part  $\varepsilon_2(E)$  of the dielectric function for this sample, obtained from best fit using four Gaussian oscillators for parameterization (oscillator 1 for main LSP resonance, oscillator 2 and oscillator 3 to account for interband transitions of gold and oscillator 4 for inhomogeneous broadening of LSP resonance) is shown in Figure 7.2. The optimal values of the parameters obtained in this example are presented in Table 7.1.

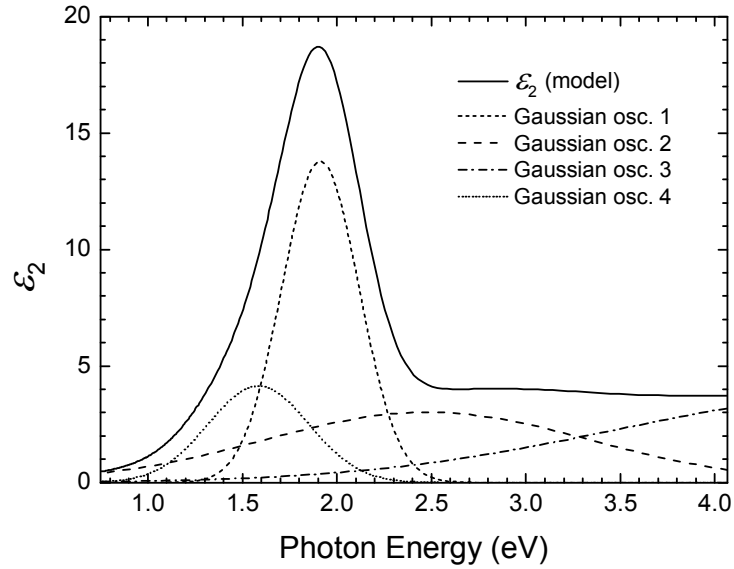


**Figure 7.2** The imaginary part  $\varepsilon_2(E)$  of the dielectric function for the sample with 7 nm mass thickness deposited at 120 °C (full bold line) obtained with fit using four Gaussian oscillators for parameterization (oscillator 1 for main LSP resonance, oscillator 2 and oscillator 3 to account for interband transitions of gold, and oscillator 4 for inhomogeneous broadening of LSP resonance). The optimal values of the parameters obtained in this example are shown in Table 7.1.

**Table 7.1** The optimal values of the parameters obtained for the sample with 7 nm mass thickness deposited at 120 °C.

Fit parameter	Value			
Effective layer thickness $d_{eff}$ (nm)	$7.70 \pm 0.07$			
	Oscillator 1	Oscillator 2	Oscillator 3	Oscillator 4
Oscillator centre energy $E_n$ (eV)	$1.921 \pm 0.002$	$2.48 \pm 0.06$	$4.83 \pm 0.09$	$1.58 \pm 0.02$
Oscillator amplitude $A_n$	$14.0 \pm 0.3$	$3.0 \pm 0.5$	$3.74 \pm 0.07$	$4.1 \pm 0.2$
Broadening parameter $B_n$ (eV)	$0.481 \pm 0.003$	$2.03 \pm 0.08$	$3.2 \pm 0.5$	$0.63 \pm 0.02$
$\varepsilon_\infty$	$2.21 \pm 0.07$			
Number of backside reflections	$2.3 \pm 0.1$			
MSE	2.3			

By using Lorentz oscillators we either got good numerical fit with non-physical solution (negligible effective layer thickness) or lesser fit than using Gaussian oscillators ( $MSE$  larger by factor of 2 or more). Combinations of different oscillators (Lorentz/Gaussian) for LSP resonance and interband transitions have been also tried with similar outcome (either non-physical solution or higher  $MSE$ ). Fitting with Gaussian oscillators was always better than with Lorentz oscillators although the same number of parameters was used: in all the cases, with Gaussian oscillators we got a good fit from numerical and physical point of view. Although the LSP resonance of isolated spherical gold nanoparticle may have Lorentz line shape [101], we have a distribution of LSP resonances of individual nanoparticles due to disorder, size and shape distribution. Gaussian line shape accommodates this distribution well because a convolution of many Lorentz oscillators results in a Gaussian.

The results of modelling, i.e. complex dielectric function and effective layer thickness for all measured samples are shown in Figure 7.3. The first column presents the samples with 3 nm deposited mass thickness, the second with 7 nm and the third with 12 nm. The first row presents the samples deposited at 25 °C, the second at 120 °C and the third at 215 °C. The number of oscillators used and  $MSE$  are shown in Table 7.2. In some cases more than one Gaussian oscillator is needed to describe LSP resonance because of the inhomogeneous line broadening of resonance [74].

**Table 7.2** The number of oscillators used for fitting data and corresponding  $MSE$  for all the measured samples.

<b>Mass thickness</b>	3 nm	7 nm	12 nm
<b>Substrate temperature</b>			
25 °C	4 × Gaussian $MSE = 2.4$	4 × Gaussian $MSE = 2.7$	5 × Gaussian 1 × Drude $MSE = 1.6$
120 °C	3 × Gaussian $MSE = 1.2$	4 × Gaussian $MSE = 2.3$	4 × Gaussian $MSE = 3.3$
215 °C	3 × Gaussian $MSE = 1.6$	3 × Gaussian $MSE = 3.4$	4 × Gaussian $MSE = 4.5$

The results of optical characterization shown in Figure 7.3 give valuable information about gold MIFs. We can follow the behaviour of LSP resonance with substrate temperature during deposition and different mass thickness by looking at imaginary part of dielectric response function  $\epsilon_2$ . Two main effects occur: i) red shift, broadening and intensity increase of LSP resonance peak with deposited mass thickness and ii) there is a blue shift and narrowing of LSP resonance peak with substrate temperature increase.

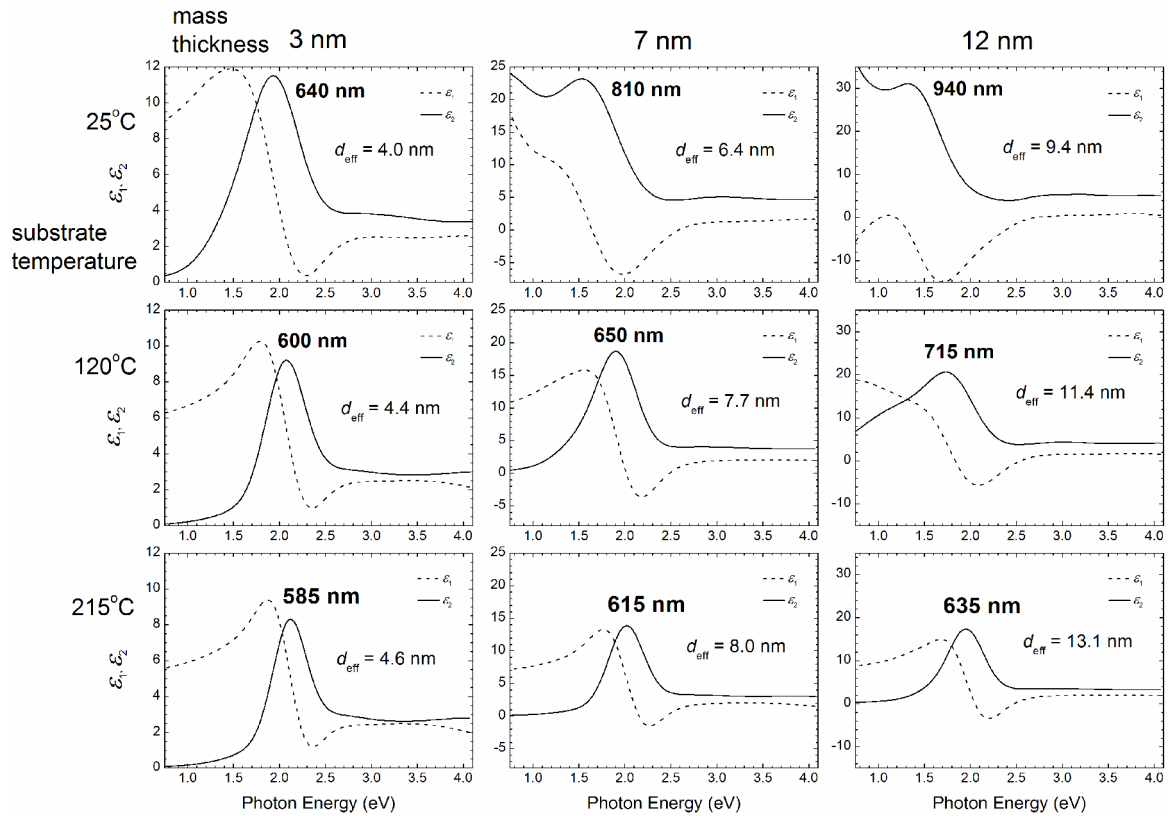


**Figure 7.3** Complex dielectric function and effective layer thickness for all measured samples in case of three deposition temperatures: 25 °C, 120 °C and 215 °C (presented in rows from top to the bottom) and for mass thickness of 3 nm, 7 nm and 12 nm (presented in columns from left to right).

These trends can be explained in terms of variations of particle size and shape for different amount of deposited material or substrate temperature [32, 96, 102]. Absorption at higher energies, to the right of LSP resonance, is attributed to the interband transitions of gold. Samples with 7 nm and 12 nm mass thickness prepared at room temperature and 12 nm sample made at substrate temperature of 120 °C show absorption at low energies (in infrared) typical for Drude (metal like) behaviour. This is an indication of percolation of gold nanoparticles [74, 103].

## 7.2. Structural characterisation of gold MIFs

Structural characterization of gold MIFs was done using atomic force microscopy and grazing-incidence small-angle X-ray scattering with an aim to explore the relationship between optical and structural properties.

### 7.2.1. Atomic force microscopy of gold MIFs

First information about structural properties of gold MIFs samples was obtained by AFM measurements. Figure 7.4 presents AFM micrographs of the samples.

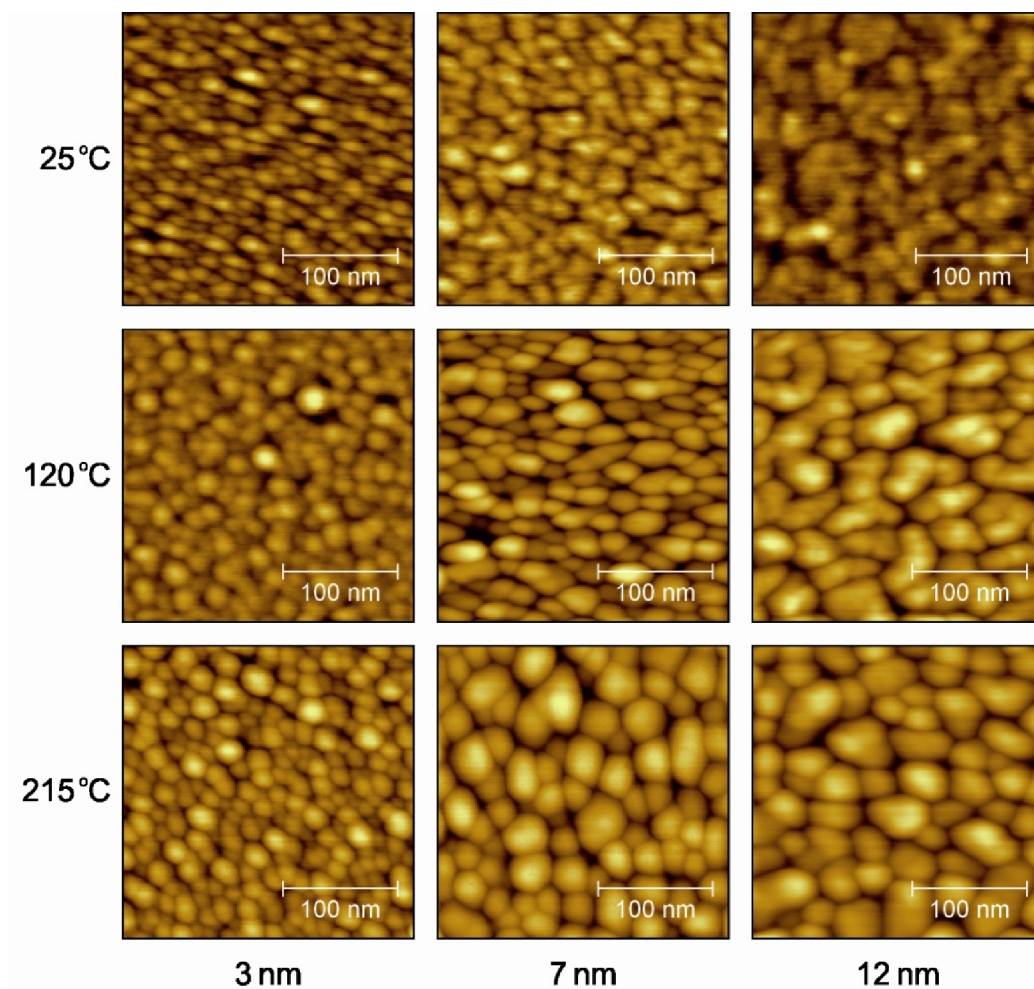


**Figure 7.4** AFM micrographs of gold MIF samples in case of three deposition temperatures; 25 °C, 120 °C and 215 °C (presented in rows from top to the bottom) and for deposition thicknesses of 3 nm, 7 nm and 12 nm (presented in columns from left to right).



As expected, according to Volmer-Weber mechanism of growth of ultrathin gold layers, supported nanoparticles of gold were formed [49].

It can be observed that the lateral size of the islands shows an increase along with the increase of deposition thickness, as well as with the substrate temperature. In the graph of 12 nm mass thickness sample deposited at 120 °C qualitative feature of percolation effect can clearly be observed where several particles join to make larger connected areas/clusters. This percolation effect is more pronounced in the case of low substrate temperatures with larger mass thickness of gold deposited – for 7 nm and 12 nm mass thickness samples deposited at 25 °C and 120 °C. Described qualitative evidence of percolation from AFM is in complete agreement with results of optical analysis and modelling of Drude-like behaviour in infrared. Very small particle sizes, comparable with the radius of AFM tip, resulted in limited possibility of extracting quantitative information obtained from AFM measurements (problem of convolution of particle shape and tip shape, and possible artefacts). Therefore, only average centre-to-centre particle distances between nearest neighbours (interparticle distances  $D$ ) and corresponding standard deviations  $\sigma_D$  were calculated and presented for all the samples without percolation in Table 7.3.

**Table 7.3** The results of AFM measurements of gold MIFs samples.

<b>Mass thickness</b>	3 nm		7 nm		12 nm	
<b>Substrate temperature</b>	$D / \text{nm}$	$\sigma_D / \text{nm}$	$D / \text{nm}$	$\sigma_D / \text{nm}$	$D / \text{nm}$	$\sigma_D / \text{nm}$
25 °C	16.3	4.0	percolation	–	percolation	–
120 °C	18.6	4.0	23.3	5.7	percolation	–
215 °C	19.0	3.4	31.0	6.2	35.1	8.8

### 7.2.2. GISAXS of gold MIFs

For the purpose of detailed analysis of gold MIFs' structural properties with the aim of determining correlation with optical properties determined from VASE and to complement information obtained with AFM measurements, GISAXS studies have been done. Figure 7.5 depicts 2D GISAXS scattering patterns of the samples.

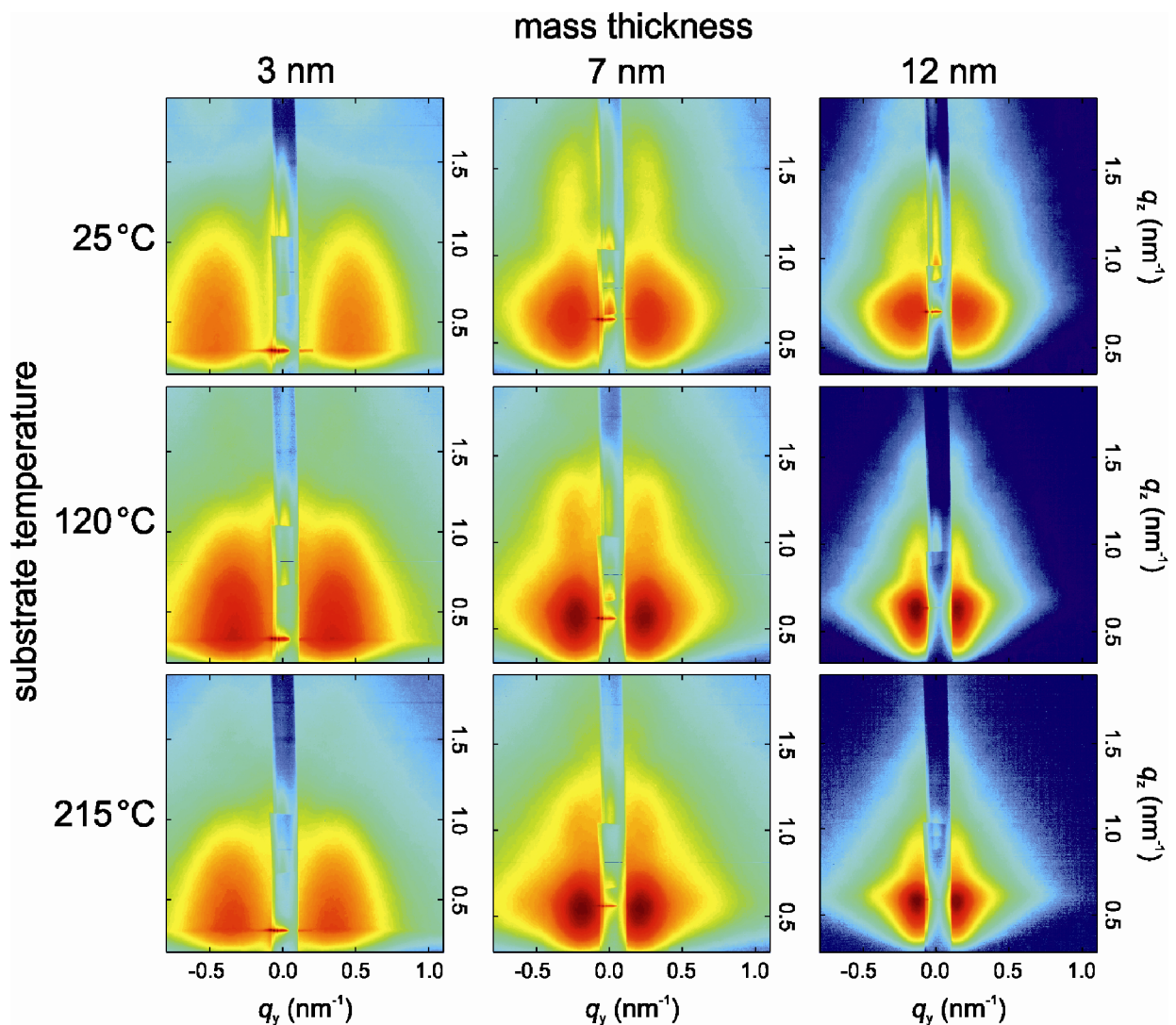


**Figure 7.5** The experimental 2D GISAXS scattering patterns for gold MIFs samples. The first column presents samples with 3 nm deposited mass thickness, the second with 7 nm and the third with 12 nm. The first row presents samples deposited at 25 °C, the second at 120 °C and the third at 215 °C. The intensity is represented with logarithmic colour scale.

In all scattering patterns in Figure 7.5, well-defined areas of maximal intensities at both sides of the beam stop could be observed. The scattered intensity concentrates more towards the origin of the reciprocal space as the deposited gold thickness increases (Figure 7.5 from left to the right), with an increase in the deposition temperature as well (Figure 7.5 from top to the bottom). This suggests that nanoparticle sizes grow in all real-space directions as it will be confirmed in further analysis. In each pattern in Figure 7.5 two maxima situated parallel to the  $q_y$  axis are separated by the partly seen (partly screened by the beam stop) specular rod at  $q_y = 0 \text{ nm}^{-1}$ . This interference effect arises because there is a preferential interparticle distance ( $D$ ) between nanoparticles [93].

The first step in gold nanoparticle size analysis was performed using a simplified approach (explained already in the analysis of structural properties of silver MIFs) where Guinier's approximation was applied. Further step included quantitative analysis in which the program IsGISAXS was used [91, 95]. The scattering calculations were done in Distorted Wave Born Approximation (DWBA) on gradient layer [86] (see Appendix). Calculation of the particle-particle correlations was in the framework of Local Monodisperse Approximation (LMA) [86]. For the model particle shapes, truncated spherical and truncated spheroid particles were chosen (Figure 7.6) with uncoupled size distributions parallel and perpendicular to the surface (log-normal and Gaussian, respectively).

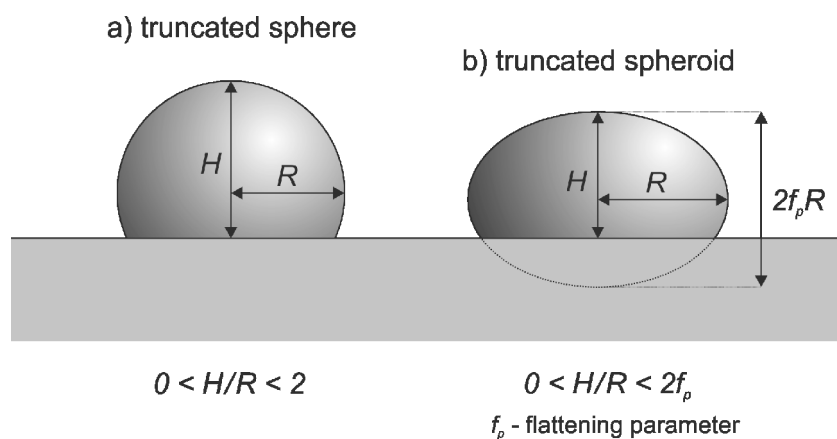


**Figure 7.6** Schematic representation of nanoparticle morphology with explanation of parameters used in GISAXS analysis.

In simultaneous fitting of GISAXS intensity profiles  $q_y$  and  $q_z$  crossing at maximum of intensity position  $q_m$ , fit parameters were average particle radius  $R$ , height  $H$  and interparticle distance  $D$  with corresponding widths of distributions  $\sigma_R$ ,  $\sigma_H$  and  $\sigma_D$ . For two samples, flattening parameter  $f_p$  was also introduced (Figure 7.6). For starting parameter values in fit procedure, numbers obtained from simplified approach with Guinier's approximation and "Bragg" law were used. In Figure 7.7 an example of GISAXS analysis is presented.  $q_y$  and  $q_z$  cuts (1D cuts of experimental 2D GISAXS intensity pattern parallel and perpendicular to the sample surface at the position of intensity maximum) together with fitting results are shown for the sample with 3 nm mass thickness of gold deposited at 25 °C, 120 °C and 215 °C (see corresponding 2D GISAXS patterns in Figure 7.5).

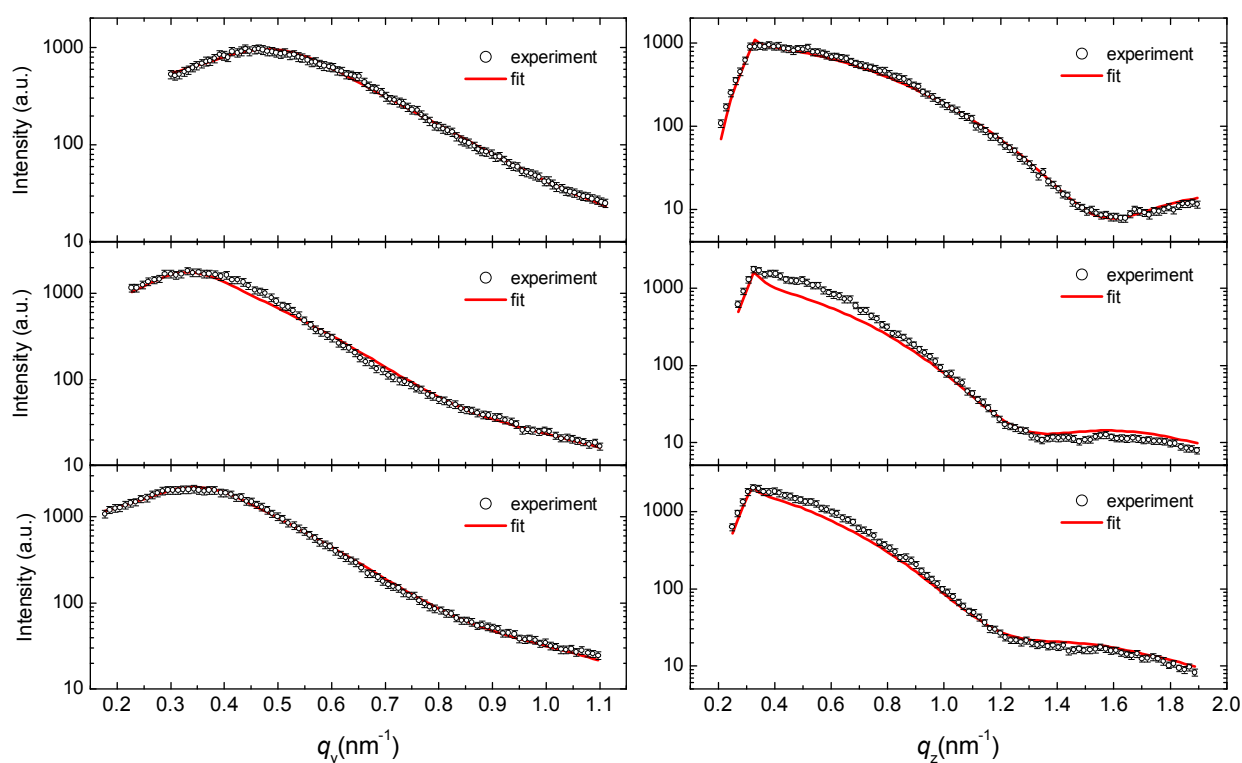


**Figure 7.7** Parallel (left) and perpendicular (right) linear cuts through the intensity maximum of experimental GISAXS pattern for the sample with 3 nm mass thickness deposited at 25 °C, 120 °C and 215 °C. The experimental points are represented by circles with error bars and lines correspond to the simultaneous best fits. Resulting values for average truncated spherical particle radius, height and interparticle distances with dispersions of these values are shown in Table 7.4.

Rich morphological information obtained by GISAXS analysis of gold MIF samples is summarized in Table 7.4 together with the results of optical characterization obtained by VASE. For the samples with percolation, described GISAXS model does not give reasonable physical results and for the purpose of completeness of analysis, simple Guinier's approximation for  $R$  and  $H$ , and "Bragg law" for  $D$  values are shown in Table 7.4. Overall, the obtained average vertical and horizontal nanoparticle sizes and interparticle distances clearly show the trend of growing with both the deposition thickness and deposition temperature.

**Table 7.4** Summarized characterisation results obtained by three methods (VASE, GISAXS and AFM) for all measured gold MIF samples.  $\lambda_{\text{peak}}$  is the position of the  $\varepsilon_2(E_{\text{photon}})$  peak maximum,  $\Delta\lambda_{\text{FWHM}}$  is the respective peak width (full width at half maximum). For AFM,  $D$  represents average interparticle distance with standard deviation  $\sigma_D$ . For GISAXS,  $H$  is average vertical size (height) of nanoparticles,  $R$  is their average horizontal (lateral) radius and  $D$  is average interparticle distance ( $\sigma_H$ ,  $\sigma_R$  and  $\sigma_D$  are widths of distributions of corresponding values). All the values are in nanometers (nm) except flattening parameter  $f_p$  which is a number.

Au samples													
		Methods											
		VASE			AFM			GISAXS					
		$\lambda_{\text{peak}}/\text{nm}$	$\Delta\lambda_{\text{FWHM}}/\text{nm}$	$d_{\text{ef}}/\text{nm}$	$D/\text{nm}$	$\sigma_D/\text{nm}$	$R/\text{nm}$	$\sigma_R/\text{nm}$	$H/\text{nm}$	$\sigma_H/\text{nm}$	$D/\text{nm}$	$\sigma_D/\text{nm}$	$f_p$
3 nm	25 °C	640	290	4.0	16.3	4.0	3.9 ± 0.6	1.5 ± 0.9	5.1 ± 0.9	0.5 ± 0.3	10 ± 3	4 ± 2	–
3 nm	120 °C	600	175	4.4	18.6	4.0	4.7 ± 0.5	1.6 ± 0.6	6.7 ± 0.9	0.8 ± 0.5	15 ± 6	6 ± 4	–
3 nm	215 °C	585	145	4.6	19.0	3.4	5 ± 1	2 ± 2	7 ± 2	0.5 ± 0.3	14 ± 7	6 ± 3	–
7 nm	25 °C	810	380 <sup>a</sup>	6.4	percolation	–	6.9 <sup>b</sup>	– <sup>b</sup>	9.8 <sup>b</sup>	– <sup>b</sup>	25.1 <sup>b</sup>	– <sup>b</sup>	–
7 nm	120 °C	650	225	7.7	23.3	5.7	10.8	4.2	7.6	4.6	19	5	0.6
7 nm	215 °C	615	155	8.0	31.0	6.2	9.6	5.3	9.6	3.3	21	9	–
12 nm	25 °C	940	460 <sup>a</sup>	9.4	percolation	–	7.8 <sup>b</sup>	– <sup>b</sup>	11.6 <sup>b</sup>	– <sup>b</sup>	36.6 <sup>b</sup>	– <sup>b</sup>	–
12 nm	120 °C	715	250 <sup>a</sup>	11.4	percolation	–	13.8 <sup>b</sup>	– <sup>b</sup>	16.4 <sup>b</sup>	– <sup>b</sup>	45.3 <sup>b</sup>	– <sup>b</sup>	–
12 nm	215 °C	635	175	13.1	35.1	8.8	12 ± 4	–	15.6	–	30	13	0.7

<sup>a</sup>Because of percolation and Drude-like infrared absorption shoulder on the left side of the LSP resonance peaks for these samples, the value of half-width on the right side of peak, at half maximum, multiplied by 2 is shown.

<sup>b</sup>For these samples, results of simplified Guinier's approximation for GISAXS analysis are shown

## 8. Gold metal island films in dielectric multilayers

In this part of the research we found particularly interesting the influence of surrounding media that change the LSP resonance properties of embedded MIFs compared with MIFs on bare substrate. Understanding of the surrounding media influence on plasmonic oscillations is of crucial importance for the further multilayer design containing metal island films.

At first we have studied the plasmon resonances and optical characteristics of gold island films embedded between SiO<sub>2</sub> and/or TiO<sub>2</sub> dielectric films each of 100 nm thickness. The effects of gold islands size, shape and arrangement on the optical properties have been studied earlier in details with bare silver and gold island films [32]. In the second phase, we used the obtained data for design of optical multilayers containing thin metal island films.

### 8.1. Optical characterization of embedded gold MIFs

The influence of a dielectric surrounding on the optical properties of MIFs may be seen in the series of figures that will be presented; the optical loss spectra of gold MIFs are shown for MIFs on bare BK7 substrate and for MIFs in different combinations of SiO<sub>2</sub>/TiO<sub>2</sub> layers above/below.

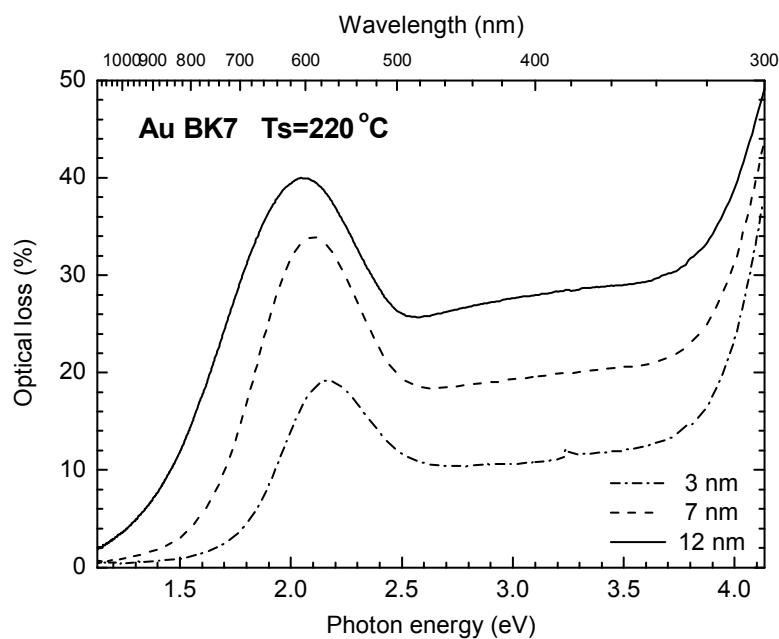


**Figure 8.1** The optical loss spectrum of gold MIFs on bare BK7 substrate.

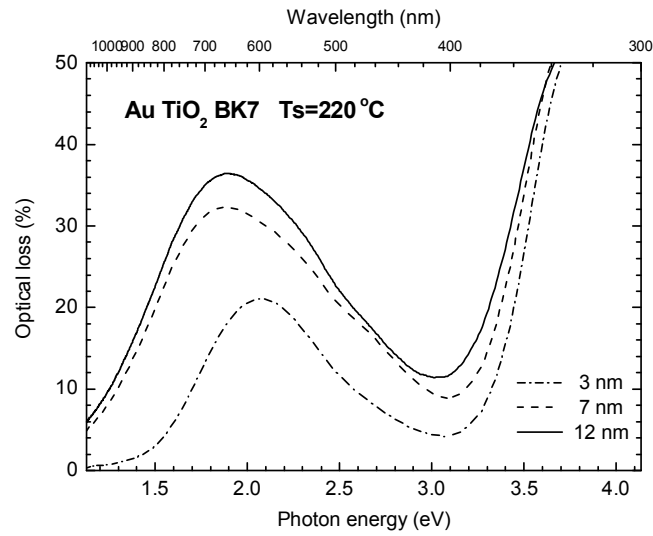


**Figure 8.2** The optical loss spectrum of gold MIFs on 100 nm  $\text{TiO}_2$  layer on BK7 substrate.

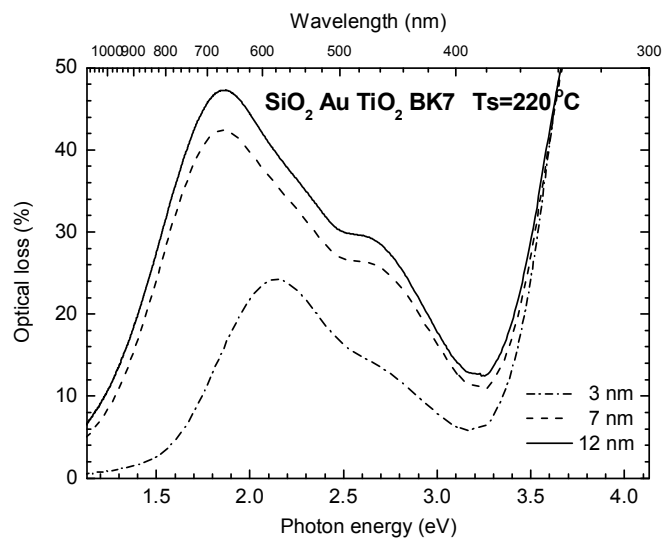


**Figure 8.3** The optical loss spectrum of gold MIFs embedded between  $\text{SiO}_2$  and  $\text{TiO}_2$  layer.

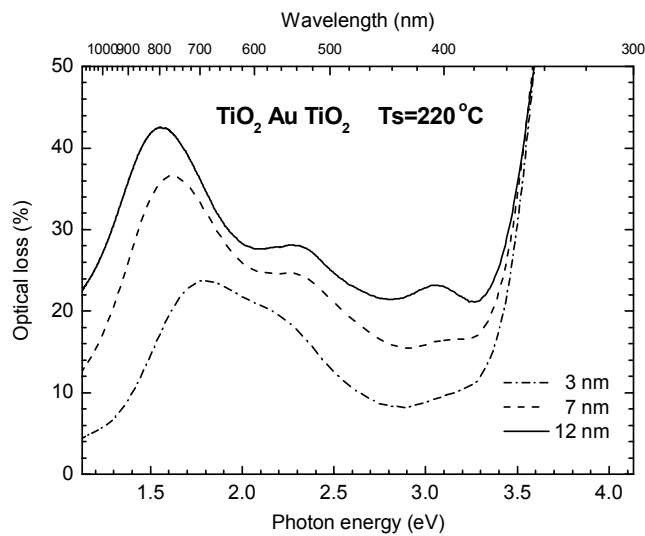


**Figure 8.4** The optical loss spectrum of gold MIFs embedded between two 100 nm  $\text{TiO}_2$  layers.

More detailed optical characterisation was done using spectroscopic ellipsometry. At first bare BK7 glass substrates and SiO<sub>2</sub> and TiO<sub>2</sub> films on BK7 substrates were measured and characterized. The yielded optical parameters  $n$  and  $k$  were used in subsequent analysis. Gold island films on bare BK7 substrate were prepared and analyzed using an efficient procedure for optical characterization of gold island films that we developed and described in previous chapter [104], where gold island films were modelled as homogeneous layers with effective optical constants and thickness. For modelling the dispersion of optical constants, multiple oscillator approach with Gaussian oscillators was used. The values of parameters obtained from characterization of gold island film on BK7 glass were used as a starting point for analysis of gold films embedded between dielectric layers and then refined. For example, experimental data for the sample with TiO<sub>2</sub>/Au/TiO<sub>2</sub> assembly together with results of fitting of spectroscopic ellipsometry and transmittance are presented in Figure 8.5. Transmittance measurements at the same point of the sample were needed to achieve uniqueness of fit with respect to the effective layer thickness [105].

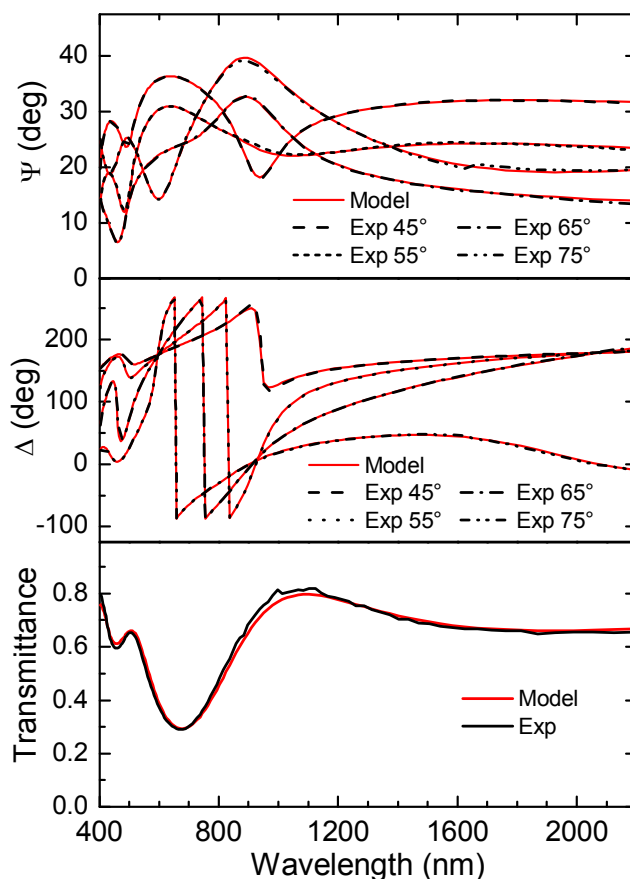


**Figure 8.5** Experimental and modelled values of ellipsometric  $\Psi$  and  $\Delta$  functions and normal incidence transmission measured at the same point of the sample with TiO<sub>2</sub>/Au/TiO<sub>2</sub> assembly.



In the Figure 8.6 all four complex refractive index dispersions of the studied gold films are presented. For all the samples, results show strong extinction in the visible spectral range that is associated with the localized surface plasmon resonance of the islands. Additional absorption was observed in the near UV spectral range, which can be associated with the electronic interband transition of gold. The plasmon frequency is shifted, depending on the embedding media. The plasmon resonance is red shifted for gold island films embedded in media with higher refractive index which is in agreement with earlier observations [30].

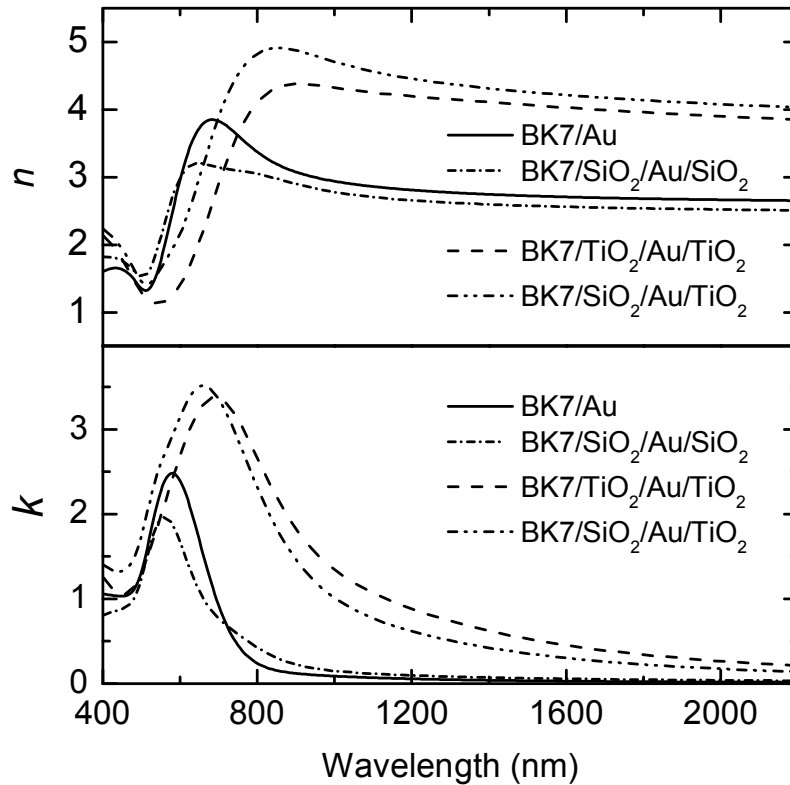


**Figure 8.6** Refractive indices of gold island films in various assemblies: BK7/Au, BK7/SiO<sub>2</sub>/Au/SiO<sub>2</sub>, BK7/SiO<sub>2</sub>/Au/TiO<sub>2</sub> and BK7/TiO<sub>2</sub>/Au/TiO<sub>2</sub>

The dielectric layers were considered to have fixed values of  $n$  and  $k$  in a standard multilayer design procedure. On the contrary, the gold island films had to be characterized from the same environment in which they will be within an optical multilayer. Their  $n$  and  $k$  cannot be used from the characterization of a single gold island film on the substrate as evident in the Figure 8.6. It's up to conclusion that effective optical constants  $n$  and  $k$  of gold island films depend strongly on dielectric environment. Thus, different values of optical constants, corresponding to particular dielectric environment, have to be taken for the design of optical multilayers.

## 8.2. Design of multilayer reflectors with gold MIFs

We designed various multilayer reflectors based on the enhancement of reflectance of silver in the region of 400 nm – 700 nm. Actually, we started with improvement of one of earlier designs done by P. Heger et al. [106], where they used a silver island film as a part of the multilayer on the top of a thicker silver film with the similar purpose. The optical characterization described in previous section yielded the data required for further design of optical multilayers with embedded gold island films.

Three various designs were studied: blue reflector, white reflector and yellow reflector. The used target functions are listed as follows (R denotes reflectance):

Blue reflector:  $R = 1$  for 400 nm – 580 nm and  
 $R = 0$  for 600 nm – 900 nm

White reflector:  $R = 1$  for 420 nm – 680 nm

Yellow reflector:  $R = 0$  for 380 nm – 500 nm,  
 $R = 1$  for 520 nm – 600 nm and  
 $R = 0$  for 620 nm – 900 nm

The idea was to use the surface plasmon properties of gold island films. In the given wavelength range, its high absorbance of refractive index indicated a potential to get good results for high reflectance.

For design the TFCalc<sup>TM</sup> software was used [107]. In the design several approaches were tried. Basically we started by creating a reflector on the top of a silver film with an idea to get induced resonance absorption for the maximum reflectance. Therefore, in the process of optimization we had to fix groups containing gold island film in order to keep surrounding media. We started with a 500 nm thick single layer of SiO<sub>2</sub> and then applied needle optimization with the three material combinations plus SiO<sub>2</sub> and TiO<sub>2</sub> [108-110]. Target functions were varied in order to get blue, yellow and white reflectors with high luminosity. The obtained results for blue and white reflectors are presented in the Figure 8.7. The corresponding designs are presented in Table 8.1 together with the obtained luminosities.

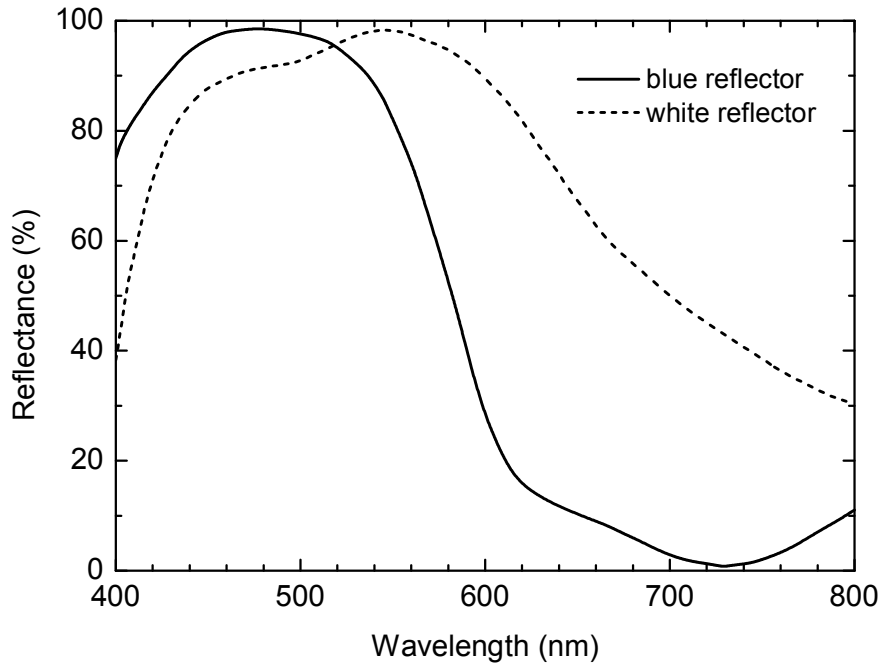


**Figure 8.7** The reflectance of the blue and white reflectors

**Table 8.1** Design details and luminosities of the blue and white reflectors

	<b>Blue reflector</b>	<b>White reflector</b>
BK7		
Ag	100.00 nm	100.00 nm
SiO <sub>2</sub>	41.26 nm	68.09 nm
TiO <sub>2</sub>	53.78 nm	57.06 nm
Au	9.50 nm	9.50 nm
SiO <sub>2</sub>	64.66 nm	66.20 nm
TiO <sub>2</sub>	59.59 nm	124.76 nm
SiO <sub>2</sub>	211.33 nm	167.74 nm
Air		
Luminosity:	66.7%	93.0%

The same design approach did not yield satisfactory results for the yellow reflector and, therefore, a different design strategy was applied. It turned out that multilayers based on the enhanced reflectivity of compact silver films were not selective enough and systems without silver layers on the substrate made far better designs. The details are presented in the Figure 8.8 and the corresponding design is presented in Table 8.2.

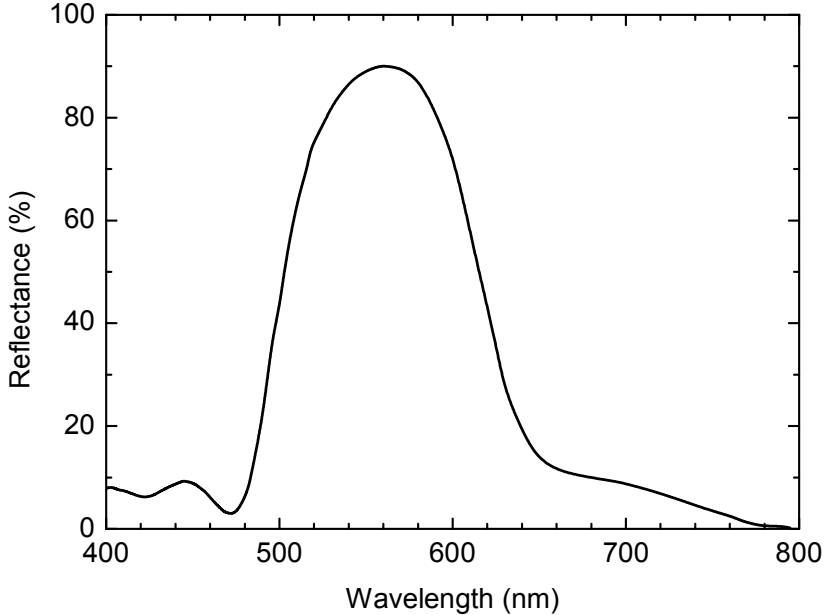


**Figure 8.8** Reflectance of the yellow reflector

**Table 8.2** Design details and luminosity of the yellow reflector

BK7	
TiO <sub>2</sub>	71.21 nm
Au	9.50 nm
SiO <sub>2</sub>	87.53 nm
TiO <sub>2</sub>	68.33 nm
Au	9.50 nm
SiO <sub>2</sub>	65.54 nm
TiO <sub>2</sub>	211.33 nm
Au	9.50 nm
SiO <sub>2</sub>	124.55 nm
TiO <sub>2</sub>	39.31 nm
Au	9.50 nm
TiO <sub>2</sub>	122.34 nm
Air	

Luminosity: 71.6%

## 9. Conclusions

Metal island films of silver, copper and gold were fabricated by electron beam evaporation. The tailoring of optical and structural properties of the samples was done by changing two experimental parameters: mass thickness of deposited material and substrate temperature.

The formation of metal islands on the substrates was confirmed by AFM and GISAXS. The first trend of the islands morphology dependence (deduced from AFM and GISAXS) is an increase of the interparticle distance and of all island dimensions with an increase of deposited mass thickness. This could be explained by greater amount of deposited material available for particle nucleation. The second trend is an increase of particle size and interparticle distance as the deposition temperature increases. This is explained by the higher energy available to the silver atoms arriving to a hotter substrate.

The optical properties of the samples were investigated using spectrophotometry and variable angle spectroscopic ellipsometry. The existence of the LSP resonance was identified in the optical spectra and the change of LSP resonance position and width with the change of deposition mass thickness and substrate temperature was quantified. The absorption in visible-to-UV range for copper and gold, and in UV for silver was associated with interband transitions of these metals. Metal-like behaviour of dielectric functions, at low frequencies for samples at low substrate temperatures and high mass thickness, was observed and attributed to appearance of percolation.

Efficient procedure for optical characterization of MIFs using variable angle spectroscopic ellipsometry was developed. This procedure is based on modelling the dispersion of effective optical constants using a multiple oscillator approach. As a result, it gives effective optical constants which are Kramers-Kronig consistent over the whole frequency range examined, and corresponding effective layer thickness. Although the Lorentz oscillators are usually employed to represent LSP resonance [74], it appears that Gaussian oscillators are more flexible and provide better fits to experimental data [104]. The modelling of interband transitions of noble metals and Drude absorption in NIR is also successfully performed in the multiple oscillator model previously described.

A broadening and red shift of the LSP peak characterize the evolution of the optical properties of MIFs with the amount of deposited noble metal. Such behaviour could be qualitatively explained by modelling the metal MIF-SiO<sub>2</sub> layer as a composite film, which shows that, when the concentration of metal increases in the composite film, the LSP resonance becomes broader and red shifted [70, 97, 98]. Regarding the evolution of LSP with temperature, a blue shift and a narrowing of the LSP resonance is observed. It is attributed to the changes in size and shape of islands and interparticle distance. The multiple oscillator model successfully reproduced all the trends of behaviour of LSP resonance.

The research of the gold MIFs on bare BK7 substrates gave a basis for describing the optical properties of gold MIFs embedded between SiO<sub>2</sub> and TiO<sub>2</sub> layers. Plasmonic properties of gold MIFs were characterized for various combinations of embedding media and used for design of reflectors.

The used design strategies resulted in blue, white and yellow reflectors based on multilayers containing gold MIFs. Two of them were spectrally selected enhancements of silver film reflectance and the yellow reflector was designed by only using gold MIFs, SiO<sub>2</sub> and TiO<sub>2</sub> films [44].

If one compares the results with those given in the paper [106] it is obvious that use of either gold island films or silver island films can produce very similar results. To produce this filters, one has to maintain constant deposition conditions and fixed gold island film thickness. The influence of gold island film environment, SiO<sub>2</sub> and TiO<sub>2</sub>, in this study had to be taken into consideration, because those neighbouring materials drastically change optical behaviour of islands.

Gold MIFs show interesting potential for the future considerations in thin film optics. Multilayers with high absorbance and no reflectance are one of them. Well controlled production, in which the influence of gold island film environment is properly taken into consideration, is one of the basic prerequisites. Nevertheless, gold island films are on the right way to find their use in interference coatings.

## Appendix: Different approaches in GISAXS analysis

In this appendix various approximate approaches to GISAXS analysis are presented which were used in the study of gold island films.

When a beam of collimated X-rays comes to a perfectly flat surface, all the outgoing intensity is concentrated in the reflected beam. The off-specular scattering appears when any type of surface roughness or scattering density is present on the surface. In our case, the roughness comes from presence of small particles or islands on the surface, where each object is characterised by its position on the substrate  $\mathbf{R}^i$  and its shape function  $S^i(\mathbf{r})$ , equal to one inside the object and to zero outside. The scattering density (electronic density in the case of X-rays) is given by a convolution product

$$\rho(\mathbf{r}) = \rho_0 \sum_i S^i(\mathbf{r}) \otimes \delta(\mathbf{r} - \mathbf{R}^i), \quad (1.1)$$

where  $\rho_0$  is the mean electronic density of the islands.

X-ray beam is scattered from the supported small particles due to changes in electronic density described by (1.1), with scattering wave vector  $\mathbf{q}$  which equals  $\mathbf{q} = \mathbf{k}_f - \mathbf{k}_i$ . ( $\mathbf{k}_i$  is the incident X-ray beam wave vector and  $\mathbf{k}_f$  is the scattered X-ray beam with wave vector). The scattering wave vector magnitude  $q = 4\pi \sin(\theta) / \lambda$ , where  $2\theta$  is the angle between  $\mathbf{k}_f$  and  $\mathbf{k}_i$ .

The scattering cross section is defined by

$$\frac{d\Sigma}{d\Omega}(q) = \frac{N}{NI_0 \Delta\Omega}, \quad (1.2)$$

with  $N$  the number of photons scattered into the solid angle  $\Delta\Omega$  around  $(2\theta_f, \alpha_f)$ ,  $I_0$  the flux of incident photons and  $N$  the total number of scattering centres (islands). The scattering intensity  $I(q)$  is proportional to the scattering cross section.

$$I(q) = \frac{1}{N} \sum_i \sum_j F^i(q) F^{j*}(q) \exp(-iq(R^i - R^j)), \quad (1.3)$$

where  $S^i$  is the shape function and  $R^i$  is the position of particle indexed with  $i$ .

Small angle scattering is the sum of a coherent scattering term and an incoherent scattering term. The incoherent scattering term is present when the size distribution of the nanostructures is not monodisperse. The coherent term is the product of the square modulus of the mean nanostructure form factor  $F(q)$  (which is the Fourier transform of the nanostructure shape) with the interference function  $S(q)$  (which is the Fourier transform of the pair correlation function of the nanostructures position described later). The incoherent scattering is very difficult to evaluate analytically in the general case. Therefore, two limit cases are usually used: (i) the Decoupling Approximation (DA), assuming no nanostructure correlations, and (ii) the Local Monodisperse Approximation (LMA), assuming full correlation between nanostructure sizes at a scale corresponding to the coherence length of the X-ray beam.



## Statistical approximations for scattering intensity

Usual statistical approximations for scattering intensity

$$I(q) = \frac{1}{N} \sum_i \sum_j F^i(q) F^{j*}(q) \exp(-iq(R^i - R^j)) \quad (1.4)$$

depend on particular morphology of particles in different cases:

a) Size, shape and position completely uncorrelated → **Decoupling Approximation (DA)**



$$I(q) = I_d(q) + \left| \langle F(q) \rangle_\alpha \right|^2 S(q), \quad I_d(q) = \left\langle |F(q)|^2 \right\rangle_\alpha - \left| \langle F(q) \rangle_\alpha \right|^2, \quad (1.5)$$

b) Locally identical particles → **Local Monodisperse Approximation (LMA)**



$$I(q) = \left\langle |F(q)| \right\rangle_\alpha^2 S(q), \quad (1.6)$$

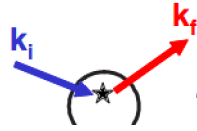
c) Particle distance partially depends on size → **Size-Spacing Correlation Approximation (SSCA)**



## Form factor $F(q)$

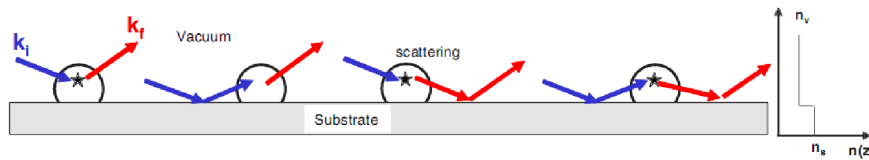
Form factor  $F(q)$  may be calculated within approximations of increasing complexity:

- a) Isolated particle: **Born Approximation (BA)**

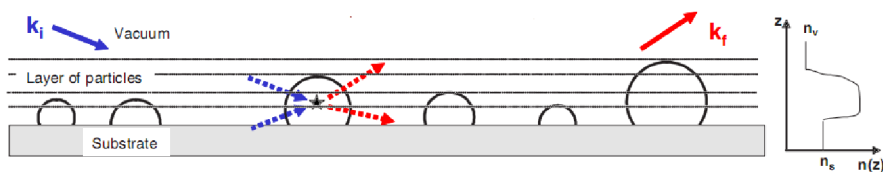


$$F_i(q) = \oint_{S_i} \exp(iqr) d^3r, \quad (1.7)$$

- b) Particle supported on a substrate: **Distorted Wave Born Approximation (DWBA)**



- c) Dense particle system supported on a substrate: **DWBA on gradient layer**



Several approaches were tried in the GISAXS analysis of metal island films in this research, but only the framework of DWBA on gradient layer with local monodisperse approximation gave appropriate results that are presented in the text.

## Interference function $S(q)$

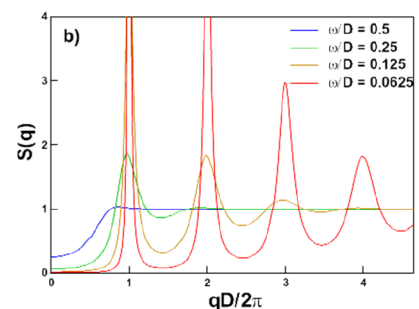
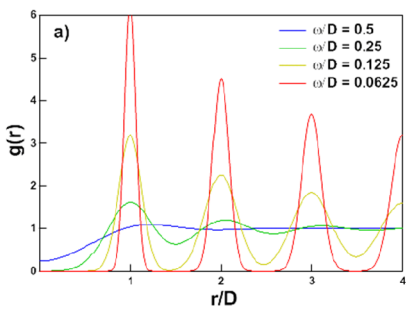
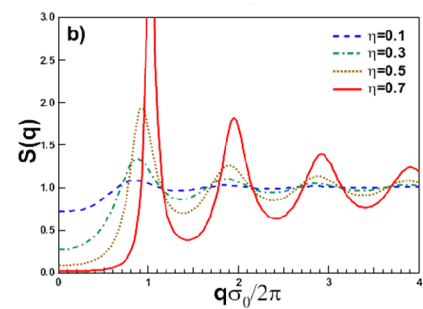
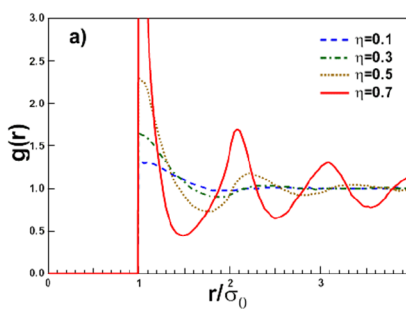
Let us assume that  $dP(\mathbf{r})$  is the number of particles at  $\mathbf{r}$ , knowing that a particle is present at origin. As for a completely random distribution, this value tends towards the surface per particle times the elementary surface area around  $\mathbf{r}$ , we define the pair correlation function  $g(\mathbf{r})$  as the departure from this mean value:

$$dP(\mathbf{r}) = \rho_s g(\mathbf{r}) d^2\mathbf{r} \quad (1.8)$$

with  $\rho_s$  the particle density per unit surface.

The interference function  $S(q)$  is the Fourier transform of partial pair correlation function  $g(r)$  and their corresponding relation is illustrated below for three characteristic cases of particle order:

### a) Ordered systems (lattice)



The para-crystal model was applied in the analysis of the gold MIFs samples in this thesis which is presented in section 7.2.2.

## References

1. F. E. Wagner, S. Haslbeck, L. Stievano, S. Calogero, Q. A. Pankhurst and K. P. Martinek: Before striking gold in gold-ruby glass, *Nature* **407** (6805), 691-692 (2000).
2. I. Freestone, N. Meeks, M. Sax and C. Higgitt: The Lycurgus Cup A Roman Nanotechnology, *Gold Bull* **40** (4), 270-277 (2007).
3. U. Leonhardt: Optical metamaterials: Invisibility cup, *Nat Photon* **1** (4), 207-208 (2007).
4. W. Cai, U. K. Chettiar, A. V. Kildishev and V. M. Shalaev: Optical cloaking with metamaterials, *Nat Photon* **1** (4), 224-227 (2007).
5. A. Sommerfeld: Ueber die Fortpflanzung elektrodynamischer Wellen längs eines Drahtes, *Annalen der Physik* **303** (2), 233-290 (1899).
6. J. Zenneck: Über die Fortpflanzung ebener elektromagnetischer Wellen längs einer ebenen Leiterfläche und ihre Beziehung zur drahtlosen Telegraphie, *Annalen der Physik* **328** (10), 846-866 (1907).
7. G. Mie: Beiträge zur Optik trüber Medien, speziell kolloidaler Metallösungen, *Annalen der Physik* **330** (3), 377-445 (1908).
8. W. Gotschy, K. Vonmetz, A. Leitner and F. R. Aussenegg: Optical dichroism of lithographically designed silver nanoparticle films, *Opt. Lett.* **21** (15), 1099-1101 (1996).
9. D. W. C. So and S. R. Seshadri: Metal-island-film polarizer, *J. Opt. Soc. Am. B* **14** (11), 2831-2841 (1997).
10. K. Baba, Y. Ohkuma, T. Yonezawa and M. Miyagi: Silver-based compound metal island films for write-once optical data-storage media, *Appl. Opt.* **40** (16), 2796-2804 (2001).

11. A. Hohenau, H. Ditlbacher, B. Lamprecht, J. R. Krenn, A. Leitner and F. R. Aussenegg: Electron beam lithography, a helpful tool for nanooptics, *Microelectron Eng* **83** (4-9), 1464-1467 (2006).
12. M. Lahav, A. Vaskevich and I. Rubinstein: Biological sensing using transmission surface plasmon resonance spectroscopy, *Langmuir* **20** (18), 7365-7367 (2004).
13. J. N. Anker, W. P. Hall, O. Lyandres, N. C. Shah, J. Zhao and R. P. Van Duyne: Biosensing with plasmonic nanosensors, *Nat Mater* **7** (6), 442-453 (2008).
14. A. Wokaun, J. G. Bergman, J. P. Heritage, A. M. Glass, P. F. Liao and D. H. Olson: Surface second-harmonic generation from metal island films and microlithographic structures, *Phys Rev B* **24** (2), 849 (1981).
15. K. Kneipp, Y. Wang, H. Kneipp, L. T. Perelman, I. Itzkan, R. R. Dasari and M. S. Feld: Single Molecule Detection Using Surface-Enhanced Raman Scattering (SERS), *Phys Rev Lett* **78** (9), 1667 (1997).
16. S. Nie and S. R. Emory: Probing single molecules and single nanoparticles by surface-enhanced Raman scattering, *Science* **275** (5303), 1102-1106 (1997).
17. A. Campion and P. Kambhampati: Surface-enhanced Raman scattering, *Chemical Society Reviews* **27** (4), 241-250 (1998).
18. Z. Q. Tian: Surface-enhanced Raman spectroscopy: advancements and applications, *J Raman Spectrosc* **36** (6-7), 466-470 (2005).
19. S. Pillai, K. R. Catchpole, T. Trupke and M. A. Green: Surface plasmon enhanced silicon solar cells, *Journal of Applied Physics* **101** (9), 093105-093108 (2007).
20. K. R. Catchpole and A. Polman: Plasmonic solar cells, *Opt. Express* **16** (26), 21793-21800 (2008).

21. M. Losurdo, M. M. Giangregorio, G. V. Bianco, A. Sacchetti, P. Capezzuto and G. Bruno: Enhanced absorption in Au nanoparticles/a-Si:H/c-Si heterojunction solar cells exploiting Au surface plasmon resonance, *Sol Energ Mat Sol C* **93** (10), 1749-1754 (2009).
22. H. A. Atwater and A. Polman: Plasmonics for improved photovoltaic devices, *Nat Mater* **9** (3), 205-213 (2010).
23. L. Escoubas, J.-J. Simon, P. Torchio, D. Duché, S. Vedraïne, W. Vervisch, J. Le Rouzo, F. Flory, G. Rivière, G. Yeabiyo and H. Derbal: Bringing some photonic structures for solar cells to the fore, *Appl. Opt.* **50** (9), C329-C339 (2011).
24. L. R. Hirsch, R. J. Stafford, J. A. Bankson, S. R. Sershen, B. Rivera, R. E. Price, J. D. Hazle, N. J. Halas and J. L. West: Nanoshell-mediated near-infrared thermal therapy of tumors under magnetic resonance guidance, *P Natl Acad Sci USA* **100** (23), 13549-13554 (2003).
25. P. K. Jain, I. H. El-Sayed and M. A. El-Sayed: Au nanoparticles target cancer, *Nano Today* **2** (1), 18-29 (2007).
26. W.-K. Fong, T. L. Hanley, B. Thierry, N. Kirby and B. J. Boyd: Plasmonic Nanorods Provide Reversible Control over Nanostructure of Self-Assembled Drug Delivery Materials, *Langmuir* **26** (9), 6136-6139 (2010).
27. S. J. Leung, X. M. Kachur, M. C. Bobnick and M. Romanowski: Wavelength-Selective Light-Induced Release from Plasmon Resonant Liposomes, *Advanced Functional Materials*, (2011).
28. J. R. Krenn: Nanoparticle waveguides: Watching energy transfer, *Nat Mater* **2** (4), 210-211 (2003).
29. H. A. Atwater: The promise of Plasmonics, *Scientific American* **296** (4), 56-63 (2007).
30. U. Kreibig and M. Vollmer, *Optical properties of metal clusters*. (Springer, Berlin, 1995).

31. R. Gupta, M. J. Dyer and W. A. Weimer: Preparation and characterization of surface plasmon resonance tunable gold and silver films, *Journal of Applied Physics* **92** (9), 5264-5271 (2002).
32. M. Lončarić, J. Sancho-Parramon, M. Pavlović, H. Zorc, P. Dubček, A. Turković, S. Bernstorff, G. Jakopic and A. Haase: Optical and structural characterization of silver islands films on glass substrates, *Vacuum* **84** (1), 188-192 (2009).
33. G. Xu, M. Tazawa, P. Jin, S. Nakao and K. Yoshimura: Wavelength tuning of surface plasmon resonance using dielectric layers on silver island films, *Appl Phys Lett* **82** (22), 3811-3813 (2003).
34. J. Toudert, D. Babonneau, L. Simonot, S. Camelio and T. Girardeau: Quantitative modelling of the surface plasmon resonances of metal nanoclusters sandwiched between dielectric layers: the influence of nanocluster size, shape and organization, *Nanotechnology* **19** (12), 125709 (2008).
35. T. Wenzel, J. Bosbach, A. Goldmann, F. Stietz and F. Träger: Shaping nanoparticles and their optical spectra with photons, *Applied Physics B: Lasers and Optics* **69** (5), 513-517 (1999).
36. A. Serrano, O. R. d. l. Fuente and M. A. Garcia: Extended and localized surface plasmons in annealed Au films on glass substrates, *Journal of Applied Physics* **108** (7), 074303 (2010).
37. K. Baba, T. Okuno and M. Miyagi: Silver-gold compound metal island films prepared by using a two-step evaporation method, *Appl Phys Lett* **62** (5), 437-439 (1993).
38. F. Hubenthal, N. Borg and F. Träger: Optical properties and ultrafast electron dynamics in gold–silver alloy and core–shell nanoparticles, *Applied Physics B: Lasers and Optics* **93** (1), 39-45 (2008).
39. J. Sancho-Parramon, V. Janicki, M. Lončarić, H. Zorc, P. Dubček and S. Bernstorff: Optical and structural properties of Au-Ag islands films for plasmonic applications, *Applied Physics A: Materials Science & Processing*, 1-4 (2011).

40. J. Sancho-Parramon, V. Janicki, H. Zorc and M. Lončarić: Modification of optical properties of metal island films by electric field-assisted dissolution of clusters, *SPIE Proceedings* **7101**, 71011X-71017 (2008).
41. A. Abdolvand, A. Podlipensky, S. Matthias, F. Syrowatka, U. Gösele, G. Seifert and H. Graener: Metallodielectric Two-Dimensional Photonic Structures Made by Electric-Field Microstructuring of Nanocomposite Glasses, *Advanced Materials* **17** (24), 2983-2987 (2005).
42. V. Janicki, J. Sancho-Parramon, F. Peiro and J. Arbiol: Three-dimensional photonic microstructures produced by electric field assisted dissolution of metal nanoclusters in multilayer stacks, *Appl Phys B-Lasers O* **98** (1), 93-98 (2010).
43. M. Losurdo, M. Bergmair, G. Bruno, D. Cattelan, C. Cobet, A. de Martino, K. Fleischer, Z. Dohcevic-Mitrovic, N. Esser, M. Galliet, R. Gajic, D. Hemzal, K. Hingerl, J. Humlicek, R. Ossikovski, Z. Popovic and O. Saxl: Spectroscopic ellipsometry and polarimetry for materials and systems analysis at the nanometer scale: state-of-the-art, potential, and perspectives, *Journal of Nanoparticle Research* **11** (7), 1521-1554 (2009).
44. H. Zorc, M. Lončarić and J. Sancho-Parramon: Use of gold island films in design of reflectors with high luminosity, *Appl Optics* **50** (9), C364-C367 (2011).
45. C. G. Granqvist and O. Hunderi: Optical properties of Ag-SiO<sub>2</sub> Cermet films: A comparison of effective-medium theories, *Phys Rev B* **18** (6), 2897 (1978).
46. W. E. Vargas, D. E. Azofeifa, N. Clark and X. Marquez: Collective response of silver islands on a dielectric substrate when normally illuminated with electromagnetic radiation, *Journal of Physics D: Applied Physics* **41** (2), 025309 (2008).
47. R. Lazzari and I. Simonsen: Gran Film: a software for calculating thin-layer dielectric properties and Fresnel coefficients, *Thin Solid Films* **419** (1-2), 124-136 (2002).
48. J. A. Venables, G. D. T. Spiller and M. Hanbucken: Nucleation and growth of thin films, *Reports on Progress in Physics* **47** (4), 399 (1984).



49. N. Kaiser: Review of the Fundamentals of Thin-Film Growth, *Appl. Opt.* **41** (16), 3053-3060 (2002).
50. C. R. Henry: Surface studies of supported model catalysts, *Surface Science Reports* **31** (7-8), 231-325 (1998).
51. M. Bäumer and H.-J. Freund: Metal deposits on well-ordered oxide films, *Progress in Surface Science* **61** (7-8), 127-198 (1999).
52. C. T. Campbell: Ultrathin metal films and particles on oxide surfaces: structural, electronic and chemisorptive properties, *Surface Science Reports* **27** (1-3), 1-111 (1997).
53. C. Kittel, *Introduction to Solid State Physics, 8th Edition*. (John Wiley & Sons, Inc., 2005).
54. L. Cauchy: Sur la refraction et la reflexion de la lumiere, *Bull. Des. Sc. Math.* **14**, 6-10 (1830).
55. W. Sellmeier: Zur Erklärung der abnormen Farbenfolge im Spectrum einiger Substanzen, *Annalen der Physik und Chemie* **143** (272-282), (1871).
56. F. Urbach: The Long-Wavelength Edge of Photographic Sensitivity and of the Electronic Absorption of Solids, *Physical Review* **92** (5), 1324 (1953).
57. S. Kasap and P. Capper, (Springer, New York, 2007).
58. P. Drude: Zur Elektronentheorie der Metalle, *Annalen der Physik* **306** (3), 566-613 (1900).
59. A. Sommerfeld: Zur Elektronentheorie der Metalle, *Naturwissenschaften* **15** (41), 825-832 (1927).
60. J. M. Ziman, *Principles of the Theory of Solids*. (Cambridge University Press, 1979).

61. N. Ashcroft and D. Mermin, *Solid State Physics*. (Brooks Cole, 1976).
62. *SOPRA n&k Optical Database*.
63. S. A. Maier, P. G. Kik, H. A. Atwater, S. Meltzer, E. Harel, B. E. Koel and A. A. G. Requicha: Local detection of electromagnetic energy transport below the diffraction limit in metal nanoparticle plasmon waveguides, *Nat Mater* **2** (4), 229-232 (2003).
64. C. Bohren and D. Huffman, *Absorption and Scattering of Light by Small Particles*. (Wiley, New York, 1998).
65. M. Šunjić, in *Dynamics of Gas-Surface Interaction*, edited by G. Benedek and U. Valbusa (Springer-Verlag, Berlin, 1982).
66. R. Brako, J. Hrnčević and M. Šunjić: Curvature dependence of surface phonon and plasmon frequencies, *Zeitschrift für Physik B Condensed Matter* **21** (2), 193-201 (1975).
67. D. E. Aspnes: Optical properties of thin films, *Thin Solid Films* **89** (3), 249-262 (1982).
68. H. A. Lorentz: Über die Beziehung zwischen der Fortpflanzungsgeschwindigkeit des Lichtes und der Körperdichte [On the relation between the propagation speed of light and density of a body], *Ann. Phys.* **9**, 641-665 (1880).
69. L. Lorenz: Über die Refraktionsconstante [About the constant of refraction], *Ann. Phys.* **11**, 70-103 (1880).
70. J. C. M. Garnett: Colours in metal glasses and in metallic films, *Philos. Trans. R. Soc. Lond. A* **203**, 385–420 (1904).
71. D. A. G. Bruggeman: Berechnung Verschiedener Physikalischer Konstanten von Heterogenen Substanzen, *Ann. Phys. (Leipzig)* **24**, 636-679 (1935).
72. T. C. Choy, *Effective Medium Theory, Principles and Applications*. (Oxford University Press, 1999).

73. J. Sancho-Parramon: Surface plasmon resonance broadening of metallic particles in the quasi-static approximation: a numerical study of size confinement and interparticle interaction effects, *Nanotechnology* **20** (23), - (2009).
74. M. Hövel, B. Gompf and M. Dressel: Dielectric properties of ultrathin metal films around the percolation threshold, *Phys Rev B* **81** (3), 035402 (2010).
75. P. B. Johnson and R. W. Christy: Optical Constants of the Noble Metals, *Phys Rev B* **6** (12), 4370 (1972).
76. T. W. H. Oates and A. Mücklich: Evolution of plasmon resonances during plasma deposition of silver nanoparticles, *Nanotechnology* **16** (11), 2606 (2005).
77. A. Franke and et al.: Gaussian quadrature approach to the calculation of the optical constants in the vicinity of inhomogeneously broadened absorption lines, *Pure and Applied Optics: Journal of the European Optical Society Part A* **5** (6), 845 (1996).
78. R. M. A. Azzam and N. M. Bashara, *Ellipsometry and Polarized Light*. (North-Holland, Amsterdam, 1977).
79. H. G. Tompkins and W. A. McGahan, *Spectroscopic Ellipsometry and Reflectometry: A User's Guide*. (John Wiley & Sons, Inc., New York, 1999).
80. M. Schubert, *Infrared Ellipsometry on Semiconductor Layer Structures: Phonons, Plasmons, and Polaritons*. (Springer, Heidelberg, 2004).
81. H. G. Tompkins and E. A. Irene, (William Andrew, New York 2005).
82. H. Fujiwara, *Spectroscopic ellipsometry: principles and applications*. (John Wiley & Sons Ltd, Chichester, 2007).
83. *WVASE manual "Guide to Using WVASE32"*, J. A. Woollam Co., Inc.
84. A. Guinier: Le diffraction de rayons X aux tres petits angles., *Ann. Phys. (Paris)* **12**, 161-236 (1939).

85. A. Guinier, G. Fournet, C. B. Walker and K. L. Yudowitch, *Small Angle Scattering of X-Rays*. (Wiley, New York, 1955).
86. G. Renaud, R. Lazzari and F. Leroy: Probing surface and interface morphology with Grazing Incidence Small Angle X-Ray Scattering, *Surface Science Reports* **64** (8), 255-380 (2009).
87. A. Macleod, *Optical coatings from design through manufacture*. (Thin Film Center Inc., Tucson, 2004).
88. O. Stenzel, *The Physics of Thin Film Optical Spectra*. (Springer, Berlin, 2005).
89. H. Amenitsch, S. Bernstorff and P. Laggner: High-flux beamline for small-angle X-ray scattering at ELETTRA, *Rev Sci Instrum* **66** (2), 1624-1626 (1995).
90. H. Amenitsch, M. Rappolt, M. Kriechbaum, H. Mio, P. Laggner and S. Bernstorff: First performance assessment of the small-angle X-ray scattering beamline at ELETTRA, *Journal of Synchrotron Radiation* **5** (3), 506-508 (1998).
91. R. Lazzari: IsGISAXS: a program for grazing-incidence small-angle X-ray scattering analysis of supported islands, *Journal of Applied Crystallography* **35** (4), 406-421 (2002).
92. P. Heger, O. Stenzel and N. Kaiser: Metal island films for optics, *SPIE Proceedings* **5250**, 21-28 (2004).
93. C. Revenant, G. Renaud, R. Lazzari and J. Jupille: Growth of Ag on MgO(0 0 1) studied in situ by grazing incidence small angle X-ray scattering, *Nuclear Instruments and Methods in Physics Research Section B: Beam Interactions with Materials and Atoms* **246** (1), 112-117 (2006).
94. A. Turkovic, M. Pavlovic, M. Ivanda, M. Gaberscek and Z. C. Orel: Influence of intercalated lithium on structural and electrical properties of V<sub>2</sub>O<sub>5</sub>, mixed V/Ce oxide, and Fe<sub>2</sub>O<sub>3</sub>, *J Electrochem Soc* **153** (1), A122-A126 (2006).

95. R. Lazzari, <http://www.insp.jussieu.fr>.
96. R. R. Singer, A. Leitner and F. R. Aussenegg: Structure analysis and models for optical constants of discontinuous metallic silver films, *J Opt Soc Am B* **12** (2), 220-228 (1995).
97. J. Sancho-Parramon, A. Abdolvand, A. Podlipensky, G. Seifert, H. Graener and F. Syrowatka: Modeling of optical properties of silver-doped nanocomposite glasses modified by electric-field-assisted dissolution of nanoparticles, *Appl Optics* **45** (35), 8874-8881 (2006).
98. A. Podlipensky, A. Abdolvand, G. Seifert and H. Graener: Femtosecond laser assisted production of dichroitic 3D structures in composite glass containing Ag nanoparticles, *Applied Physics A: Materials Science & Processing* **80** (8), 1647-1652 (2005).
99. C. Noguez: Optical properties of isolated and supported metal nanoparticles, *Optical Materials* **27** (7), 1204-1211 (2005).
100. E. D. Palik, *Handbook of Optical Constants of Solids I, II, III*. (Academic Press, San Diego, 1998).
101. H. Wormeester, E. S. Kooij and B. Poelsema: Effective dielectric response of nanostructured layers, *Physica Status Solidi (a)* **205** (4), 756-763 (2008).
102. G. Xu, M. Tazawa, P. Jin and S. Nakao: Surface plasmon resonance of sputtered Ag films: substrate and mass thickness dependence, *Applied Physics A: Materials Science & Processing* **80** (7), 1535-1540 (2005).
103. A. J. de Vries, E. S. Kooij, H. Wormeester, A. A. Mewe and B. Poelsema: Ellipsometric study of percolation in electroless deposited silver films, *Journal of Applied Physics* **101** (5), 053703 (2007).
104. M. Lončarić, J. Sancho-Parramon and H. Zorc: Optical properties of gold island films-a spectroscopic ellipsometry study, *Thin Solid Films* **519** (9), 2946-2950 (2011).

105. J. N. Hilfiker, N. Singh, T. Tiwald, D. Convey, S. M. Smith, J. H. Baker and H. G. Tompkins: Survey of methods to characterize thin absorbing films with Spectroscopic Ellipsometry, *Thin Solid Films* **516** (22), 7979-7989 (2008).
106. P. Heger, O. Stenzel and N. Kaiser, presented at the Proc. of SPIE 5250, 2004 (unpublished).
107. *Spectra, Inc. TFCalc*, <http://www.sspectra.com/>.
108. A. V. Tikhonravov: Some theoretical aspects of thin-film optics and their applications, *Appl. Opt.* **32** (28), 5417-5426 (1993).
109. A. V. Tikhonravov, M. K. Trubetskov and G. W. DeBell: Application of the needle optimization technique to the design of optical coatings, *Appl. Opt.* **35** (28), 5493-5508 (1996).
110. A. V. Tikhonravov, M. K. Trubetskov and G. W. DeBell: Optical coating design approaches based on the needle optimization technique, *Appl. Opt.* **46** (5), 704-710 (2007).

## List of symbols and abbreviations

$c$	velocity of light in vacuum
$d$	particle diameter
$d_{eff}$	effective layer thickness
$D$	interparticle distance
$E$	energy
$E_{adh}$	adhesion energy
$E$	electric field
$f$	filling factor
$f_p$	flattening parameter
$h$	particle height
$\hbar$	reduced Planck's constant
$I$	light intensity
$k$	extinction coefficient (imaginary part of complex refractive index)
$\mathbf{k}$	wave vector
$K$	absolute value of wave vector
$m_e$	electron mass
$m^*$	electron effective mass
$N$	number of particles per unit volume
$\tilde{n}$	complex refractive index
$n$	real part of the refractive index
$p$	dipole moment
$R$	reflectance
$R$	sphere radius
$R_g$	Guinier radius or gyroradius – RMS value from centre of scattering density
$R_{rms}$	film surface roughness

$t$	time
$T$	temperature
$V$	volume
$\alpha$	polarizability
$\alpha_{ext}$	absorption coefficient
$\beta$	absorption index
$\delta$	refractive index decrement
$\gamma$	damping constant; electron relaxation rate
$\gamma_{met}$	surface free energy of a metal
$\Gamma$	line-width of the plasmon resonance
$\varepsilon$	dielectric function
$\varepsilon_0$	dielectric permittivity of vacuum
$\varepsilon_1$	real part of the dielectric function
$\varepsilon_2$	imaginary part of the dielectric function
$\varepsilon_h$	dielectric function of host material
$\varepsilon_m$	dielectric function of metal inclusions
$\theta$	angle of incidence
$\lambda$	wavelength
$C_{abs}$	absorption cross section
$C_{ext}$	extinction cross section
$C_{sca}$	scattering cross section
$\sigma_{R(H)(D)}$	size distribution dispersions
$\tau$	electron relaxation time
$\omega_0$	resonance frequency
$\omega_p$	plasma frequency



AFM	atomic force microscopy
EMT	effective medium theory
FTIR	Fourier Transform Infrared Spectroscopy
FWHM	full-width-at-half-maximum
GISAXS	grazing-incidence small-angle X-ray scattering
LSP	localized surface plasmon
LSPR	localized surface plasmon resonance
MSE	mean squared error
NIR	near infrared
SERS	surface-enhanced Raman scattering
TEM	transmission electron microscopy
UHV	ultra-high vacuum
UV	ultra-violet light
VASE	variable angle spectroscopic ellipsometry
VIS	visible light
XRD	X-ray Diffraction
a.u.	arbitrary unit
e.g.	for example (exempli gratia)
et al.	and others (et alia)
i.e.	that is (id est)

## Curriculum vitae

### Martin Lončarić

#### Education

*Postgraduate:* Since 2002. Faculty of Science, University of Zagreb,  
Physics Department – doctoral study

*Undergraduate:* 1993 – 2001 University of Zagreb, Faculty of Science,  
Physics Department

Diploma thesis (2001):

Transportna svojstva vala gustoće na niskim temperaturama  
("Transport properties of density wave at low temperatures")

*Secondary school:* 1989 – 1993 in Zagreb, MIOC "Vladimir Popović"  
received International Baccalaureate Diploma in 1993

*Primary school:* 1981 – 1989 in Varaždin

**Languages:** Croatian (native), English (fluent)

#### Subjects of research:

2008 – Optical and structural properties of metal nanoparticles

2002 – 2008 Photodynamic diagnosis and therapy

2000 – 2001 Electrical transport properties of low-dimensional organic materials

#### Work experience:

Since May 2002 Research assistant at "Ruđer Bošković" Institute,  
Division of Laser and Atomic Research and Development,  
Laboratory of Optics and Thin Films

## List of publications in Current Contents journals

1. Pinterić, Marko; Vuletić, Tomislav; Lončarić, Martin; Tomić, Silvia; von Schütz, Ulrich Jost. *Low frequency dielectric spectroscopy of the Peierls-Mott insulating state in the deuterated copper-DCNQI systems*. European Physical Journal B, 16 (2000); 487-493
2. Vuletić, Tomislav; Pinterić, Marko; Lončarić, Martin; Tomić, Silvia; von Schütz, Ulrich Jost. *Non-ohmic electrical transport in the Peierls-Mott state of deuterated copper-DCNQI systems*. Synthetic Metals, 120 (2001); 1001-1002
3. Pinterić, Marko; Vuletić, Tomislav; Lončarić, Martin; Petukhov, Kostja; Gorshunov, Boris; von Schütz, Ulrich Jost; Tomić, Silvia; Dressel, Martin. *Mott-Peierls phase in deuterated copper-DCNQI systems: a comprehensive study of longitudinal and transverse conductivity and aging effects*. Journal of Physics: Condensed Matter, 15 (2003); 7351-64
4. Kopriva, Ivica; Peršin, Antun; Zorc, Hrvoje; Pašić, Aida; Lipozenčić, Jasna; Kostović, Krešimir; Lončarić, Martin. *Visualisation of basal cell carcinoma by fluorescence diagnosis and independent component analysis*. Photodiagnosis and Photodynamic Therapy, 4 (2007), 3; 190-196
5. Lončarić, Martin; Sancho-Paramon, Jordi; Pavlović, Mladen; Zorc, Hrvoje; Dubček, Pavo; Turković, Aleksandra; Bernstorff, Sigrid; Jakopic, Georg; Haase, Anja. *Optical and structural characterization of silver islands films on glass substrates*. Vacuum, 84 (2009), 1; 188-192
6. Lončarić, Martin; Sancho-Paramon, Jordi; Zorc, Hrvoje. *Optical properties of gold island films – a spectroscopic ellipsometry study*. Thin Solid Films, 519 (2011), 9; 2946-2950
7. Sancho-Paramon, Jordi; Janicki, Vesna; Lončarić, Martin; Zorc, Hrvoje; Dubček, Pavo; Bernstorff, Sigrid. *Optical and structural properties of Au-Ag islands films for plasmonic applications*. Applied Physics A: Materials Science & Processing, 103 (2011), 3; 745-748
8. Zorc, Hrvoje; Lončarić, Martin; Sancho-Paramon, Jordi. *Use of gold island films in design of reflectors with high luminosity*. Applied Optics, 50 (2011), 9; C364-C367

## Accepted for publication

1. Turković, Aleksandra; Dubček, Pavo; Rakić, Mario; Lončarić, Martin; Etlinger, Božidar; Bernstorff, Sigrid. *SAXS/DSC/WAXD study of TiO<sub>2</sub> nanoparticles and the effect of gamma-radiation on nano-polymer electrolyte*. Vacuum, (2011).

## Other contributions:

1. Kopriva, Ivica; Zorc, Hrvoje; Peršin Antun; Lipozenčić, Jasna; Pašić, Aida; Kostović, Krešimir, Lončarić, Martin. *Comparative study of PDD fluorescent excitation and image processing methods*, 6th International Symposium on Photodynamic Diagnosis and Therapy in Clinical Practice  
H. Kostron, G. Jori (ed.). Bressanone, 2006.
2. Advances in Optical Thin Films III. Glasgow, (UK). 2-3 September 2008 J. Sancho-Parramon, V. Janicki, H. Zorc, M. Lončarić, *Modification of optical properties of metal island films by electric field assisted dissolution of clusters*, Published in SPIE proceedings. Vol Proc. SPIE 7101, 71011X (2008)

## Conference contributions

1. 5<sup>th</sup> International Symposium on Photodynamic Diagnosis and Therapy in Clinical Practice. Bressanone (Italy), 2003. I. Radman, A. Peršin, H. Zorc, K. Tisaj, V. Stanišić, M. Lončarić, D. Soldo Roudnicky, A. Radman, *First results of the use of new LED-based light sources on PDD and PDT of Mycosis Fungoides*, B. Kramer, H. Kostron, G. Jori (ur.).
2. 15<sup>th</sup> Međunarodni sastanak "Vakuumska znanost i tehnika". Varaždin (Croatia). 4 June 2008. M. Lončarić, J. Sancho-Parramon, M. Pavlović, H. Zorc, A. Haase, G. Jakopic "Optical spectroscopy and atomic force microscopy study of silver island films" Poster
3. 15<sup>th</sup> Međunarodni sastanak "Vakuumska znanost i tehnika". Varaždin (Croatia). 4 June 2008. M. Pavlović, M. Lončarić, J. Sancho-Parramon, H. Zorc, A. Turković, P. Dubček, and S. Bernstorff, *GISAXS study of silver islands deposited on glass substrate*" Poster
4. 12<sup>th</sup> Joint Vacuum Conference, 10<sup>th</sup> European Vacuum Conference 7<sup>th</sup> Annual Meeting of the German Vacuum Society, 22–26 September, 2008, Balatonalmadi, Lake Balaton, Hungary. M. Lončarić, J. Sancho-Paramon, M. Pavlović, H. Zorc, P. Dubček, A. Turković, S. Bernstorff, G. Jakopic, A. Haase, *Optical and Structural Characterization of Silver Island Films on Glass Substrates*, Poster
5. 16<sup>th</sup> International Scientific Meeting on Vacuum Science and Technique, Bohinj (Slovenia), 4-5 June 2009. J. Sancho-Parramon, V. Janicki, H. Zorc, M. Lončarić, *Modification of optical properties of metal island films by electric field assisted dissolution of clusters*, Oral (invited)

6. 6. znanstveni sastanak Hrvatskog fizikalnog društva, Primošten (Croatia), 8-11 October 2009. Hrvoje Zorc, Martin Lončarić, Jordi Sancho-Parramon, Vesna Janicki, *Optička svojstva plazmoničkih nanomaterijala u tankom sloju*, Poster
7. 2<sup>nd</sup> International Conference on Metamaterials, Photonic crystals and Plasmonics META10, Cairo (Egypt) J. Sancho-Parramon<sup>1</sup>, V. Janicki, M. Lončarić, H. Zorc, P. Dubček, S. Bernstorff, *Optical and structural properties of silver-gold islands films for plasmonic applications*, 22 February 2010, Poster
8. 17. Međunarodni sastanak “Vakuumska znanost i tehnika”. Tuhelj (Croatia). 1 June 2010. M. Lončarić, H. Zorc, J. Sancho-Parramon, S. Šegota, *Spektroskopska elipsometrija zlatnih nanočestica u tankom sloju*, Poster

## Patents

1. Peršin, Antun; Tisaj, Krešimir; Zorc, Hrvoje; Stanišić, Vitomir; Soldo-Roudnicky, Dunja; Agatić, Nenad; Lončarić, Martin; Radman, Anton. *Mobile Device for Photodynamic Diagnostics and Therapy and Methods*. PCT WO2005035058 2005-04-21
2. Peršin, Antun; Tisaj, Krešimir; Zorc, Hrvoje; Stanišić, Vitomir; Soldo Roudnicky, Dunja; Agatić, Nenad; Lončarić, Martin; Radman, Anton. *Portable Illuminator for Photodynamic Diagnostics*. PCT WO2005035059 2005-04-21
3. Peršin, Antun; Tisaj, Krešimir; Zorc, Hrvoje; Stanišić, Vitomir; Soldo Roudnicky, Dunja; Agatić, Nenad; Lončarić, Martin; Radman, Anton. *Portable Illuminator for Photodynamic Therapy*. PCT WO2005035060 2005-04-21
4. Peršin, Antun; Tisaj, Krešimir; Zorc, Hrvoje; Stanišić, Vitomir; Soldo-Roudnicky, Dunja; Agatić, Nenad; Lončarić, Martin; Radman, Anton. *Pametni prijenosni kontaktni iluminator za fotodinamičku terapiju površinskih tumora*. HR 4294967295

## In preparation

1. Lončarić, Martin; Sancho-Paramon, Jordi; Zorc, Hrvoje; Šegota, Suzana; Dubček, Pavo; Bernstorff, Sigrid. *Optical and structural characterization of gold island films on glass substrates*